ABSTRACT

Title of thesis: UNDERSTANDING BROWNOUT USING DUAL-PHASE PARTICLE IMAGE VELOCIMETRY MEASUREMENTS

Anish Joshua Sydney, Master of Science, 2011

Thesis directed by: Professor J. Gordon Leishman
Department of Aerospace Engineering

To better understand the development of brownout dust clouds generated by rotorcraft, the dual-phase flow environment produced by one- and two-bladed laboratory-scale rotors operating over a mobile sediment bed were studied. Three size ranges of characterized glass microspheres were used to represent the sediment particles. Time-resolved flow visualization, particle image velocimetry, and particle tracking velocimetry were used to make the flow measurements. The high imaging rate of these systems allowed the time-history of the rotor wake interactions with the sediment bed to be documented, providing a better understanding of the transient processes and mechanisms that lead to the uplift of sediment and the formation of dust clouds near a rotor in ground effect operation. In particular, the fluid dynamics of the blade tip vortices near the bed were examined in detail, which were shown to have a primary influence on the mobilization of sediment. In general, the near-wall measurements documented at least five fundamental uplift and sediment transport mechanisms below the rotor: 1. Creep, 2. Modified saltation and saltation bombardment, 3. Vortex induced trapping, 4. Reingestion bombardment (local and global), and 5. Secondary suspension. In addition, a further mechanism related to the

local unsteady pressure field induced by the convecting wake vortices was hypothesized to contribute to the uplift of sediment. The highest sediment entrainment levels occurred within the wake impingement zone, mainly from the erosion aspects of the tip vortices on the bed. Once entrained, significant quantities of sediment were intermittently trapped in the vortex-induced upwash field. Secondary sediment suspension was found to be more prevalent with the two-bladed rotor because of the propensity for merging of adjacent blade tip vortices and the resulting higher upwash velocities. The trapping of suspended sediment particles into the vortex flow was shown to cause recirculation of the particles back onto the sediment bed, thereby ejecting more sediment through bombardment mechanisms.

UNDERSTANDING BROWNOUT USING DUAL-PHASE PARTICLE IMAGE VELOCIMETRY MEASUREMENTS

by

Anish Joshua Sydney

Thesis submitted to the Faculty of the Graduate School of the
University of Maryland, College Park in partial fulfillment
of the requirements for the degree of
Master of Science
2011

Advisory Committee:
Professor J. Gordon Leishman, Chair/Advisor
Associate Professor James Baeder
Assistant Professor Anya Jones

Acknowledgments

First and foremost I'd like to thank my advisor and thesis committee chair, Professor J. Gordon Leishman, for giving me the opportunity to work under his tutelage on this interesting and challenging project. It has been an honor to learn from Dr. Leishman through the years as an Undergraduate and Graduate Research Assistant.

I would like to thank Associate Professor James Baeder and Assistant Professor Anya Jones for their contributions as members of my thesis committee.

A very special thanks to Ajay Baharani, who helped in gathering, processing, and analyzing all the data in this thesis. His "do-it-right-the-first-time" attitude, work ethic, and constant support are what made this work possible. I would also like to thank Bradley Johnson, who was my mentor when I was an Undergraduate Research Assistant and began teaching me the science, as well as the art, behind PIV.

I want to thank all of the guys in the lab, Joe Milluzzo, Joe Ramsey, Dave Mayo, Ben Hance, Jaime Reel, Juergen Rauleder, Bharath Govinda Rajan and Harrison Chau for all of their help and guidance. Coming in to work everyday is always exciting and fun with these guys around, I couldn't ask for a better group of people to work with.

My deepest appreciation for my family, specifically my twin brother Nitin. He has always been my strength and motivation. His unwavering support throughout undergrad and graduate school have kept me going. A warm thank you to my parents, Mukesh and Rekha. They've provided so many opportunities for me, opened so many doors, and showered me with unconditional love. Without them, I wouldn't be where I am today.

I would like to acknowledge the support of the Air Force Office of Scientific Re-

search (AFOSR) under Multidisciplinary University Research Initiative Grant No. W911NF0410176. I would like to thank contract monitor, Dr. Douglas Smith, for his support and advice during the course of this research.

Table of Contents

List of Figures

Nomenclature

A	Rotor disk area
C_T	Rotor thrust coefficient, $= T/\rho\pi\Omega^2 R^4$
C_T/σ	Blade loading coefficient
DL	Disk loading
M	Camera magnification factor
r	Radial distance
R	Radius of blade
R_c	Particle centroid
Re	Reynolds number, $= \rho V_{tip} c/\mu$
Re_ν	Vortex Reynolds number, $= \Gamma/\nu$
T	Rotor thrust
u, v	Velocities in r and z directions, respectively
v_i	Induced velocity
V_{tip}	Rotor tip speed
x, y	PIV coordinates in the horizontal and vertical directions, respectively
z	Distance of rotor above ground plane

Greek Symbols

Δt	Pulse separation time, μs
Δx, Δy	Grid spacing in the x and y directions, respectively
Φ_{fg}	Cross-correlation function
ρ	Flow density
σ	Rotor solidity
ψ	Blade azimuth angle
Ω	Rotational speed of the rotor
ζ	Wake age

Abbreviations

CFD	Computational fluid dynamics
CMOS	Complementary metal oxide semiconductor
FV	Flow visualization
PIV	Particle image velocimetry
PSD	Particle size distribution
TPP	Rotor tip path plane
TR-PIV	Time-resolved particle image velocimetry

Chapter 1

Introduction

1.1 The Problem of Brownout

"Brownout" is a phenomenon that occurs when rotorcraft operate in arid environments over ground surfaces covered with loose sediment such as dust or sand. The problem occurs when a flying rotorcraft becomes close enough to the ground such that its rotor wake (or wakes if there is more than one rotor) interacts with the loose material on the sediment bed, mobilizing the material and initiating the onset of a rapidly developing and dense dust cloud. A helicopter photographed during a landing and encountering brownout conditions is shown in Fig. 1.1, where the action of its rotor wake has produced sufficiently strong aerodynamic forces to mobilize and uplift the dust that was originally stationary on the ground. Encounters with brownout conditions are the leading cause of human factor-related mishaps during military rotorcraft operations [1], and civilian helicopters have also suffered from the problem [2].

A major practical concern with the occurrence of brownout is that the pilot loses visibility of the landing or take-off zone, which results in a loss of situational awareness. The detrimental effects of the dust cloud manifests in two main ways: loss of visual cues needed for landing and spurious sensory cues. To safely land the helicopter, the pilot needs to use certain visual cues from the ground such as the horizon, a nearby structure such a building, blades of grass, etc. and the loss of such cues poses a serious safety of

Figure 1.1: A landing helicopter experiencing brownout conditions in a desert environment (courtesy of OADS).

flight risk. The pilot may also experience spurious sensory cues from the swirling and convection of the forming dust cloud; the relative motion of the dust cloud often causes the pilot to experience vection illusions that may result in the pilot making undesirable control inputs too near the ground that can result in a crash.

Besides losses of visibility, the suspended dust particles cause rapid abrasion of the rotor blades as well as engine wear, creating serious maintenance issues and reducing the flight readiness of the aircraft. Blades have been reported to last for only tens of hours if frequent brownout conditions are encountered in operational service, causing expensive maintenance issues. In addition to maintenance, the swirling dust cloud creates a hazardous environment for ground crew personnel, thereby hampering or limiting ground operations.

There have been several attempts at mitigating the brownout problem, although none yet from a rotorcraft design perspective. Pilots have adopted operational strategies

such as flying faster near the ground to outpace the evolving dust cloud. Another possible option is to minimize the time in the flare during landing, thereby potentially stirring up less dust. Pilots have also tried increasing the rate of descent in an attempt to land before the dust cloud has had time to fully develop. Such landing strategies have served to operationally mitigate brownout, but only to a limited extent. This is because the techniques are vehicle specific, depend on the weight of the vehicle and the density altitude at which it operates, the types of dust that are encountered, etc., and they may just be unsafe maneuvers (e.g., flying fast near the ground is never safe).

Other attempts at brownout mitigation have been directed toward the development of sensors that seek to penetrate the dust cloud, which are combined with advanced display avionics to replace missing visual information for the pilot [3–5]. Such systems have been reasonably effective in improving safety of flight when they are combined with certain operational tactics and flight path management. However, the number of operational mishaps with rotorcraft remains unacceptably high, and brownout related maintenance issues continue to reduce mission readiness rates and drive up operational costs.

The foregoing issues demonstrate a need to see if there is an option of mitigating brownout at its source, i.e., recognizing brownout as a fluid mechanics problem with (potentially) a fluid mechanics solution, which is the motivation behind the present research work. Anecdotal evidence at least, suggests that the development and formation of a dust cloud is dependent on the specific vehicle and have shown that some helicopters have less severe brownout signatures, implying that there may be certain features of the vehicle design (e.g., the rotor) that could be used or changed as a viable approach to brownout mitigation. For example, Fig. 1.2 shows an image taken of a helicopter landing over a bed

Figure 1.2: A landing helicopter with the formation of a more favorable ring or toroidal shaped dust cloud away from the immediate landing zone.

of loose sediment, which generates a more preferable type of brownout cloud in the form of a toroidal dust ring. While there is still a considerable amount of sediment uplifted, in this case it is blown a significant distance away from the helicopter, allowing the pilot to better see the landing zone. Other helicopters are known to produce large dome-shaped dust clouds that may completely engulf the aircraft, which is also accompanied by significant reingestion of dust back through the rotor(s) and bombardment of the suspended dust back onto the sediment bed and ejecting more dust in the process, which can produce the most severe brownout conditions. The reason(s) for such profound differences in the dust clouds, however, are not yet understood.

Except for limited data contained in Refs. 4–6, there is still a relative dearth of useful quantitative measurements for rotorcraft encountering actual brownout conditions. In an attempt to begin to understand why some rotorcraft produce worse brownout signatures than others, work has been done by Milluzzo and Leishman [7] to characterize brownout severity for different rotorcraft based on the geometric and aerodynamic operating condi-

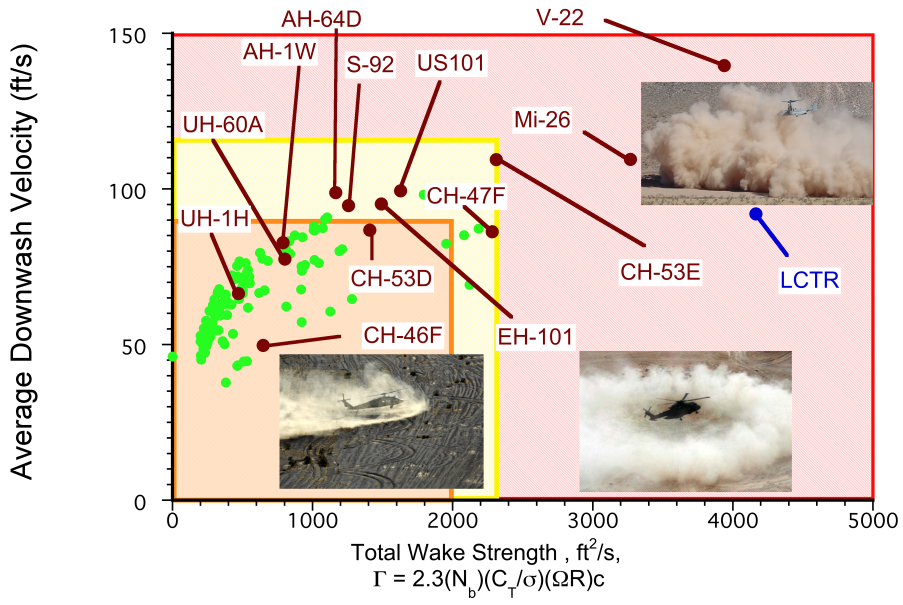

Figure 1.3: A measure of brownout severity as a function of downwash velocity and total wake strength (From Milluzzo and Leishman [7].)

tions of the main rotor(s). Figure 1.3, which relates average induced downwash from the rotor to a measure of wake strength, implies that the unique characteristics of each vehicle can significantly impact the intensity of a brownout cloud. Figure 1.3 also identifies three regions of brownout severity, although they were based on subjective assessments of photographs and videography of rotorcraft encountering actual brownout conditions. The first region is typical of a cloud that is relatively benign and does not completely attenuate the required visual cues for landing. The next two regions are progressively worse brownout signatures and create dust clouds that may become severe enough to affect safety of flight. While the total wake strength used in this particular correlation includes the number of blades, blade loading coefficient, rotational tip speed, rotor radius, and blade chord, the importance of each variable to the problem of brownout is yet to be fully determined. As

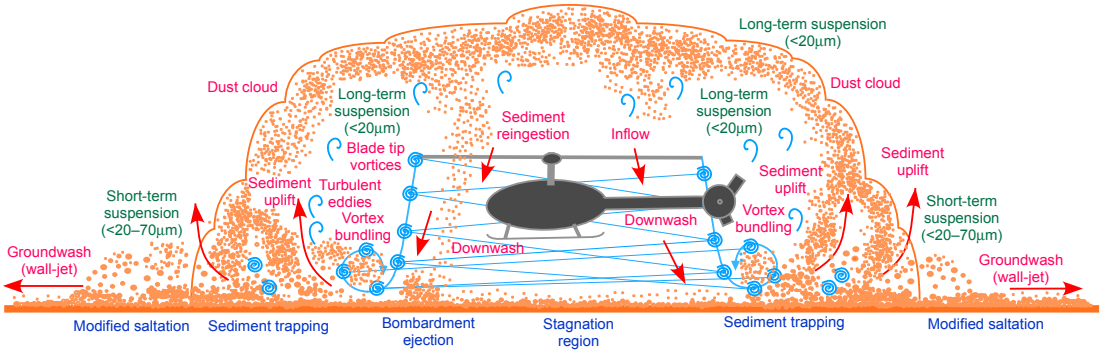

Figure 1.4: A schematic of some of the fluid dynamic mechanisms involved in the uplift and transport of sediment in the development of brownout conditions surrounding a helicopter over a mobile sediment bed.

such, the goal of the present work is to better identify the fundamental sediment mobilization and uplift mechanisms involved in the brownout problem, and how certain rotor design variables may effect these mechanisms.

1.2 Fluid Dynamics of Brownout

The problem of brownout obviously requires a fundamental understanding of the underlying fluid dynamics. A schematic of the fluid dynamics of the problem is shown in Fig. 1.4, which identifies at least some of the physical mechanisms involved. The fluid dynamics of brownout is fundamentally one with two fluid phases: 1. The carrier phase, i.e., the three dimensional, unsteady flow in the rotor wake and 2. The dispersed phase, which is the sediment particles that are mobilized by the rotor flow. The two fluid phases may interact with one another (e.g., momentum coupling, particle collisions, etc.), further increasing the complexity of the problem. The characteristics of the rotor wake flow near the ground are responsible for initiating the various fluid dynamic forces that mobi-

lize and uplift the dust particles and, therefore, play a central role in producing brownout conditions. Such forces involve (but are not limited to) shear, pressure, and turbulence. Measurements made with landing helicopters [4, 5] have shown that brownout clouds are actually composed of small dust particles ($<10\ \mu$m in diameter). Such particles are relatively more cohesive and are not as easily mobilized by the boundary layer shear stresses induced below a rotor, raising some interesting questions as to how such small particles then end up constituting most of the brownout dust cloud. Answering this question is one of the main goals of the present work. To this end, the local action of the rotor blade tip vortices and the bombardment of particles back onto the underlying bed seems to play a particularly important role in the uplift of sediment and the creation of dust clouds [8]. Compounding the brownout problem is that different levels of brownout severity can be expected based solely on the nature of the sediment bed over which a helicopter is operating; the size and mineralogy of the particles, as well as their compactness, cohesiveness, moisture content, etc., can all effect the initial uplift of sediment particles because they change the magnitude of the interparticle forces.

Recent computational work to model brownout [9–17], including attempts at formulating mitigation strategies [18, 19], has met with mixed levels of success. The difficulty in simulating brownout dust clouds is that the mathematical models must accurately resolve the detailed vortical structures and turbulent flow produced at the ground by the rotor wake, as well as modeling the uplift and subsequent convection of billions of dust particles. Fluid modeling challenges include the need to accurately represent the effects of unsteady boundary layers, wall-jets, shear layers, concentrated vorticity in the form of trailed tip vortices, and turbulence. The modeling of sediment particles and their as-

sociated dynamics also significantly increase the complexity of the simulation, overall creating a very challenging computational problem.

While such brownout simulations are becoming increasingly credible, they still require validation with experimental measurements if they are to be used confidently to make quantitative predictions. To this end, detailed laboratory measurements are required for prototypical rotor flow problems, as well as field measurements in the actual brownout environment. Therefore, the focus of this work was to use a small-scale rotor operating over a mobile sediment bed to undertake a detailed, quantitative study of the mobilization and uplift mechanisms that actually contribute to the generation of a brownout dust cloud.

1.2.1 Rotor Flow Physics in Ground Effect Operation

Complicating the problem of understanding brownout is that the flow on the ground below a rotor operating in-ground-effect (IGE) is not yet fully understood, though it has been studied to some limited extent [20, 21]. The rotor wake contains vortical flows, turbulence and other flow structures that interact not only with the ground plane, but also with each other. Clearly, an understanding the flow of the rotor near the ground in the absence of sediment is a necessary prerequisite to understanding the complex phenomenon of brownout. Most experimental data for rotors operating in-ground-effect document rotor performance [22–27], generally exploring the advantages of a rotor in ground effect in terms of reducing power requirements for a given thrust. While some studies have focused on the fluid dynamics of the problem [20, 21, 28–30], there are relatively fewer quantitative measurements available for the flow field in the near wall region on the ground below

the rotor, and even fewer such measurements over a mobile sediment bed.

Lee et al. [20] has explored the aerodynamic flow field of a small-scale rotor operating at varying heights above a ground plane, quantifying the evolution of the wake as it interacted with the ground. They also examined the blade tip vortices produced by the rotor and the effect stretching and straining had on the vortices as the rotor height was lowered. A preliminary analysis of the effect of turbulence and diffusion on the vortices was also given. The present work significantly expands on the single-phase study performed by Lee et al., giving much further insight into the flow environment produced below a hovering rotor as it interacts with a ground plane. Milluzzo et al. [21] measured the evolution of the helicoidal blade tip vortex filament in-ground-effect for different blade tip shapes in an effort to quantify the local flow near the ground as it could potentially effect the mobilization of sediment and, ultimately, the creation of brownout conditions. The core size and velocity profile of the tip vortices for each blade tip shape was measured, as well as the resultant swirl velocities in the near-wall region. They also examined the effect that each tip shape had on flow velocity profiles along the ground and how this effected the local boundary layer profile at given radial locations.

Both of these foregoing studies, however, were limited to non-contiguous instantaneous realizations of the flow field. Brownout, however, has many temporal elements and, as such, studying the transient, unsteady aspects of the flow is necessary prerequisite to better understand the problem. To this end, the present work expands on the work of both Lee et al. [20] and Milluzzo et al. [21] to a dual-phase environment, examining how the characteristics of the rotor wake relate to the fundamental sediment uplift and mobilization mechanisms.

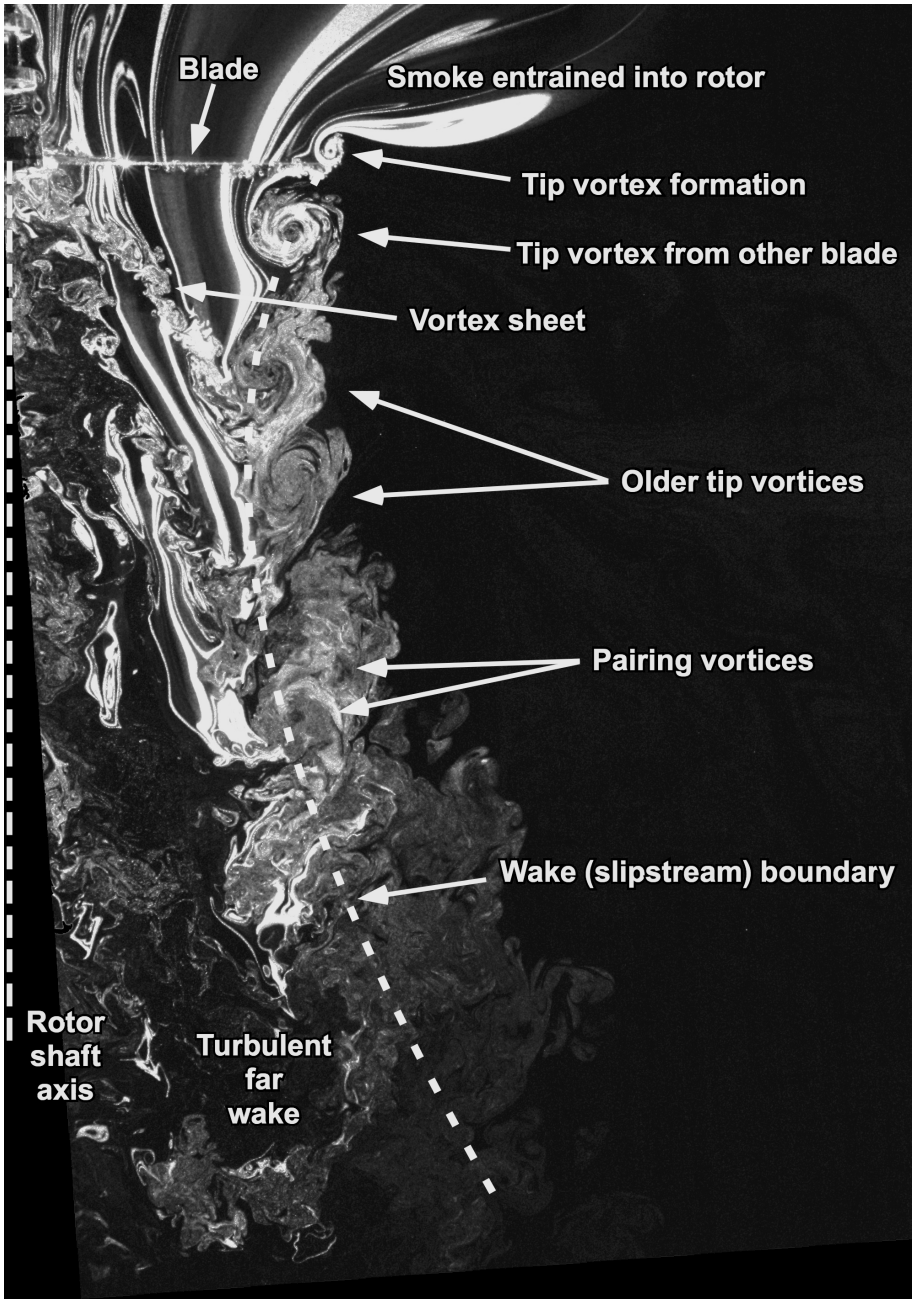

Figure 1.5: Flow visualization of a rotor OGE.

Figure 1.5 shows the flow visualization of a rotor out-ground-effect (OGE), which can be used to convey the general complexity of the wake system of a helicopter rotor. The wake is visualized using smoke, which is illuminated in a radial plane using a thin laser light sheet. The flow enters the plane of the rotor disk and immediately begins to

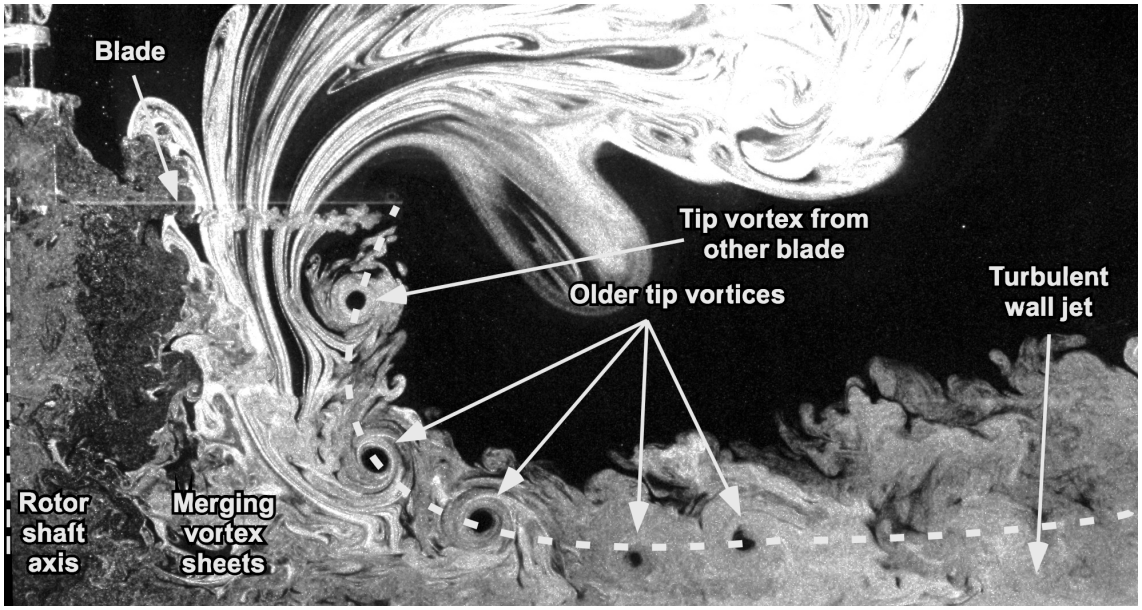

Figure 1.6: Flow visualization of a rotor IGE.

contract as it is accelerated, thereby producing thrust on the rotor system. Under the influence of diffusion and turbulence, however, the flow eventually begins to expand and slow. A dominant feature of the wake flow is the helicoidal vortex that is trailed off the tip of each blade, which convects along the slipstream boundary, occasionally merging with adjacent vortices. These vortices, also under the influence of viscosity and turbulence, normally diffuse within a few rotor revolutions (2 to 3 revolutions).

Notice from Fig. 1.6 that the flow of the rotor when it operates in-ground-effect (IGE) is very different compared to that in OGE conditions. The rotor wake in this case is forced to radially expand in a direction that is more parallel to the ground plane, a process that is discussed later in this thesis in greater detail. The radial expansion of the downwash creates a turbulent wall-jet like flow along the ground that initially thins, and eventually thickens as it develops further downstream over the wall. The tip vortices also come periodically in close proximity to the ground and interact with the developing flow there.

The rotor wake in this case is laden with concentrated vorticity that, in contrast to the OGE case, persists to much older wake ages (4 to 5 rotor revolutions), which is a result of the stretching and straining of the helicoidal tip vortex filaments. This reintensification of vorticity produces high local velocities in the near wall region, rather strongly influencing the initial mobilization and uplift of sediment [8], and is a process that is also examined in detail in the present work.

1.2.2 Sediment Transport

Understanding the formation of a brownout dust clouds necessitates the basic understanding of the detailed particle physics that are involved in the processes of their mobilization and uplift. This goal requires detailed experiments, which was the primary objective of the present work. When on the ground, a sediment particle is influenced by the characteristics of the boundary layer that develops along the sediment bed, and also by the tip vortices that were generated by the rotor as they subsequently convect over the bed, the vortices being a key contributor to the initial uplift and, ultimately, the suspension of these sediment particles [8].Once the forces and moments induced by the flow on the sediment particle exceed those caused by gravity and the interparticle cohesive forces, the particle will become mobilized. If the particle is then subsequently uplifted into the flow, the particle experiences additional aerodynamic and inertial forces. The particles also extract energy from the surrounding flow and their subsequent motion is primarily effected by the lift, drag, and weight of each particle; see Fig. 1.7.

Previous work in the field of aeolian sciences to study sediment transport are also

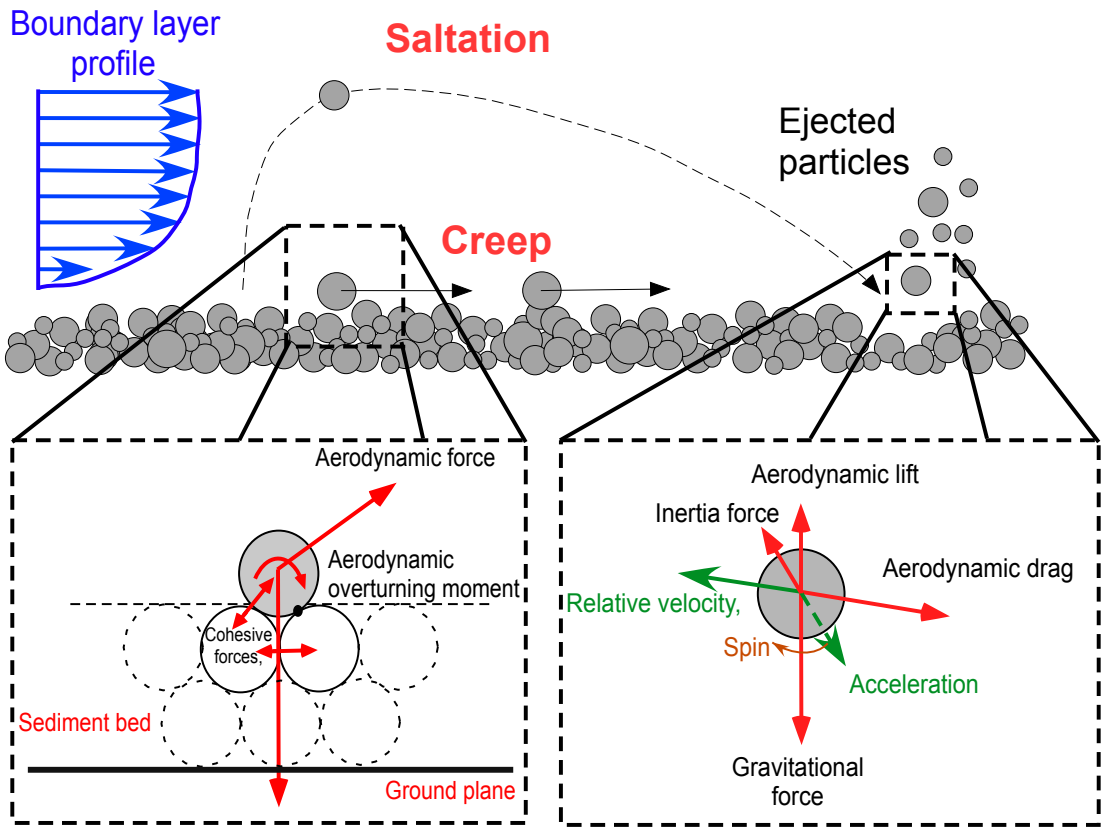

Figure 1.7: A schematic of the classic aeolian creep and saltation sediment transport mechanisms and the particle forces involved in mobilization and suspension.

useful, but are somewhat limited for improving the understanding the brownout problem. Such studies have dealt with wind-blown sands, riverine sediment flows, and simple jet-type flows [31–33]. These conditions are not entirely representative of the flow conditions found below rotors, which, as previously described, are generally dominated by discrete vorticity (i.e., vortices and larger turbulent eddies). Specific measurements are also critically required for the extraction of the parameters needed in the development of semi-empirical models derived from these studies to better describe the onset of sediment mobility.

For riverine and channel flows, the classic forms of sediment transport are creep and saltation [31, 32]. The process of creep is one in which sediment particles initially meet a threshold velocity criterion, i.e., the shear stress induced on the particles by the fluid is high enough to cause the particles to be mobilized. The sediment then rolls and translates across the surface, dislodging other sediment particles. Saltation occurs when these creeping particles encounter a local upwash in the flow, such as a local turbulent fluctuation, and are uplifted. These particles follow ballistic like trajectories in the flow, and can extract enough momentum from the surrounding fluid to eject more particles when they impact the sediment bed. The processes of creep and saltation create a layer of shifting sediment near the ground called a saltation layer [31,32], a schematic of both mechanisms and the associated forces on the sediment particles being shown in Fig. 1.7. These mechanisms, however, have yet to be studied in detail under a rotor in ground effect operation and it cannot be assumed that they occur in the same manner as observed in classical aeolian sciences. The presence of the rotor wake and its embedded tip vortices near the ground can obviously be expected to significantly effect the fluid mechanisms near the sediment bed, and so the resulting particle field can also be expected to be significantly different. To this end, the present work examines how these classic sediment transport mechanisms are modified by a rotor flow, and if any new mechanisms are introduced into the problem.

There have been few experiments that have examined details of the combined dual-phase flow environment below a rotor. This type of research requires unique experimental facilities, advanced types of instrumentation, and sophisticated analysis capabilities that can properly discriminate between the two fluid phases. Nathan and Green [34] performed

a qualitative study of the dual-phase flow environment of a rotor in-ground-effect, studying the general motion of the sediment to begin scoping out the problem of the effects of the rotor wake. This work examined a small-scale rotor in hover as well as in low-speed forward flight, shedding light onto the movement of dust in both operating conditions. In an attempt to begin quantifying the dual-phase environment in more detail, Johnson et al. [8] performed dual-phase particle image velocimetry on a lab scale rotor over a sediment bed, which has provided a foundation for the work presented in this thesis. This work studied the interaction between a rotor wake and sediment bed, and qualitatively observed a number of different sediment transport mechanisms; they concluded that there were significant differences from classical aeolian sediment transport. While this study had enormous value in scoping out the fundamental sediment transport mechanisms, it was only a preliminary investigation into the problem, with the present work expanding significantly on their initial findings.

Haehnel and Dade [35–37] have studied aspects of the brownout problem, but more so from a classical sedimentology perspective. Their studies used high-speed videography to observe the detailed sediment dynamics occurring in the near wall region under the action of a propeller wake. Measurements of the sediment bed profile were made to quantify the erosion properties and bed morphology in this non-uniform flow. Different densities of sediment particles were examined in both air and water giving insight into the aerodynamic scaling of the problem. A preliminary investigation of the flow field was also performed using hot wire anemometry, this investigation yielding values of flow velocity and estimates of wall shear stress. Unlike the measurements taken in the present work, they did not measure concurrent time histories of the flow field and the sediment

dynamics, and so the interactions between the two phases could only be inferred. Helicopter brownout is fundamentally a phenomenon in which two phases interact with one another, so the concurrent time histories of both phases is needed to fully understand the problem.

In other related work, Mulinti and Kiger [38] have used a coaxial jet system to produce an impinging jet, vortex ring, or combination of both, over a mobile sediment bed. These studies used particle image velocimetry and high-speed videography to characterize each flow, detailing the interaction between the carrier flow and the sediment bed. Geiser and Kiger [39, 40] catalogued the evolution of a vortex ring and a jet as it approached and interacted with a ground plane. This study found that there were strong secondary vortical flows produced upon the interaction of the ring with the ground. The unique property of these studies was the ability to decompose the rotor flow into its constituent parts, i.e., a vortical flow superimposed upon a axial jet-like flow. They, however were unable to fully quantify the sediment dynamics in these simplified flows or to temporally correlate their measurements, which was one of the objectives of the present work.

1.3 Objectives of the Present Work

The fluid dynamic complexity of brownout is such that experimental measurements under carefully controlled conditions are needed to properly understand the mechanisms of sediment uplift and entrainment under the action of the rotor wake in ground-effect operation. Very few experiments have been conducted on the single-phase flow environment below a rotor operating near a ground plane let alone the combined dual-phase problem.

As previously described, recent measurements have begun to expose the details of the various fluid dynamic mechanisms at work, and new computational work is also providing additional insight. However, further experimental measurements of these mechanisms, and of the complex particle-particle interactions near the ground, is needed for the validation of modeling approaches, which is a prerequisite for the accurate prediction (and the eventual mitigation) of brownout.

To this end, the main objectives of the present work were to better understand the details of the dual-phase fluid dynamics involved in the development of the dual-phase environment generated by a rotor. One of the specific goals of the present work was the quantitative measurement of vortical flows in the rotor wake and how they change when they encounter the ground. A detailed study of the flow interactions in the near-wall region has been undertaken to further gain a fundamental understanding of the fluid dynamic mechanisms. In particular, the role of concentrated vorticity was investigated as to how it influenced the mobilization and transport of the sediment particles, the various types of fluid-fluid and particle-particle interactions, and the overall properties of the developing two-phase flow field. The overall focus of the various experiments was to expose the fundamental sediment mobilization and uplift mechanisms present on the ground under an impinging rotor wake using detailed flow visualization and time-resolved particle image velocimetry.

1.4 Organization of Thesis

A discussion of the problem of rotorcraft brownout, including a summary of prior work conducted into its better understanding, has been presented in the current chapter. Next, Chapter 2 explains the experimental set up and techniques used to acquire the present measurements. Chapter 2 also gives a detailed explanation of particle image velocimetry (PIV) and particle tracking velocimetry (PTV), which were techniques used in the present work to analyze the flow measurements. Furthermore, this chapter explains the technical challenges that arose in data acquisition and how these challenges were addressed. Chapter 3 is comprised of two main parts: the single-phase flow results and the dual-phase flow results. Each section first focuses on the flow visualization used to scope out the problem, followed by the PIV and PTV results. Finally, Chapter 5 documents the conclusions drawn from the present research and suggests avenues for future research.

Chapter 2

Description of the Experiments and Instrumentation

2.1 General Description of the Experiments

The experiments were conducted in the controlled environment of a dust chamber using a prototypical flow generated by a small rotor that was hovering over a ground plane covered with sediment. The purpose of the experiments was to capture the essential features of the rotorcraft brownout problem, recognizing that the proper scaling of the problem (geometric, aerodynamic, and aeolian) would require further studies beyond those conducted here. The focus of the research was to better identify and quantify the various sediment mobility and uplift mechanisms, and to examine how these mechanisms were affected by the operating state of the rotor and its height above the ground. To this end, a range of rotor operating conditions were used to expose the details of the wake interactions with the ground, and to isolate the different sediment mobility and uplift mechanisms that may ultimately affect the formation of a brownout dust cloud.

Most of the experiments performed involved the use of a mobile sediment bed below the rotor and a sediment laden environment, so to protect the equipment all of the measurements were obtained in a specially designed dust chamber. A photograph of this test facility is shown in Fig. 2.1. This chamber provided a controlled environment for both the single- and dual-phase flow experiments. The walls of the chamber were sealed such that no dust could escape from the confines of the test area. The chamber was 2 x

Figure 2.1: The specially built dust chamber in which both the single-phase and dual-phase flow experiments with the rotor were performed.

2 x 2 meters in dimension, and the 8 m^3 volume was large enough volume to limit flow recirculation from the small rotor over the time-scales of the experiments. Additionally, flow diverters were placed at the periphery of the ground plane to direct the flow down and away from the rotor; see Fig. 2.2.

The structural frame of the dust chamber was constructed using slotted aluminum beams. The walls were made using Plexiglas sheets seated in the aluminum slots, ensuring sealed retaining walls for the dust chamber. The optically clear Plexiglas allowed for

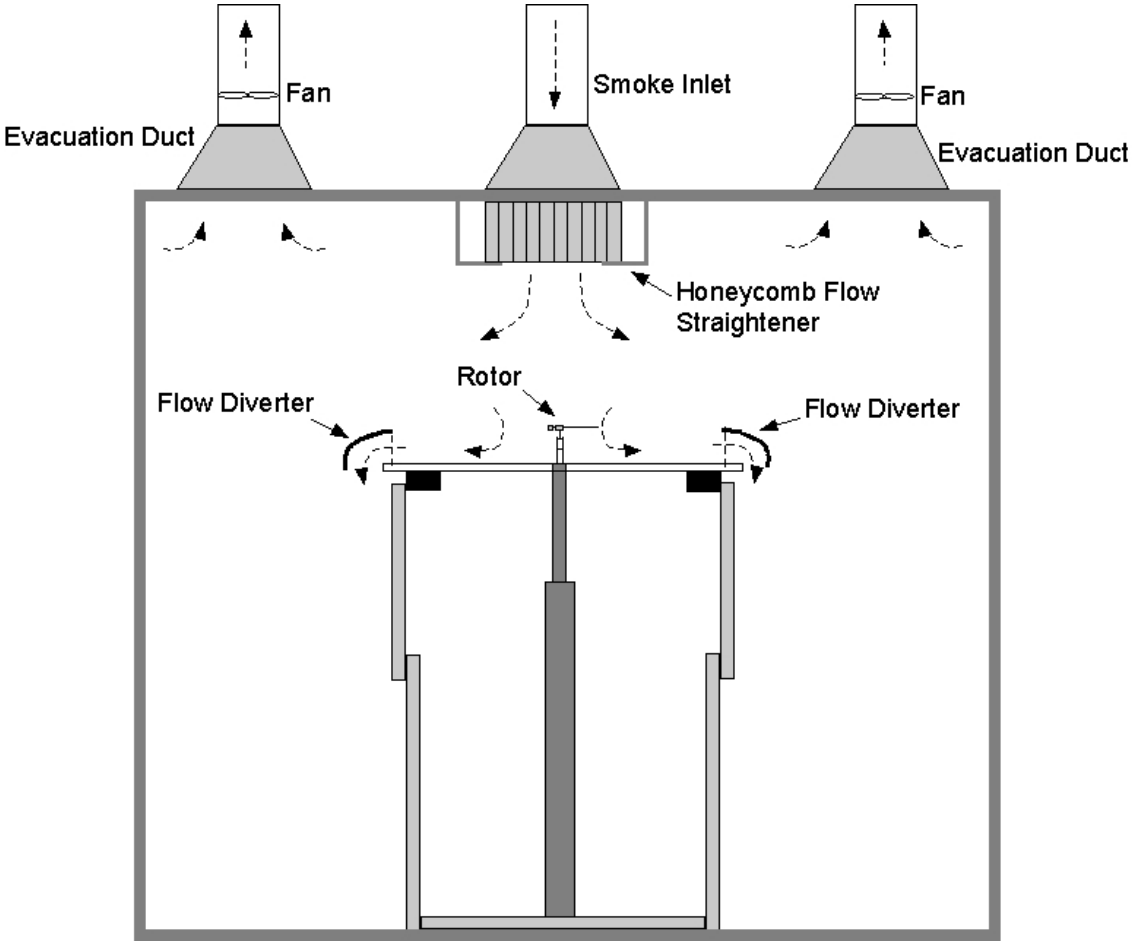

Figure 2.2: Schematic of the flow within the dust chamber.

minimal attenuation of the laser light and relatively unimpeded image capturing. To limit laser light reflections, specific portions of the chamber were lined with black cloth.

The experiments were performed in hover using a small rotor with a radius of 85 mm (≈3.346 in). The blade cross-section was a cambered flat plate airfoil of 3% thickness-to-chord ratio with a sharpened leading edge, which is aerodynamically preferable at the lower chord Reynolds numbers produced on this scale of rotor [41]. Experiments were conducted using both a 1- and 2-bladed rotor configuration mounted on a teetering hub system. The teetering hub allowed the second blade to be interchanged with

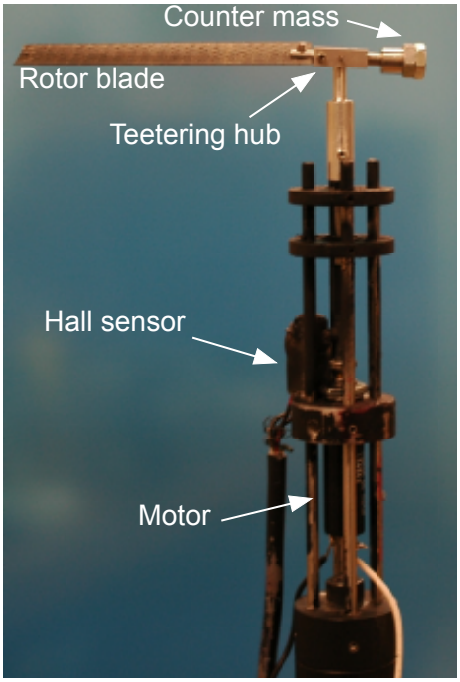

Figure 2.3: The rotor system used for the experiments shown in a 1-bladed configuration.

an equivalent counter-mass to produce a 1-bladed rotor configuration. Figure 2.3 shows a photograph of the rotor system in its 1-bladed configuration.

A schematic of the overall set-up used for the experiments is shown in Fig. 2.4. An adjustable height ground plane was arranged so that it was parallel to the rotor tip-path-plane. This ground plane was constructed out of a rigid, flat material that was painted matte-black to minimize laser light reflections. The rotor was placed above the ground plane to simulate hover in-ground-effect conditions. For the dual-phase experiments, a circular sediment bed comprised of glass microspheres was placed below the rotor, with further details of the particles used and the bed geometry being given later in this thesis.

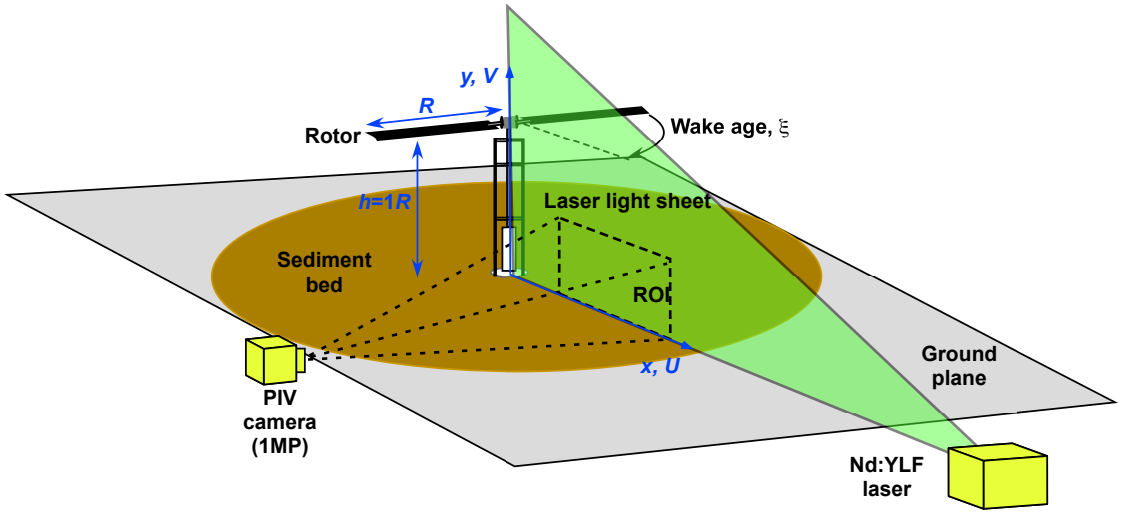

Figure 2.4: Schematic showing the experimental setup used to perform the PIV and PTV.

2.2 Instrumentation

The present study used particle image velocimetry (PIV) to measure the flow field. Specifically, a time-resolved particle image velocimetry (TR-PIV) system was implemented in which the CMOS camera and Nd:YLF laser were able to capture flow images at a frame rate of up to 3,000 Hz. However, to give sufficient camera resolution and acceptable image intensity, the maximum frame rate was limited to 1,500 Hz in the present work. This particular rate yielded good temporal resolution for the flow measurements, giving the ability to observe and analyze the transient development of the flow and the sediment particles that comprised the resulting dust cloud. The high frame rate also allowed for the observation of the evolution of turbulent eddies and secondary vorticity in the near-wall flow.

A Nd:YLF high-speed dual laser was used for both the flow visualization and for the PIV. The laser was capable of producing 20 mJ per pulse. The laser beams were

passed through a series of cylindrical lenses that turned the beams into diverging light sheets. They were then passed through a spherical lens to minimize the thickness of the sheets. These light sheets were oriented to intersect the rotor shaft axis and also remain perpendicular to the ground plane to illuminate all three regions of interest (ROI) that were examined in the present work. The axis of the camera was orthogonal to the light sheets and focused on the selected ROI. Both the laser and camera were digitally synchronized by a timing hub to capture precisely timed images. A schematic of the instrumentation setup is shown in Fig. 2.5.

2.3 Seeding and Sediment Particles

Submicron smoke particles were used as the seed particles for the carrier flow. The seed was produced by mixing high-pressure nitrogen and mineral oil in a heat exchanger, which brought the oil to its boiling point. The resulting fluid was ejected out of a nozzle into the ambient air where it rapidly cooled, causing the oil to condense into submicron sized particles. From a previous calibration [42], about 95% of these particles were 0.2 μm in diameter and were small enough to follow the flow without significant tracking errors.

The seed particles were also small enough to allow good phase discrimination from the sediment particles. A thresholding process used to separate the carrier and dispersed phase (explained in detail later) was dependent on the Mie scattering intensity from the carrier and dispersed particles. The smaller diameter seed particles give a different Mie scattering signature, allowing for successful phase discrimination between the carrier and

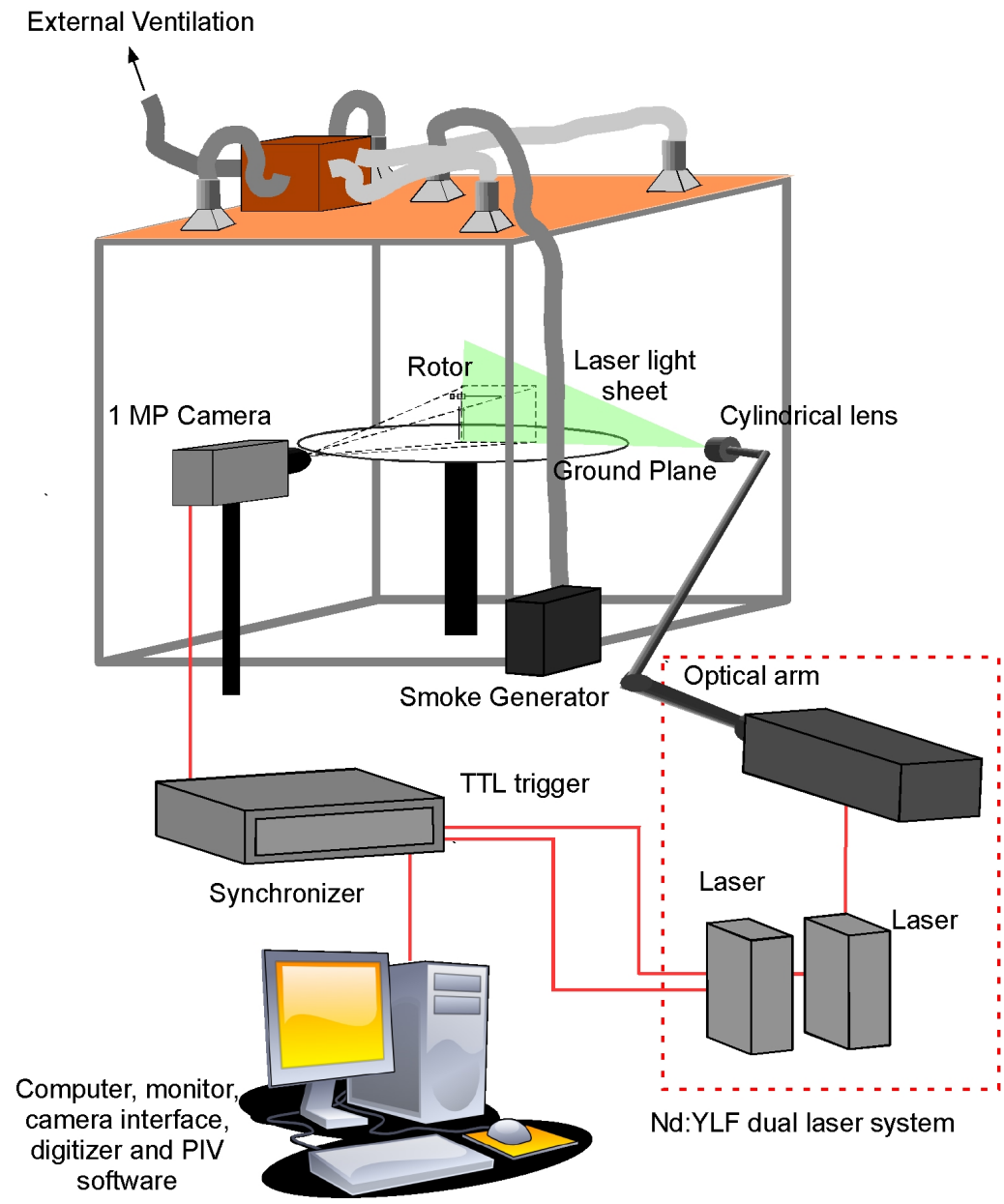

Figure 2.5: Schematic showing the instrumentation setup.

dispersed fluid phases. For the PIV studies, seed was introduced into the chamber before the beginning of the experiments and appropriately dispersed to provide the uniform concentrations that were required to make successful cross-correlations of the resultant images of the flow.

Another goal of the present experiments was to begin scoping the effects of the

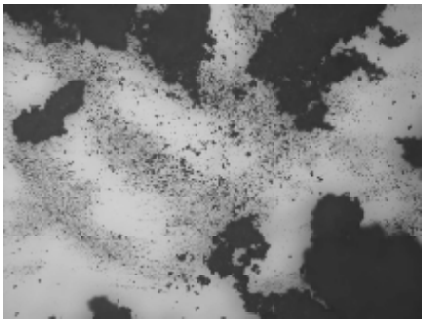

(a) 1–38 μm diameter microspheres

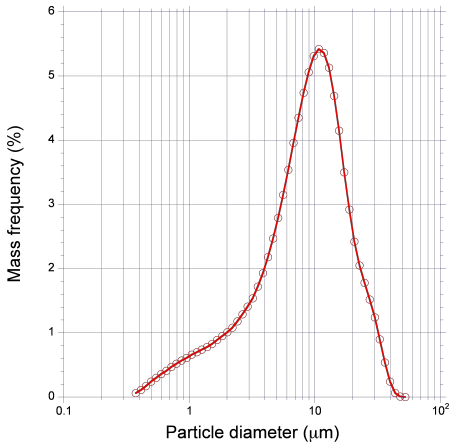

(b) 1–38 μm glass sphere size range

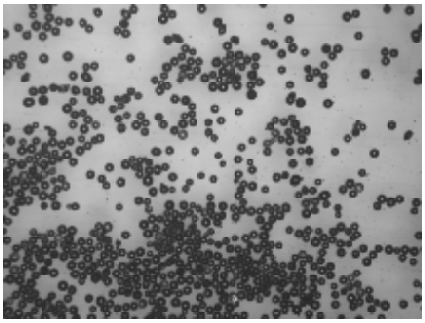

(c) 45–63 μm diameter microspheres

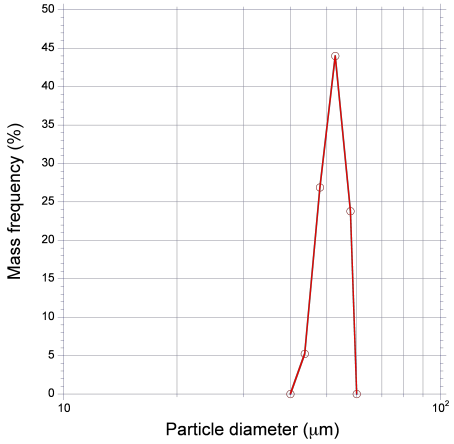

(d) 45–63 μm glass sphere size range

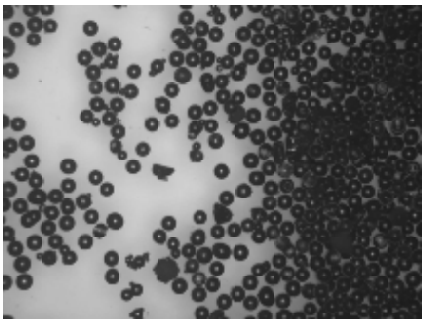

(e) 90–120 μm diameter microspheres

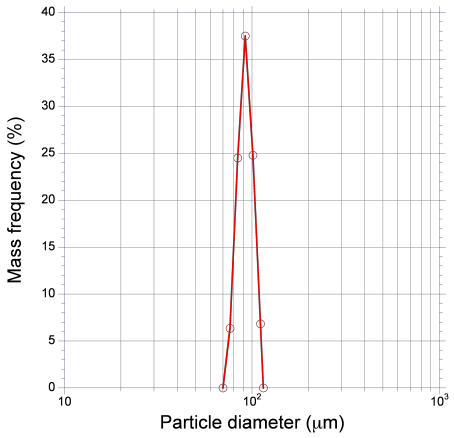

(f) 90–120 μm glass sphere size range

Figure 2.6: Microscope images and PSD of the glass microspheres.

size of the sediment particles on the mechanisms of uplift and dust cloud formation. In previous experiments, several different particle types were tested but using nonuniform sizes and more irregular (tetrahedral like) shapes [8]. To be consistent with the more commonly used dust cloud modeling assumptions, however, the present experiments used characterized glass microspheres in more uniform size ranges. Three different particle sizes were studied in the range of diameters: 1–38 μm, 45–63 μm, and 90–120 μm, which are shown in Fig. 2.6.

An X-ray sedigraph was conducted by an outside laboratory to obtain these size ranges. The technique involves measuring the gravity induced settling rates of different size particles in a liquid with known properties. The particle size can be calculated from the measured settling velocity using Stokes' law. This technique provided both the size of the particles and the mass frequency of each particle diameter used in the present work.

After the sensitivities of the dual-phase flow with respect to the different size ranges were established, the particles could be combined to achieve any desired combination of size distributions. However, most of the experiments in the present work were performed with the 45–63 μm diameter particles because this particular size range gave the best sediment mobility as well as good phase discrimination, and were better suited for identifying the various mobilization and uplift mechanisms. The particles were arranged below the rotor as a circular sediment bed of sufficient depth to prevent complete erosion during the test period.

2.4 Operating Conditions

The height of the rotor plane above the ground plane or sediment bed was varied from $2.0R$ down to as low as $0.25R$. Flows from both the 1- and 2-bladed rotor configurations were studied. Two operating conditions were used in this study, the first at a rotational frequency of 75 Hz yielding a tip speed of 40.06 ms^{-1} and Re_{tip} of about 40,000. The second was at a rotational frequency of 60 Hz yielding a tip speed of 32.04 ms^{-1} and Re_{tip} of about 35,000.

Changing the height of the rotor above the ground plane, the tip speed, and number of blades all individually effect the performance and aerodynamic parameters of the rotor system. Therefore, to perform a meaningful quantitative comparison between all the different rotor operating conditions, a metric that is kept constant between all test cases is required. One metric used in performance studies is rotor disk loading (DL), which is the ratio of rotor thrust to rotor disk area, to which the average downwash from the rotor can be related. Brownout, however, is a phenomenon that is also driven by effects other than average rotor downwash velocities, particularly the vortices [8]. The comparison metric chosen for the present study was the blade loading coefficient, C_T/σ, because the tip vortex strength is directly proportional to C_T/σ (see later). Keeping this parameter constant for all operating conditions (i.e., varying height, number of blades, and tip speed) also means that the lift generated by each blade is the same.

The thrust of the 2-bladed rotor at $1.0R$ and a blade pitch of 12° was measured and yielded a C_T/σ of 0.0136. The 2-bladed rotor has twice the solidity of the 1-bladed rotor. Therefore, to compare between the 1- and 2- bladed cases, the 2-bladed rotor was

run at twice the thrust of the 1-bladed rotor (i.e., both configurations were operated at the same tip speed to keep all parameters in C_T constant other than the thrust). To this end, the pitch of the 1-bladed rotor was set such that the rotor produced half the thrust at the same rotor tip speed, thereby keeping the values of C_T/σ constant. The rotor thrust was measured with a microbalance, which had an accuracy of ± 0.1 grams. As the rotor was lowered, more thrust was produced for a given tip speed, so to compensate the blade pitch was progressively reduced to produce the same target C_T/σ. For the cases with increased tip speed, the collective blade pitch was again lowered to produce the desired value of C_T/σ. Notice that while this approach keeps the value of C_T/σ constant (and hence keeps the strengths of the vortices the same), the average induced velocity through the rotor is increased approximately by a factor of $\sqrt{2}$, which also increases the mean flow at the ground plane. For a rotor (at least of the present design) is not possible to hold constant the strengths of the blade tip vortices as well as the mean flow velocities while maintaining tip speed and other parameters.

2.5 Regions of Interest

To quantify the aerodynamic environment below the rotor and near the ground, the flow field was dissected into several different regions. The three flow regions of interest (ROI) studied are shown in Fig. 2.7. These specific regions were identified from initial scoping experiments, converging to the three ROI's that were studied in detail in the present work.

ROI 1 allowed measurements to be made of a larger area of the flow field so as to

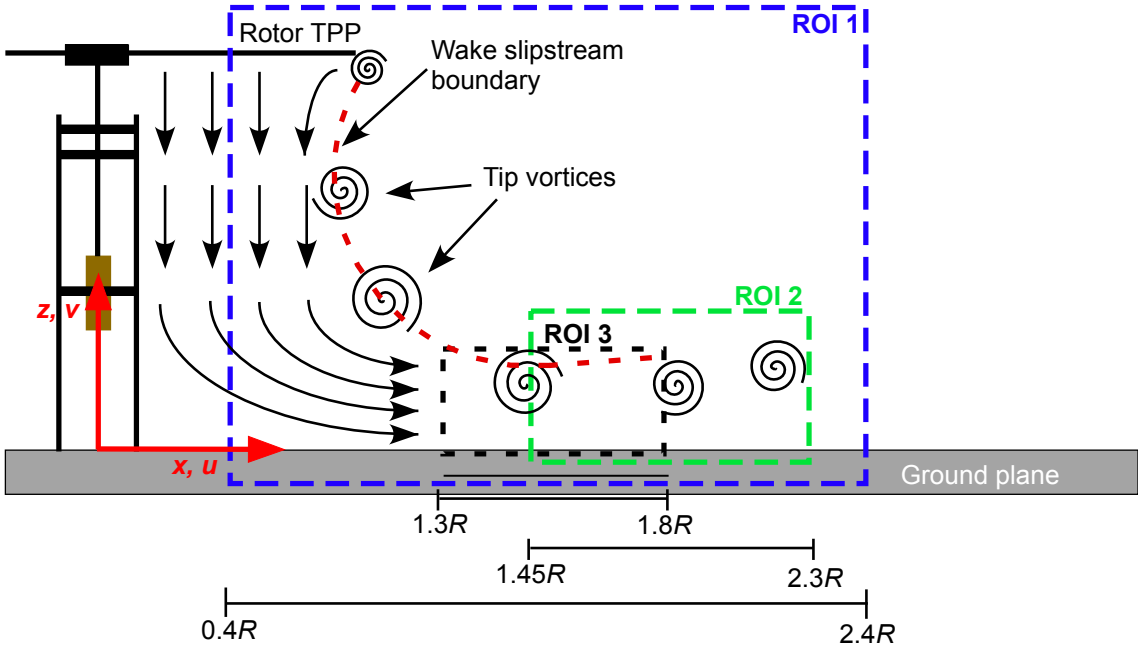

Figure 2.7: Schematic showing the different regions of interest (ROI) used in this study.

gain an overall understanding of what flow features were actually present in the rotor wake and in the near-wall flow at the ground plane. This region also provided a good field of view to compare the overall differences in the flow field in response to the changing rotor operational parameters (i.e., from the effects of the number of blades and rotor height above the ground plane). ROI 1 exposed what sediment dynamics needed to be studied in greater detail, and where the primary interactions between the rotor flow field and the sediment bed actually occurred. This region was used primarily for the single-phase and dual-phase flow visualization (FV) and the single-phase particle image velocimetry (PIV).

ROI 2 was used to identify and quantify the dust uplift mechanisms and the subsequent sediment dynamics in more detail, this location having been partly determined by outcomes from studies in ROI 1. This region was useful because it provided an opportunity to observe the evolution of the sediment and flow interactions near the ground plane

that ultimately lead to the formation of a dust cloud. ROI 2 was also used to assess the dependence of particle size on sediment uplift and mobility, and to examine how changing the particle characteristics effected the nature of the of particle uplift and suspension.

The smaller region of ROI 3 allowed for an even more detailed investigation into the fundamental sediment mobilization and uplift mechanisms. This region was used specifically to examine the fluid dynamics involved with each mechanism, and how the interaction between the local flow and the sediment caused it to be mobilized and uplifted. ROI 3 was also used to document the complex boundary layer fluid dynamics and particle-particle interactions that occurred near the sediment bed.

2.6 Tests Performed

Flow visualization (FV) was primarily performed in ROI 1 with the laser and camera firing at a frequency of 1,500 Hz. Tests were conducted with the rotor plane positioned at heights of z/R = 2.0, 1.5, 1.0, 0.75, 0.5, and 0.25 above the ground and/or sediment bed. The FV gave the ability to track the motion of the sediment particles as they were influenced by the rotor wake. The rotor was situated above the ground plane and single-phase flow experiments were performed for each rotor height. For the dual-phase experiments, the sediment particles were arranged in a 1 cm thick circular bed that was approximately 6 rotor radii in diameter. To prepare the bed, the sediment was poured in a confined area below the rotor. A straight edge was used to equally distribute the sediment and smooth the bed. For the FV and TR-PIV, image capturing began three seconds (about 200 rotor revolutions) after the rotor was started to allow for any transients in the flow to diminish.

The TR-PIV experiments were conducted in ROI 1 and ROI 2 with the laser and camera firing at a frequency of 1,000 Hz and in ROI 3 at a frequency of 1,500 Hz. The lower capture rate in ROI 1 and 2 was required to ensure sufficient laser intensity to illuminate the seed particles for a given f-stop on the camera lens. In ROI 1 and 2, single-phase experiments were performed for the 1- and 2-bladed rotors at heights of $1.0R$. In ROI 2, dual-phase experiments were conducted for both the 1- and 2-bladed rotors at a rotor height of $1.0R$ off the bed using three sediment sizes. In ROI 3, the 1-bladed rotor was placed at $1.0R$ above the sediment bed. For ROI 1, ROI 2, and ROI 3, lenses with focal lengths of 105 mm, 200 mm and 400 mm were used, respectively.

2.7 Particle Image Velocimetry (PIV)

For both the single-phase and carrier-phase experiments, particle image velocimetry (PIV) was used to measure the velocity fields. This laser based technique is a non-intrusive experimental method that can make 2-dimensional flow field measurements, even in areas close to a solid boundary such as the ground plane. The camera was synchronized with two laser pulses such that the laser pulses straddled the camera capture. This synchronization allowed enough light to enter the camera aperture, while simultaneously capturing two images over a very small time period apart (on the order of microseconds). The Δt between PIV image frames was chosen to be 20 μs for ROI 1 and ROI 2, and 15 μs for ROI 3.

Figure 2.8 shows a schematic of how the PIV software extracts the velocity measurements out of the two particle images. The first step is to take frames A and B, and

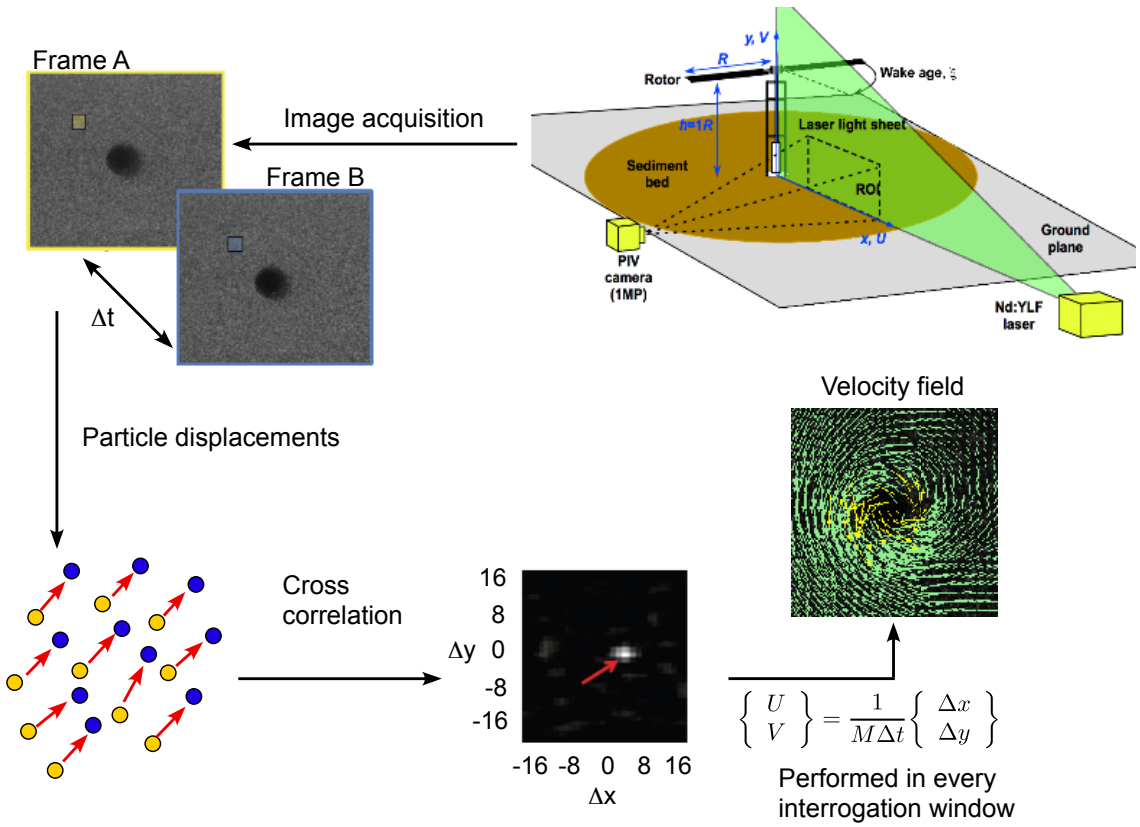

Figure 2.8: Schematic depicting the PIV cross-correlation process.

dissect them into interrogation windows. These windows are normally sized such that 5–15 seed particles are contained within each window, and that the particles move approximately a quarter of the window length in the primary direction of motion. The interrogation window must also be sized so that the contained seed particles translate mostly in one direction with the same magnitude with negligible flow curvature or shearing. The effects of flow curvature can manifest as velocity errors if the straddle time between laser flashes is too long [43].

For the same window in each frame, there are a number of particles in frame A that have translated to a new location in frame B after a pulse separation time Δt. The software

takes both frames and performs a cross-correlation, Φ_{fg}, according to the equation

$$\Phi_{fg}(m,n) = \sum_i \sum_j f(i,j) \times g(i+m, j+n)$$

with the intensity maps, f and g, corresponding to frames A and B respectively and m and n corresponding to the x and y pixel displacements. This process essentially takes frame B and translates it to each (i,j) coordinate in frame A, and then looks for the greatest similitude between the two frames. The translation in the i and j directions, in conjunction with the time difference Δt and magnification factor of the camera, are used to calculate a velocity vector for each interrogation. This process is repeated for all the interrogation windows in the image to produce the resultant flow field. The process is relatively computer intensive, especially with the large data sets that were typical of the present work. Notice that the images were spatially calibrated to provide the conversion factor between pixels and the engineering units required to calculate the flow velocities.

A square interrogation window with a deformation grid was implemented [44, 45], with the window size ranging from 40-by-40 pixels to 24-by-24 pixels, with the final size being small enough to properly resolve the swirl velocities and velocity gradients surrounding the vortex flows and in the wall-jet region at the ground. Masking was used for the regions adjacent to the ground to minimize reflections and to constrain the interrogation to begin just above the wall. Masking forces the interrogation windows within the area to yield zero velocity vectors. To further refine the cross-correlation, two passes of the Rohaly-Hart analysis were used. Each vector was validated using a universal median test and a signal-to-noise ratio of 2. Any image exceeding 5% spurious vectors of the total was removed from the analysis (the number of rejected vectors was typically low).

2.8 Phase Separation

Dual-phase image processing requires the use of a suitable phase separation algorithm before the velocities of the carrier- and dispersed-phases can be resolved using PIV and particle tracking velocimetry (PTV), respectively. In the present work, an intensity thresholding method was used to subtract the dispersed-phase from the carrier-phase, a schematic of the procedure being outlined in Fig. 2.9. For each raw image, an optimum intensity gray scale threshold was determined, and pixels above this threshold were subtracted from the original images thereby yielding separate carrier-phase and dispersed-phase images. The upper path of Fig. 2.9 shows the analysis of the carrier-phase using conventional PIV. Notice that the carrier-phase images had some masked "holes" in them from the subtraction of the dispersed-phase, therefore, a 3-by-3 local vector validation and interpolation procedure was performed to assess the validity of the resulting velocity vectors. The lower path of Fig. 2.9 shows the dispersed-phase analysis made using PTV, i.e., direct tracking of each particle (discussed next). Finally, the carrier-phase PIV and dispersed-phase PTV are recombined to produce measurements of the dual-phase flow field. This form of analysis yielded detailed quantitative measurements of both phases of the flow.

2.9 Particle Tracking Velocimetry (PTV)

The dispersed-phase does not contain the concentration of particles present in the carrier-phase and is, therefore, unsuitable for applying a cross-correlation method like PIV. Instead, each particle is individually tracked, as explained with the flow chart shown

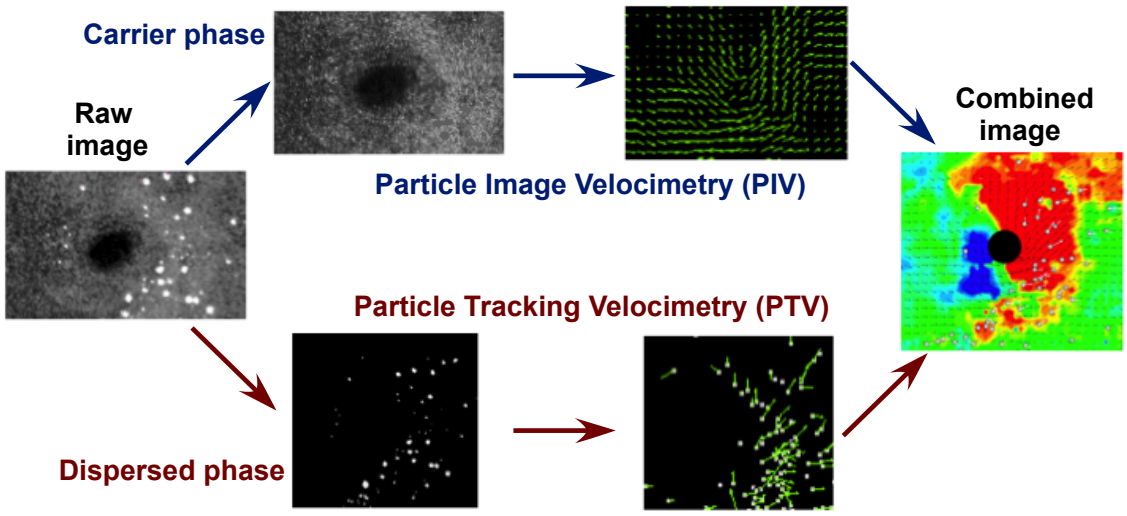

Figure 2.9: Dual-phase image phase separation and processing techniques.

in Fig. 2.10. Given an image with only the dispersed-phase present, the same intensity threshold used for phase separation is chosen to identify each individual sediment particle. For example, in a 3 x 3 pixel box surrounding one sediment particle, the software identifies whether the intensity, I, of each pixel is greater or less than the intensity threshold. If so, the algorithm identifies this pixel as potentially part of a sediment particle. Once this process has been completed for the entire image, the algorithm then identifies individual sediment particles in each frame. The selection process is based on a number of parameters, including pixel connectivity and minimum and maximum diameter.

After successful particle identification, an ellipse or circle is fitted over the pixels that correspond to the location of the particle. The PTV software then individually tracks each particle in frames A and B. This tracking is done by noting the pixel location in frame A and searching the surrounding pixels in frame B. The software identifies the "same" particle in frame B using the following parameters: total area, major and minor ellipse axes, Ferrets diameter (an average measure of the particle size), circumference,

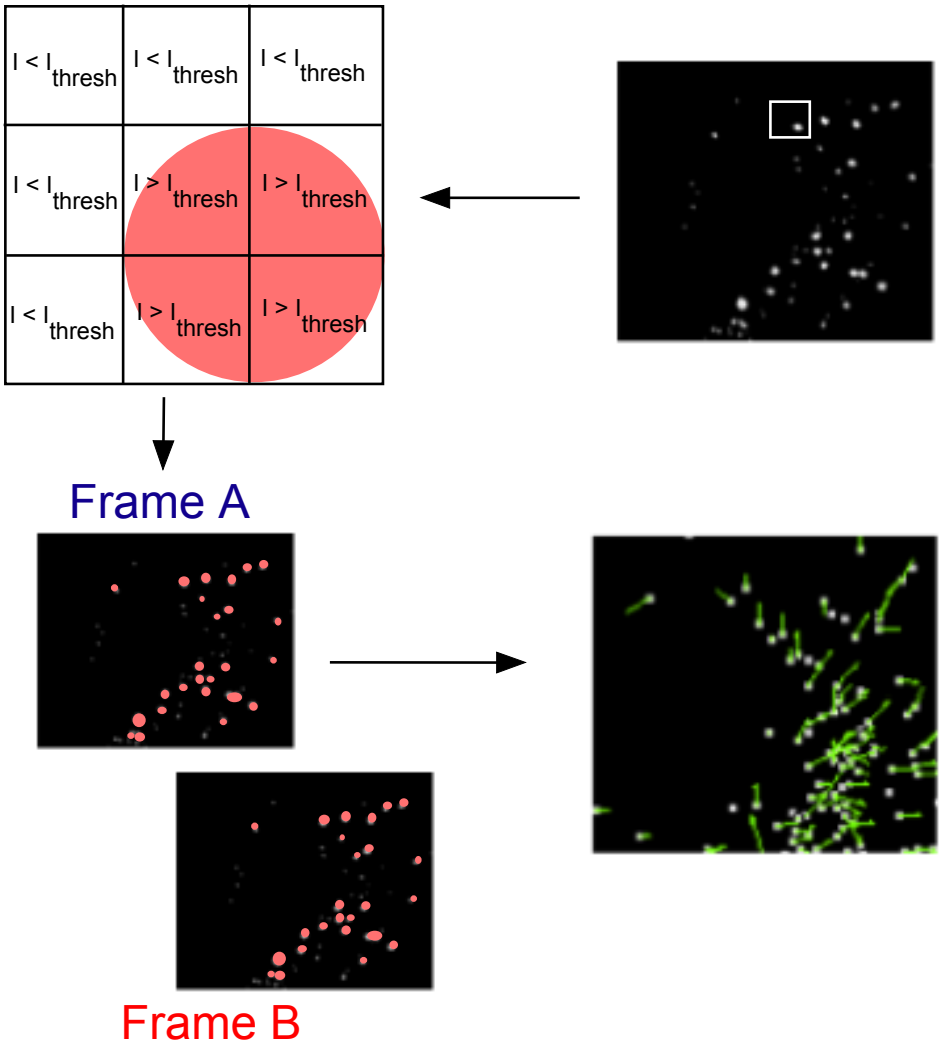

Figure 2.10: Schematic depicting the PTV algorithm used to extract the velocity of the dispersed phase.

intensity, background flow deviation, and number of surrounding neighbors. The velocity vector for each viable sediment particle in the dispersed phase is then obtained.

2.10 Technical Challenges in Data Acquisition

There were a number of technical challenges that arose while obtaining the measurements. One of the goals of this research was to find ways to either mitigate or alleviate these challenges, and to develop the most efficacious techniques for undertaking such dual-phase flow measurements in the dual-phase flow environment below the rotor at the ground. The various challenges encountered can be subdivided into two categories: software/computing issues and experimental methods.

One of first problems encountered was dealing with the large amounts of the data that were collected. Each flow field image was on the order of 1 MB, so at 1,000 images per run this amounted to 1 GB of data. The large data sizes caused two problems, the first being the transfer of data from the camera to the computer. This problem was solved by using memory buffer on the camera. The camera was equipped with software that is capable of capturing contiguous images at a high frame rate by storing the images on the onboard memory before transferring the data to the computer. The second problem is physical storage space needed on the computer, which was resolved by transferring the data onto multiple hard drives before processing and analysis.

While the available camera memory limited each run to 1,000 images, it was sufficient for statistical averaging but only providing 1 second worth of contiguous data per run. Each of the 1,000 images then had to be processed individually. For the single-phase runs, this process required processing each image through the PIV cross-correlation algorithm. To minimize the amount of time spent processing each image, the direct image correlator was replaced with a fast Fourier transform correlator, and the number of pri-

mary and secondary iterations were reduced from 3 and 2 down to 2 and 1, respectively. This procedure was found to minimize both the velocity errors and time it took for the vector fields to be processed. For the dual-phase runs, the signatures of the sediment had to be masked out of the image before the carrier-phase could be analyzed, adding an additional step and, therefore, additional time to the overall data processing.

Reflections were encountered within the dust chamber, an inevitable outcome of firing a high powered laser into a confined location. The Plexiglas used for the walls of the chamber were optically clear, but still produced some internal and surface reflections. For example, when the beam entered the dust chamber it reflected off the back wall and caused a "ghost" light sheet behind the original light sheet. This problem was mostly mitigated by lining the chamber with a black, non-reflective fabric.

The laser light sheet also has the tendency to reflect off of any solid boundary, including the ground plane; see Fig. 2.11. Figure 2.11a shows an unaltered raw image with laser reflections near the ground. The reflections in the near-wall region completely obscure the crisp seed particles that are needed to provide good correlations with the PIV. To help mitigate this problem, the laser was aligned such that the centerline of the light sheet was parallel to the ground plane. As shown in Fig. 2.11b, however, there are still some reflections from the wall. The final image, as shown in Fig. 2.11c, is the result of an additional post-processing step that has used a background subtraction algorithm, which collects the minimum intensity pixels over a number of images and subtracts it from each raw image. Finally, a background mask is placed over the ground region, thereby providing the resultant (final) image that is more suitable for the cross-correlation procedure.

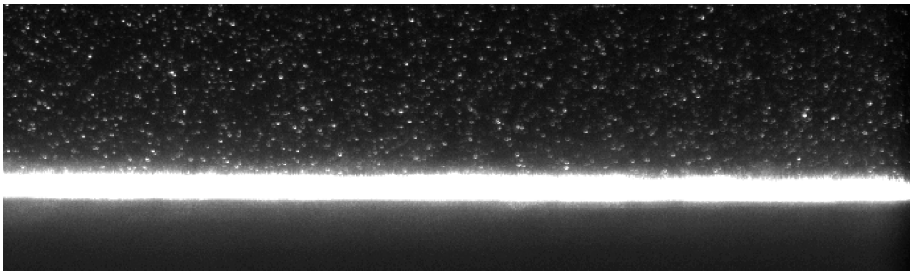

(a) Unaltered raw image

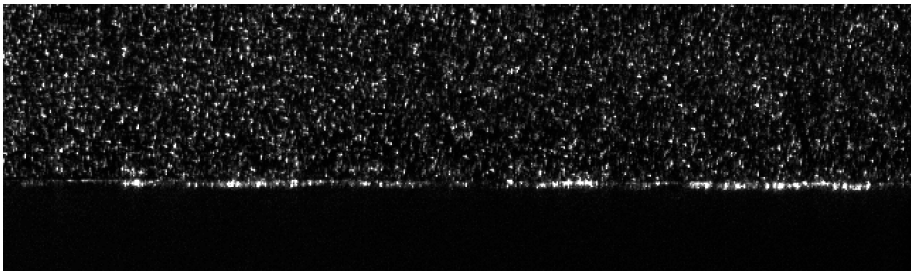

(b) Image taken after judicious laser alignment

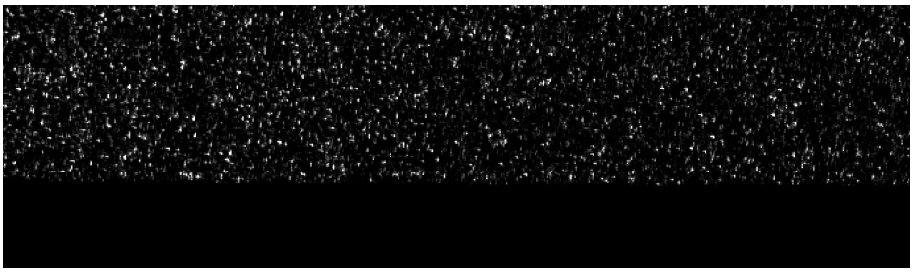

(c) Image after background subtraction and image masking

Figure 2.11: Process used to improve reflections at the ground plane.

As the vortices impinge upon the ground they slowly erode the sediment bed, causing a deflation region to form in the impingement zone, followed by a dune just downstream; see, for example, Fig. 2.12. This change in bed topology, when it becomes a significant fraction of the rotor dimensions, can also change the flow in some cases, and can encourage interactions between adjacent elements of the vortex filaments where otherwise there would be none. To this end, the rotor experiments were run as soon as the

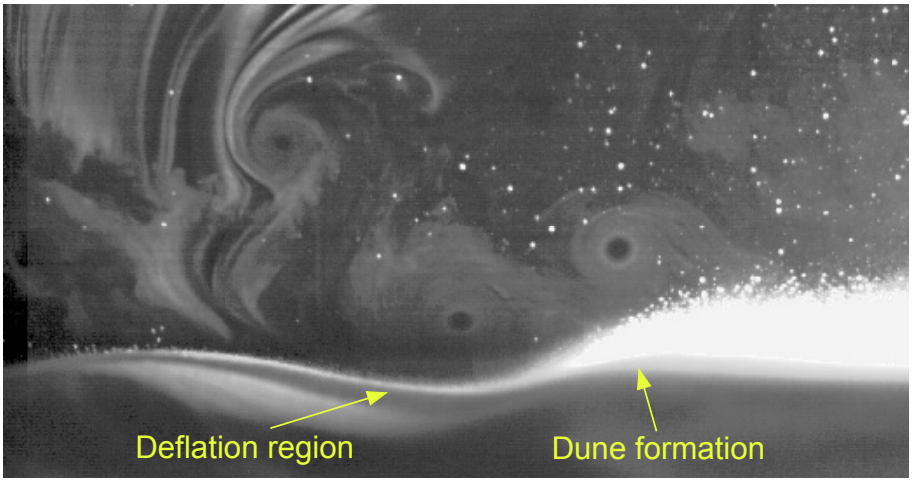

Figure 2.12: FV image showing the deflation and dune regions that can form over extended test times.

rotor was at its desired operating speed, not giving the rotor wake enough time to significantly erode the sediment bed.

Another consequence of running dual-phase experiments is in the particle identification process. The nature of the brownout problem is that a lot of sediment is typically uplifted and suspended; see Fig. 2.13. However, if these particles become too highly concentrated in the flow, the particle identification software cannot individually identify each particle in the dispersed-phase because the reflections from the particles begin to saturate the overall image. The rotor parameters and operating conditions were selected such that the dispersed phase was always relatively dilute, thereby mitigating this problem.

One of the challenges associated with the thresholding method of phase separation are the "holes" remaining in the carrier phase image; see Fig 2.14. While these holes were masked, sometimes they will provide a correlation in the PIV if they become large enough. For most of the present experiments, a simple 3 x 3 interpolation grid was found

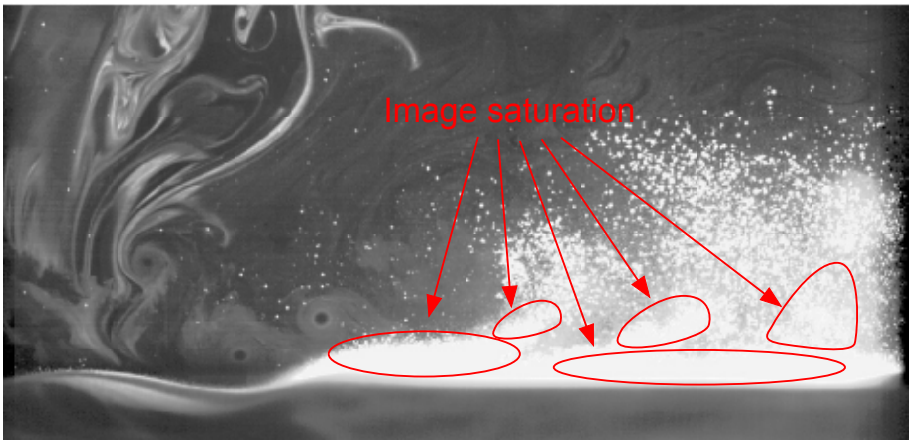

Figure 2.13: Dual-phase image depicting the light saturation caused by too many uplifted and suspended sediment particles.

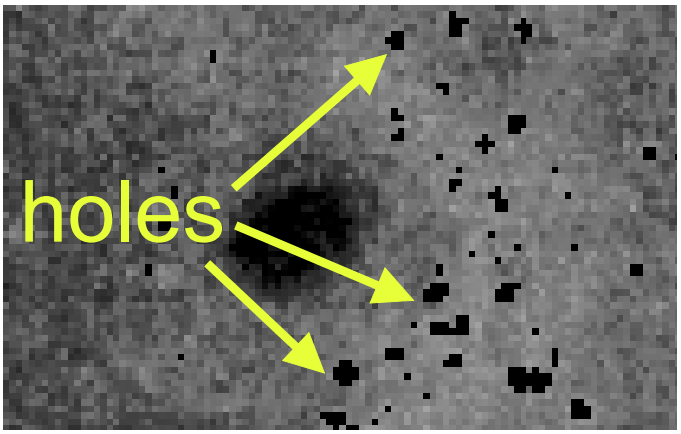

Figure 2.14: Phase separation “holes” in the carrier-phase after thresholding has been performed.

to be sufficient to fill in all of the holes in the data matrix and allow for successful cross-correlations of the carrier phase.

2.11 Uncertainties in the PIV Measurements

Sources of uncertainty in the flow measurements using PIV include tracking errors of the tracer particles, background noise, interrogation window size, pulse separation time, and laser light reflections. Tracer particle errors are a result of the seed particles slipping or not perfectly following the flow. However, in the present work, this source of error was very small. Background noise is a result of noise in the camera signal that can cause artificial intensities in the raw image that result in inaccurate correlations. To limit this error, a stringent signal-to-noise ration was used to assess the validity of each vector. Interrogation window size and pulse separation time are chosen such that there is minimal flow curvature or shearing within each window. However, in a flow with significant vorticity there is always some deviation of the flow in each interrogation window, so an image deformation approach was implemented to help alleviate this source of error. Laser light reflections, similar to background noise, obscure the tracer particles in the raw image resulting in a complete loss of signal or erroneous vectors. The amalgamation of all these sources of error resulted in approximately 4.7% error in the pixel displacements and 4.9% error in the velocity measurements, which was quantified using the equation

$$\Delta U = \sqrt{\left(\varepsilon_{\Delta x}\frac{\partial U}{\partial \Delta x}\right)^2 + \left(\varepsilon_{\Delta t}\frac{\partial U}{\partial \Delta t}\right)^2 + \left(\varepsilon_{M}\frac{\partial U}{\partial M}\right)^2}$$

where $\varepsilon_{\Delta x}$, $\varepsilon_{\Delta t}$, and ε_{M} are the errors associated with pixel displacement, pulse separation time, and magnification factor respectively.

2.12 Particle Identification Errors in PTV

There are a number of limitations that hinder the identification of all the imaged particles in PTV. The majority of the unidentified particles arise because the particle do not scatter enough light or is not completely within the laser light. There are also errors in the particle tracking as a result of the parameters used for identification and tracking. In particular, the calculation of the centroid of the particle (X_c, Y_c), which had an error of up to 5 pixels in each dimension. With the centroid defined as $R_c = (X_c, Y_c)$ and the length $|R_c| = X_c + Y_c$, the uncertainty is

$$\Delta|R_c| = \sqrt{\left(\varepsilon_{X_c}\frac{\partial|R_c|}{\partial X_c}\right)^2 + \left(\varepsilon_{Y_c}\frac{\partial|R_c|}{\partial Y_c}\right)^2}$$

where ε_{X_c} and ε_{Y_c} are the uncertainties in X_c and Y_c, respectively. The centroid uncertainty was calculated to be approximately 1.0% of the particle location.

2.13 Summary

This chapter has described the experiments that were performed in the present research. The dust chamber, rotor system, ground plane, seeding, sediment particles, and PIV/PTV system were all described. The flow visualization and PIV methods used were explained in detail. The present work used time-resolved particle tracking velocimetry (PTV) to study the dual-phase flow environments below a hovering rotor at varying heights with different numbers of blades. Different size ranges well-characterized of glass microspheres were used to create the sediment bed. For the dual-phase experiments, a phase separation algorithm was used to analyze the carrier- and dispersed-phases sepa-

rately in three regions of interest. The technical challenges involved in data acquisition have also been described. Estimates of the various sources of errors in the measurements were discussed.

Chapter 3

Results and Discussion

This chapter discusses the results from the experiments that were performed. The chapter is organized such that the single-phase results using flow visualization (FV) are discussed first, followed by the PIV results. The dual-phase results are then discussed, again starting with FV followed by PIV. The dual-phase results include a detailed analysis of the sediment mobilization and uplift mechanisms, and an exposition of how the rotor height of the ground plane, two blades versus one blade, and the size of the sediment, can effect the nature of the resulting dual-phase flow environment.

3.1 Single-Phase Results

A prerequisite toward understanding the dual-phase brownout environment is to gain an understanding of the characteristics of the single-phase flow (i.e., the carrier-phase). To this end, flow visualization (FV) was used to examine the various flow interactions and the detailed time-histories of the evolving flow structures that were present in the rotor wake. The FV was performed by introducing concentrated regions of seed above the rotor such that it was directly entrained into the salient features of the rotor wake. The brighter and denser concentrations of seed served to identify the main structures of the rotor wake, such as the tip vortices and the vortex sheets. For the time-resolved experiments, continuous filaments of more concentrated seed were needed to bring out the salient flow

features. For example, the presence of a blade tip vortex was easily identified by a distinct dark "void" regions (caused by small Coriolis and centrifugal forces) in the FV images. However, such regions do not imply that the flow there is completely unseeded. It is also important to note that any differences seen in the images in regard to the relative size of such dark regions should not be used to directly imply the strength of the vortices or any other differences in their flow characteristics.

3.1.1 Rotor Wake

As the blades pass through the imaging plane, the signature of the helicoidal vortex filaments that trail from the tips of each blade into the rotor wake can be seen. For example, Fig. 3.1 shows a schematic for a case when the rotor is operating out-of-ground-effect (OGE) (also recall Fig. 1.5 in Chapter 1). The rotor does work on the air to produce thrust, and so an increase in its velocity through the rotor is produced and the downstream wake contracts as a consequence. At further downstream distances, however, the wake begins to expand slowly as viscous and turbulent diffusion progressively reduces the axial slipstream velocities of the flow inside the wake boundaries.

The helicoidal vortex filaments that trail from the blade tips are seen to convect along the slipstream boundary that separates the relatively high velocities inside the rotor wake boundary from the quiescent flow outside the wake boundary. These vortices are seen to have mostly smooth laminar cores, devoid of the small eddies and turbulence that are present in the surrounding flow. Figure 3.1 shows that after only 2–3 rotor revolutions, the tip vortices have begun to spin-down under the action of viscosity and turbulence.

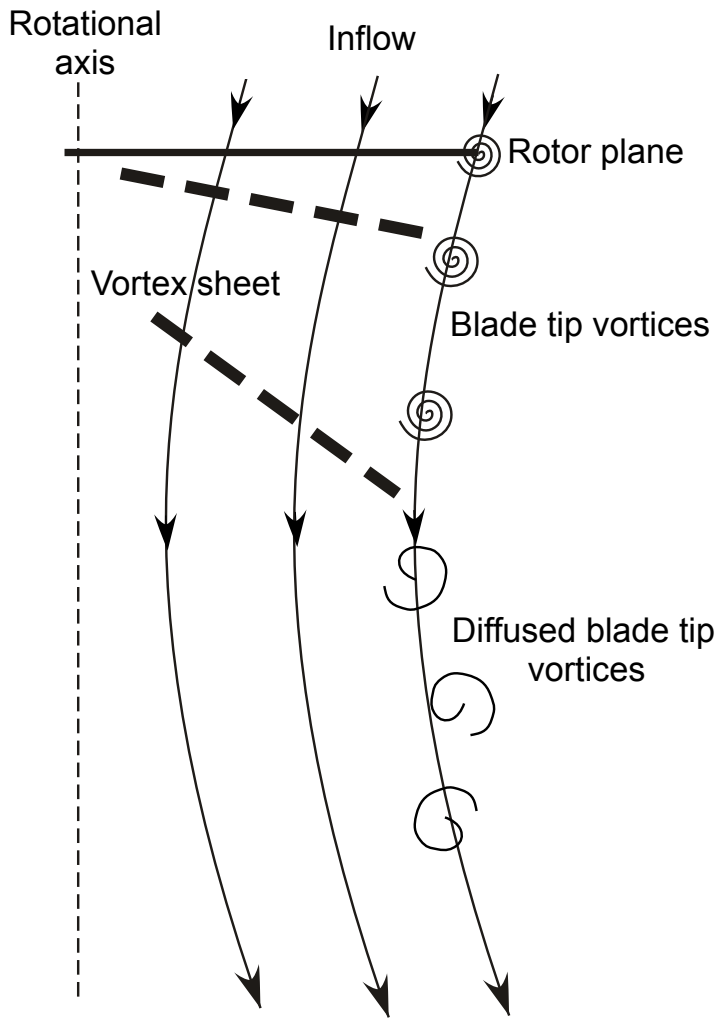

Figure 3.1: Schematic of a rotor operating OGE at $z/R = \infty$. $\psi_b = 0^\circ$.

The older vortices in the far wake were also more susceptible to the development of instabilities and the pairing of adjacent turns of the helical wake.

The schematic in Fig. 3.2 shows that when the rotor is operated in proximity to a ground plane i.e., in-ground-effect (IGE), the structure of the wake is very different to that found in hover. The rotor wake in this case is forced to turn sharply as it approaches the ground plane and it then expands radially outward. Compared to the OGE condition, it is also apparent that the flow under the rotor contains discrete vortical structures that

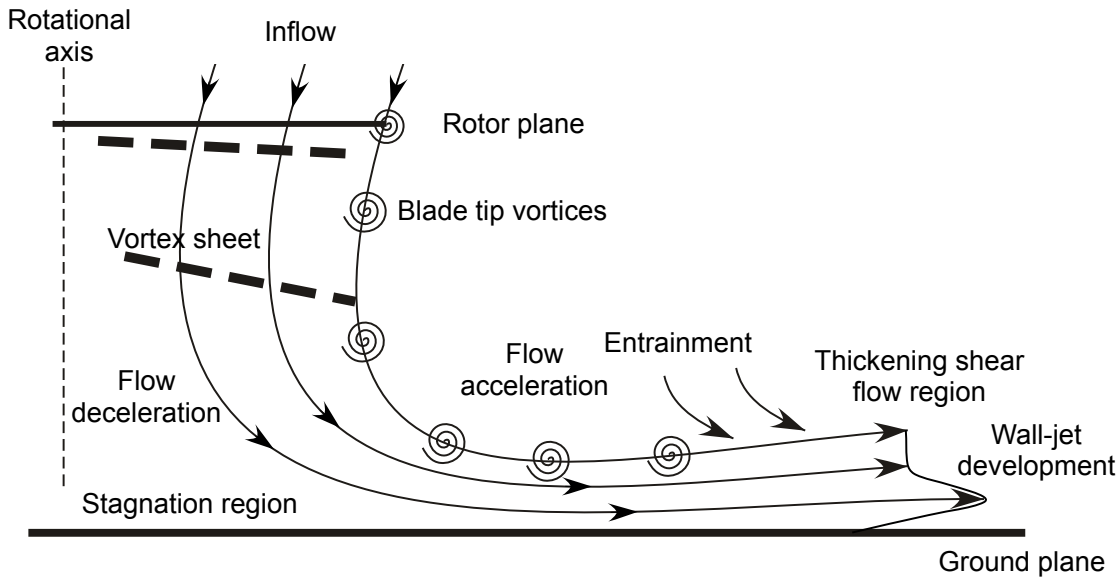

Figure 3.2: Schematic of a rotor operating IGE at $z/R = 1.0$ above a ground plane. $\psi_b = 0°$.

persist to much older wake ages than was found in hover.

3.1.2 Behavior of the Tip Vortices

The rapid expansion of the rotor wake when it encounters the ground causes the vortex filaments to stretch along their lengths as they convect radially outward. This process reintensifies their vorticity which, in turn, increases their swirl velocities. This process also causes the vortices to persist in the flow to much older wake ages [21, 46], in this case to 4–6 rotor revolutions old. Stretching occurs because of volume conservation of the fluid elements; lengthening causes a thinning of the fluid elements in the directions perpendicular to the stretching direction [46], thereby reducing the radial length scales over which the associated vorticity is distributed. The vorticity, is therefore, confined to a smaller area of the flow, the consequence being higher swirl velocities that are typical

of vortices at younger wake ages. As will be further described, this is an important fluid mechanics behavior that ultimately participates in the uplift of sediment and, ultimately, in the brownout problem.

Near the ground plane, the vortices interact with the flow there. They are sheared by the velocity gradients in the flow near the ground plane, which causes them to begin to diffuse more rapidly. The flow further downstream consists of residual vortical elements and larger turbulent eddies. If the vorticies are not sheared and/or do not diffuse at a fast enough rate, then the vortex filament eventually thins to a point were it is more susceptible to the development of instabilities or to a rapid breakdown. Such instabilities (if they occur) manifest as wave-like perturbations along the lengths of the vortices. If such perturbations become sufficiently large enough in amplitude, then they can cause an element of the vortex filament to burst, rapidly spreading the contained vorticity and reducing the associated swirl velocities [40].

3.1.3 Wake Sheet

With the passing of each blade, it was noted that a wake sheet was also trailed off each blade. This wake sheet is created by the merging of the boundary layers on the upper and lower surfaces of the blade, and comprises smaller levels of vorticity. These turbulent vortex sheets (which are actually comprised of counter rotating Taylor-Görtler vortex pairs) convect under the influence of a range of downwash velocities because they span over the length of the blades. In fact, it was clear from the flow visualization that each wake sheet convected downward relatively faster than the tip vortex to which it was

originally connected, eventually overtaking it and interacting with an older tip vortex in the flow.

As each vortex sheet approached the ground plane, it was noted that the outboard portion of the sheet becomes ingested by an older tip vortex and at least part of the turbulence becomes relaminarized inside the vortex core. The relatively small eddies in the wake sheet are entrained in the laminar vortex core and become stretched and flattened during this process, effectively undergoing a relaminarization process; see also Ref. 21 for a detailed description of this behavior. The remnants of the turbulent wake sheet that persists to the ground then begins to interact and mix with the developing flow at the ground, as shown in Fig. 3.3.

As the wake sheets approach the ground, it was noted that they also have a propensity to become unstable and roll over on themselves. Some of the associated turbulence contained in the sheets continues to be relaminarized by the nearly tip vortices, while other turbulent flow structures persist in the wake and contribute to defining the flow conditions at the ground plane (1.e., the wall). Upon reaching the wall, the remnants of the wake sheet are forced to expand radially outward with the remainder of impinging rotor wake, and the net flow then constitutes the developing conditions at the wall.

3.1.4 Flow at the Wall

The flow at the wall below the rotor takes on the characteristics of an expanding wall-jet with a boundary layer below; see the discussion later in this thesis and also Ref. 21. The ingestion of the wake sheet introduces a significant amount of turbulence

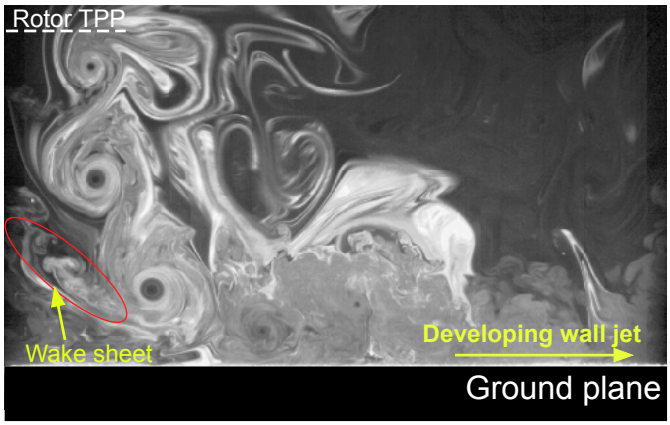

(a) Time step 1, $\psi_b = 216°$

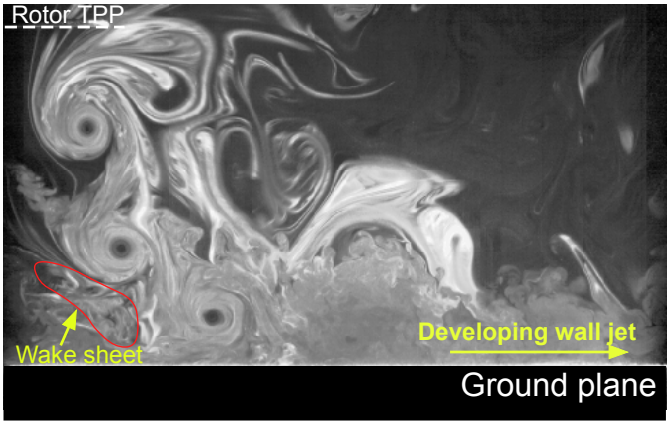

(b) Time step 2, $\psi_b = 0°$

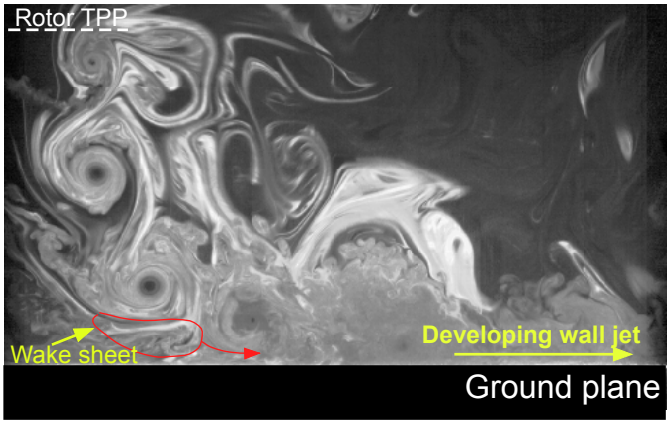

(c) Time step 3, $\psi_b = 126°$

Figure 3.3: Sequence of images depicting the evolution of the wake sheet as it is interacts with the flow at the ground and is ingested by the turbulent flow there ($z/R = 1.5$).

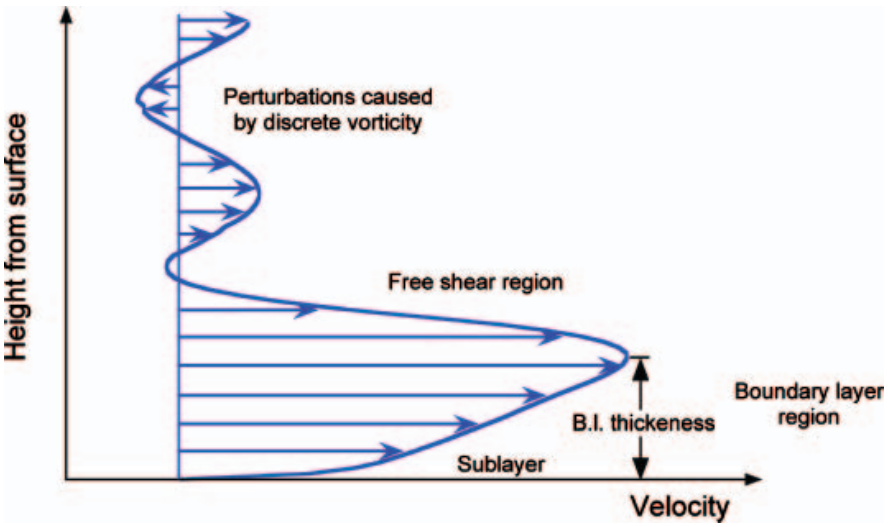

Figure 3.4: Schematic of the wall-jet like flow below a hovering rotor.

into the developing wall-jet flow; see Fig. 3.3. As the wake expands radially, the wall-jet thins and its average velocity increases to conserve momentum and mass. Eventually, the viscous and fluid shearing forces become dominant, and the energy in the flow is diffused and dissipated, causing the wall-jet to thicken and slow. A schematic of this wall-jet flow shown in Fig. 3.4

3.1.5 Effect of Rotor Height

Of significant interest in the present work were the effects of the rotor height above the ground plane (i.e., the value of z/R) on the developing wake structures, and how rotor height affected the flow environment at the ground. To this end, Fig. 3.5 shows FV results for the 1-bladed rotor at the first operating condition (rotational frequency of 75 Hz) for seven different values of z/R above the ground.

At $z/R = 2.0$, the wake shows many of the characteristics of the rotor when it oper-

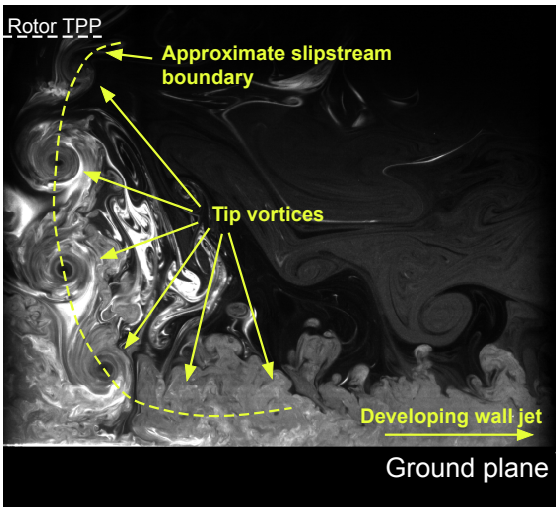

(a) 1-bladed rotor at $z/R = 2.0$

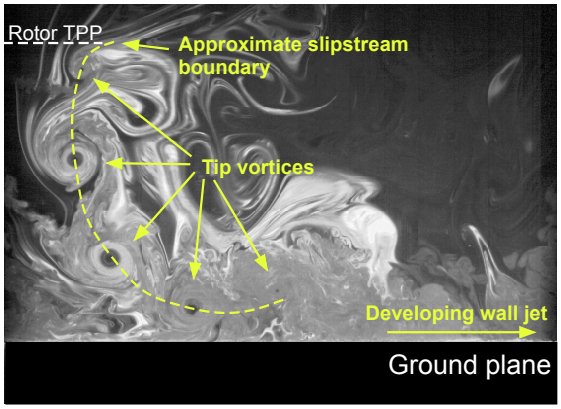

(b) 1-bladed rotor at $z/R = 1.5$

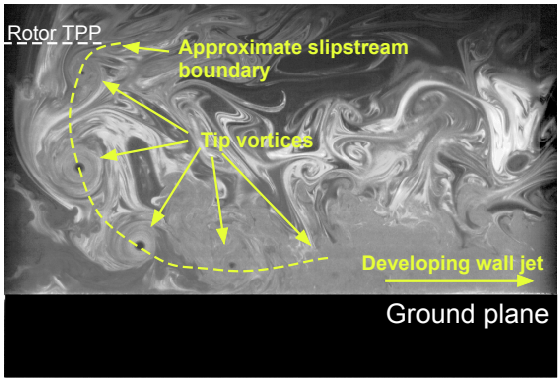

(c) 1-bladed rotor at $z/R = 1.25$

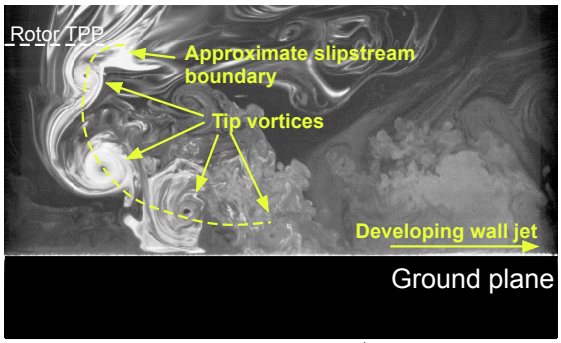

(d) 1-bladed rotor at $z/R = 1.0$

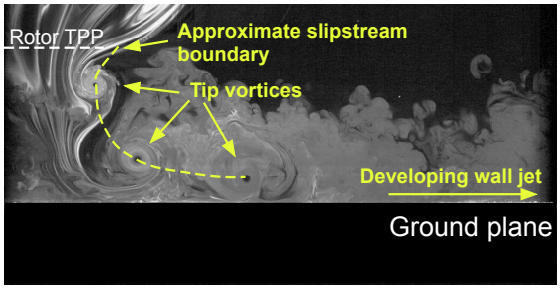

(e) 1-bladed rotor at $z/R = 0.75$

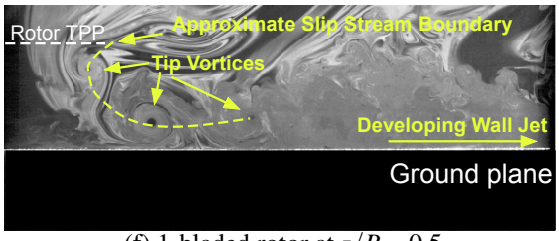

(f) 1-bladed rotor at $z/R = 0.5$

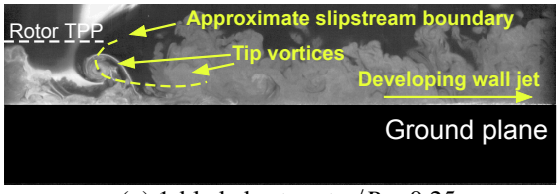

(g) 1-bladed rotor at $z/R = 0.25$

Figure 3.5: Single-phase flow visualization for the 1-bladed rotor at various heights.

ates OGE, the tip vortices undergoing a certain amount of diffusion before they reach the ground, with the wake initially contracting and then slowly expanding because of viscous shearing and the eventual interaction of the wake with the ground. The resulting flow over the ground plane in this case is highly turbulent because the remaining vorticity from the tip vortices and the wake sheet are now ingested into the developing wall flow, causing significant fluctuations in the flow velocities there.

When the rotor was lowered to $z/R = 1.5$, the wake contracts below the rotor and then convects more quickly outward along the ground plane, expanding radially and thinning in the vertical dimension. In this case, there was evidence of the stretching and straining of the vortices to the extent that they now persisted in the flow to relatively older wake ages (about 4 or 5 rotor revolutions in this case). As previously mentioned, stretching the vortex filaments maintains (and can even intensify) their vorticity. A rotor height of $z/R = 1.5$ is the first condition at which the vortices are close enough to the ground such that any initial diffusion of the tip vortices is counteracted by their stretching and straining.

The detailed time-histories of the trailed tip vortices were examined to help understand their fluid dynamic interactions at the ground plane, mainly because their behavior participates in the uplift of sediment (discussed later). To this end, as the rotor was further lowered toward the ground plane the frequency at which vortex-vortex interactions occurred (i.e., the susceptibility to pairing) was found to increase. An associated fluid dynamic mechanism here is the merging of adjacent vortices, i.e., the viscous merging of the adjacent turns of the helicoidal rotor wake. This merging process was found to begin at a rotor height of $z/R = 1.5$ and arises because of the mutual interactions and pairing

between closely spaced turns of the helicoidal vortex filament. The consequence of this behavior (in most cases) is that the viscous merging of the net vorticity field causes intensification of the respective upwash and downwash regions in the combined vortical flow. As the rotor height was lowered to z/R = 1.25, 1.0 and 0.75, the intrinsic aperiodicity in the flow became increasingly evident and the susceptibility of vortex merging interactions occurred more frequently.

Further details of this type of vortex merging process is shown by the sequence of FV and PIV images in Fig. 3.6. In this case, an older vortex enters the imaging frame, which is then followed by a younger vortex (180° of wake age younger in this case). The older vortex begins to roll above the younger vortex (i.e., pairing with a younger vortex). The younger vortex then convects directly underneath the older vortex such that the upwash and downwash regions of both vortices begin to merge with one another, creating a more powerful flow that contains the combined circulation that was initially present in both of the original vortices.

It is important to note that while both original vortices from the blades had fairly laminar cores, the combined vortex flow has been formed by the viscous merging of the flows and does not have much of a laminar core; in fact, the observations suggested that this was rarely the case. The merging of two adjacent vortices is an unsteady phenomenon and occurs in the presence of a shear layer (the slipstream boundary between the turbulent wall-jet and quiescent flow). This merging process inevitably contains some of the surrounding turbulence which, in conjunction with the merging process itself, is not conducive to the suppression of turbulence in the vortex core region.

Secondary vortical flows in the wall region were also produced in most cases, this

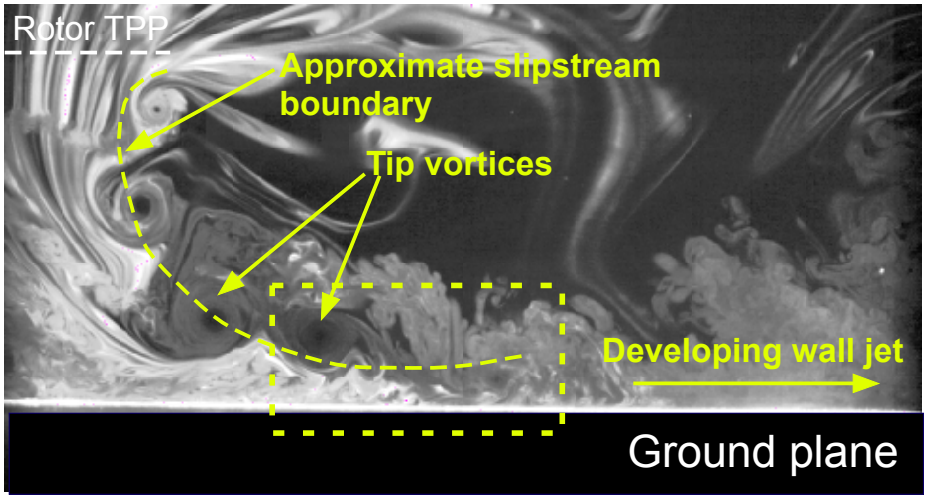

(a) FV at time step 1, $\psi_b = 72°$

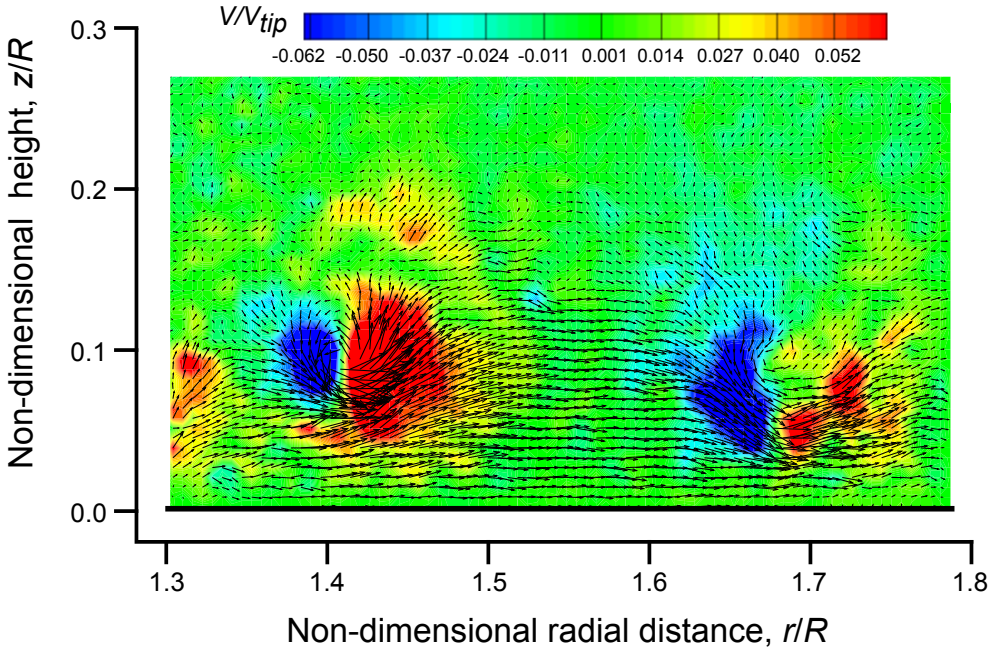

(b) PIV at time step 1, $\psi_b \approx 174.6°$

Figure 3.6: Flow visualization in ROI 1 and PIV in ROI 2 showing the time-history of the vortex merging process.

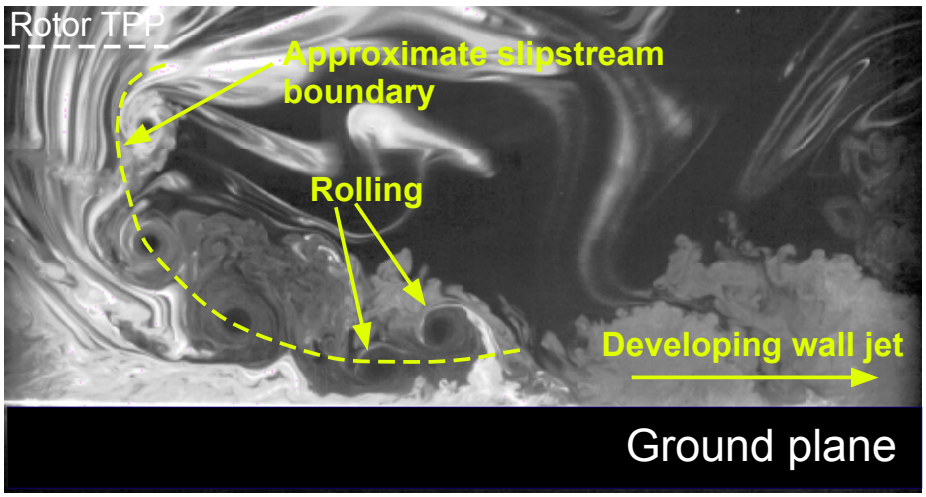

(c) FV at time step 2, $\psi_b = 288°$

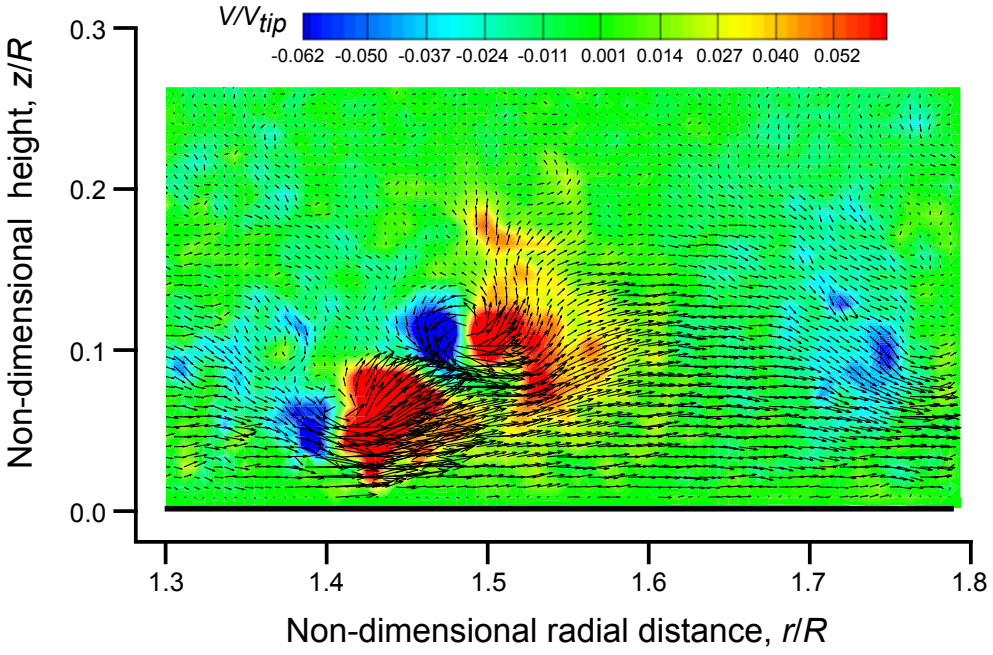

(d) PIV at time step 2, $\psi_b \approx 261°$

Figure 3.6: (Cont'd) Flow visualization in ROI 1 and PIV in ROI 2 showing the time-history of the vortex merging process.

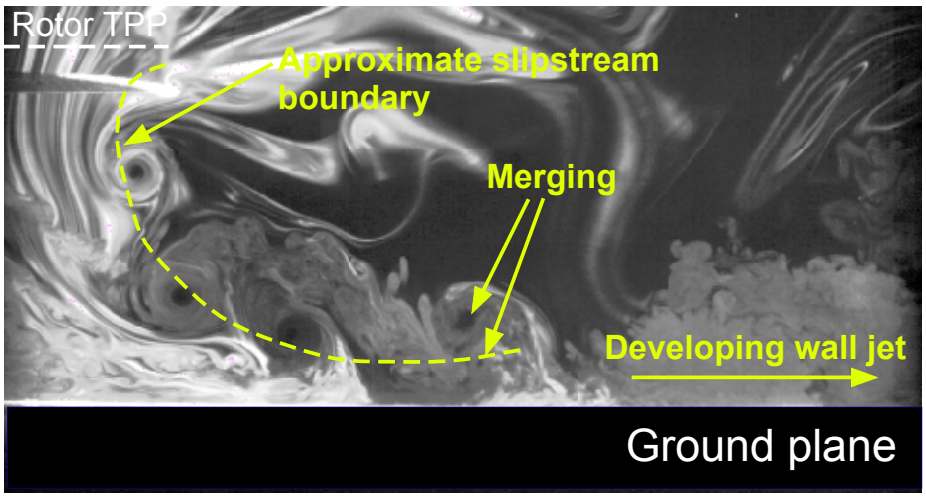

(e) FV at time step 3, $\psi_b = 18°$

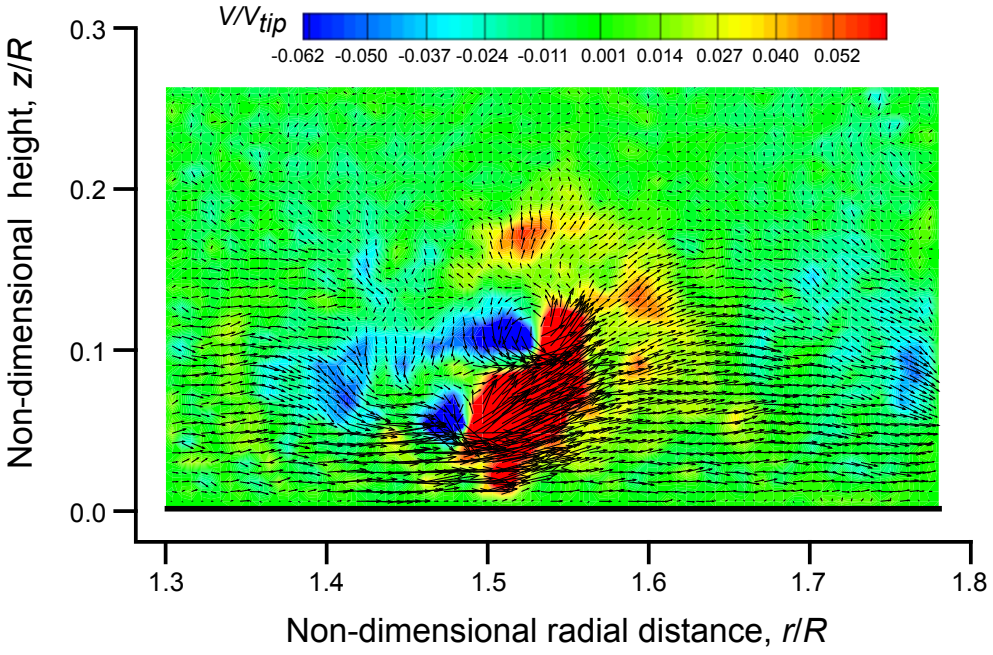

(f) PIV at time step 3, $\psi_b \approx 304.2°$

Figure 3.6: (Cont'd) Flow visualization in ROI 1 and PIV in ROI 2 showing the time-history of the vortex merging process.

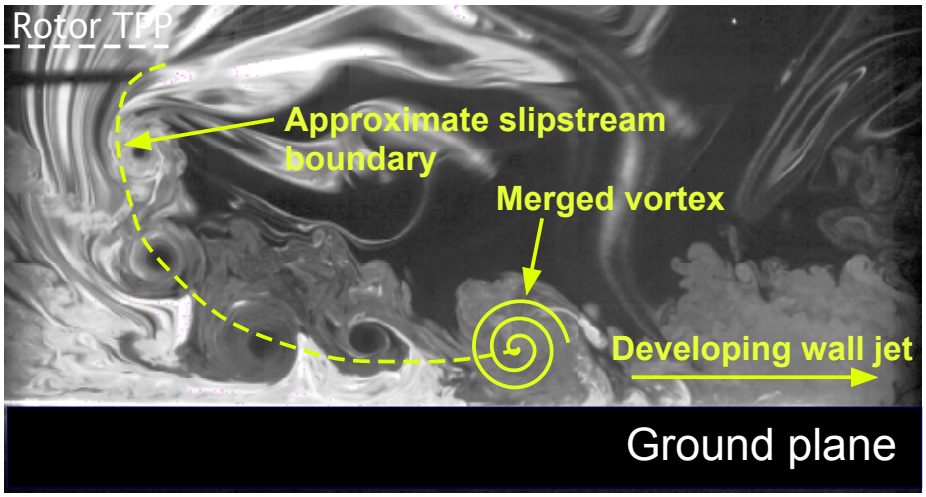

(g) FV at time step 4, $\psi_b = 144°$

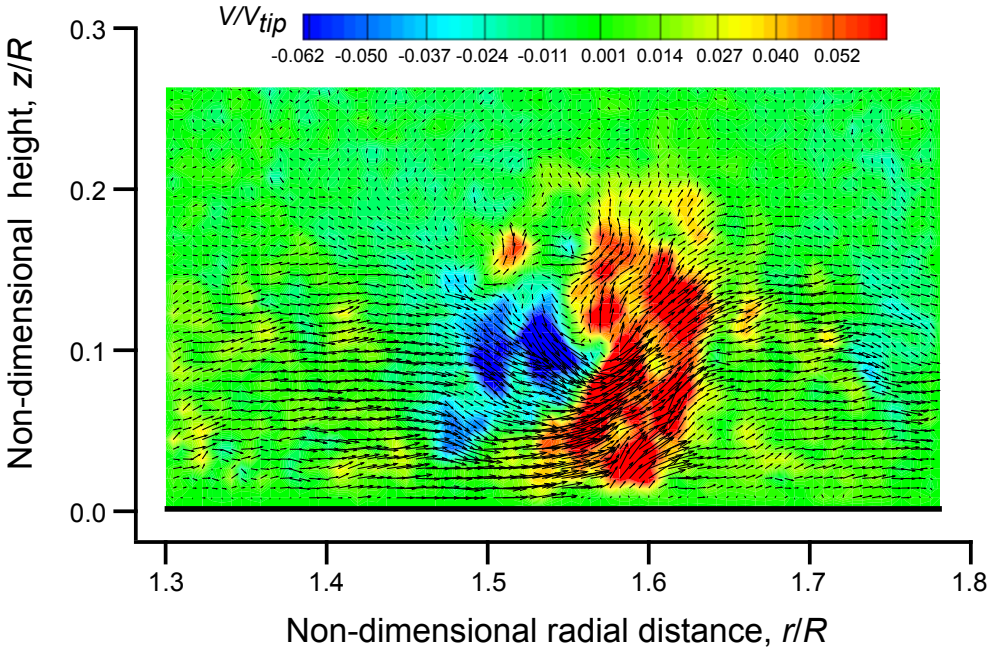

(h) PIV at time step 4, $\psi_b \approx 9°$

Figure 3.6: (Concluded) Flow visualization in ROI 1 and PIV in ROI 2 showing the time-history of the vortex merging process.

effect being an artifact of the shearing forces produced during the vortex-vortex interactions as well the adverse pressure gradient at the wall. An adverse pressure gradient in the flow can be deduced from the observed thickening of the boundary layer region immediately below the vortex, or in some cases by incipient flow separation. After the merging of adjacent vortices, the corresponding measured velocity field (discussed next) showed a transient increase in both the upwash and downwash velocities near the locations of the merging process. Vortex merging was found to also introduce much higher velocities above the shear layer that demarcated the wake boundary, increasing the apparent turbulence levels in this region of the flow. This increase in turbulence above the slipstream boundary was found to be important where sediment was uplifted into the flow (discussed later).

As the rotor height was further lowered, the phase-resolved spatial positions of the rotor wake and the vortex filaments tended to become even more aperiodic, also increasing the propensity for vortex-vortex pairing and merging. Pairing differs from merging in that it involves an older tip vortex rolling above a younger tip vortex. However, instead of merging together and mixing, in this case the pair continue to rotate about a common center of circulation as they convect parallel the ground plane. One of the outcomes of this behavior is that the vortices were seen to maintain more distinct cores to longer times (wake ages) as they continued to convect along the ground plane. The frequency at which pairing occurred increased markedly when the rotor was in the z/R = 0.75–1.25 height range above the ground.

Moving the rotor height down to $z/R = 0.5$ caused the rotor wake to expand outward quickly across the ground plane. The results suggested that instabilities formed on the

vortex filaments because of their close proximity to the ground, and caused them to diffuse at relatively younger wake ages. This effect, in turn, caused the older adjacent vortices to merge more frequently when they were at younger wake ages, thereby introducing a significant amount of turbulence further upstream in the flow. This process was further intensified as the rotor was lowered to a height of $z/R = 0.25$; in this case the wake contracted and expanded very quickly, and upon reaching the ground the tip vortices were observed to rapidly diffuse. For both these latter rotor heights, significant diffusion of the tip vortices does not have time to manifest before the vortices interact with the wall flow.

Not only do the dynamics of adjacent blade tip vortices at the ground introduce vorticity and turbulence into the flow, but they also powerfully interact with each other [8]. To investigate this effect further, the flow field of the 1-bladed rotor was studied at the same heights above the ground as for the 2-bladed rotor. Results in this case for a representative height of $1.0R$, are shown in Fig. 3.7. The immediate observation is that the 2-bladed rotor produces twice the number of vortices and wake sheets as compared to the 1-bladed rotor. While this observation may seem obvious, it becomes an important consideration when the near-wall interactions are examined in quantitative detail (see later). As expected, both rotors produce a wake that initially contracted and then radially expanded as it interacted with the ground plane. The vortices in both cases follow the slipstream boundary between the wake and the quiescent flow, occasionally interacting with each other.

The addition of a rotor blade into the problem also means more vorticity from the wake sheets and the spacing between adjacent turns of the trailed vortices is considerably smaller. The resulting flow field, however, is far from a simple superposition of

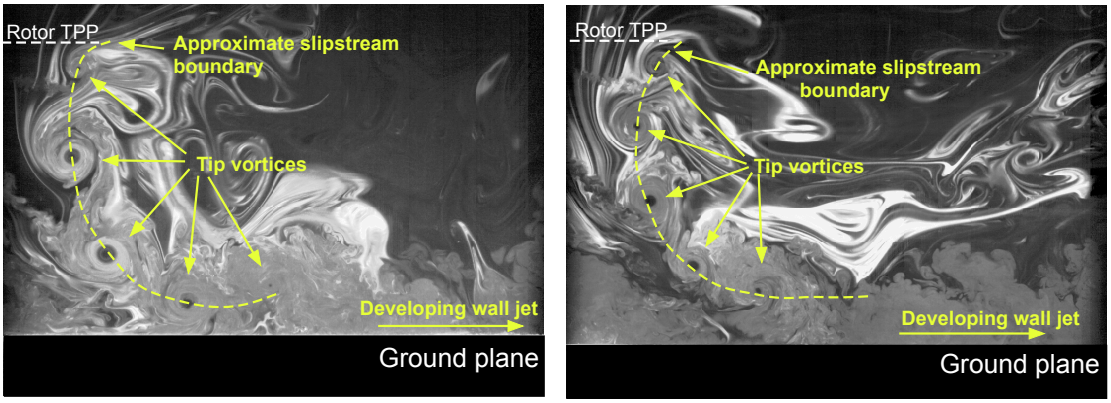

(a) 1-bladed rotor

(b) 2-bladed rotor

Figure 3.7: Single-phase flow visualization comparison of the 1- and 2-bladed rotors at a height of $z/R = 1.0$.

two interdigitated vortex flows. In this case, the lower effective helicoidal pitch of the wake was observed to cause an increased susceptibility to the pairing of adjacent vortex filaments and production of higher levels of aperiodicity in the flow, especially in the near-wall region. The tip vortices for the 1-bladed rotor experienced merging and pairing only occasionally, while the 2-bladed rotor produced more significant interactions between adjacent turns of the vortex filaments. The turbulent nature of the wall-jet, in conjunction with the natural aperiodicity in the flow and closer spacing of the adjacent turns of the vortex filaments, led to a more unsteady far-field and more persistent vortical flow structures, as shown in Fig. 3.7.

The differences in the wakes of both rotors can be further exposed by using the PIV measurements taken in ROI 1 with both rotors at a height of $z/R = 1.0$. Figures 3.8a and Fig. 3.8b compare the vorticity fields for the two tests, and Fig. 3.8c and Fig. 3.8d compare the wall-normal velocity; again red indicates an upwash and blue indicates a downwash,

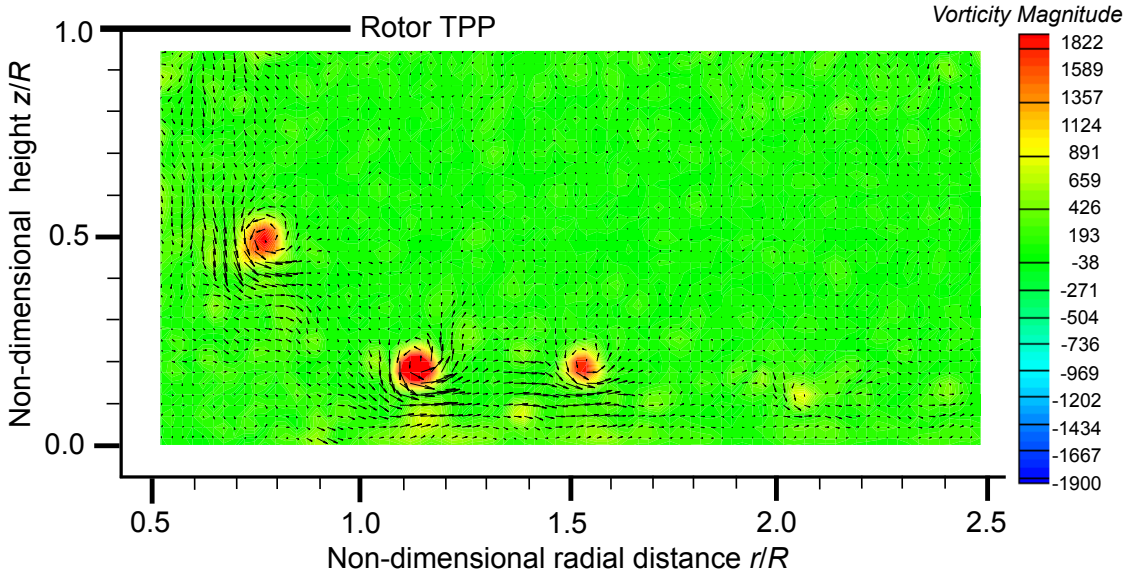

(a) 1-bladed vorticity

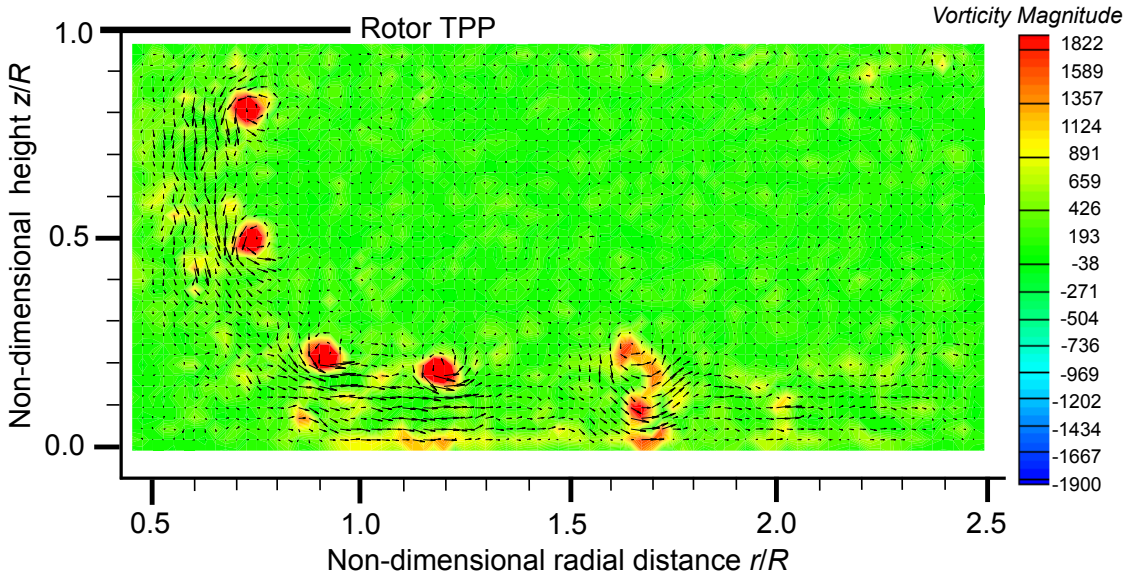

(b) 2-bladed vorticity

Figure 3.8: Vorticity in ROI 1 for the 1- and 2-bladed rotors. $\psi_b = 302.4°$.

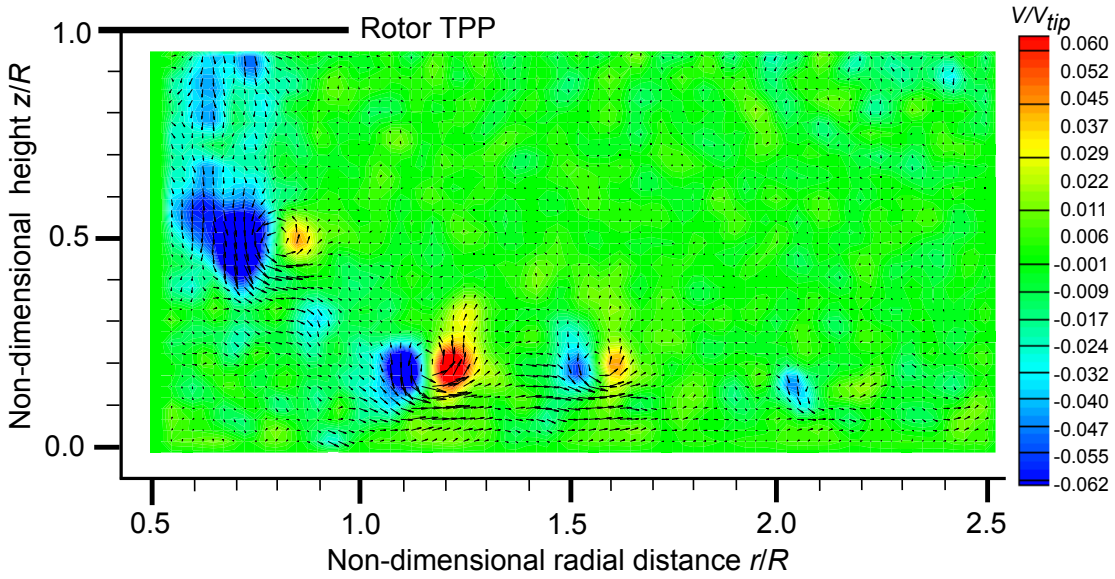

(c) 1-bladed wall-normal velocity

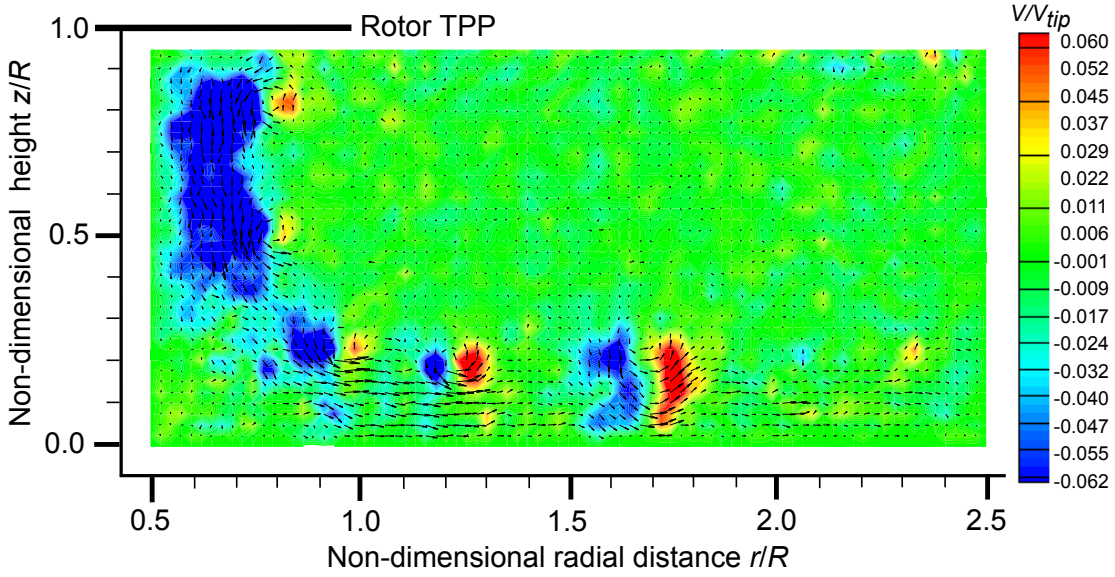

(d) 2-bladed wall-normal velocity

Figure 3.8: (Cont'd) Wall-normal velocity in ROI 1 for the 1- and 2-bladed rotors. ψ_b = 302.4°.

thereby making a red-blue pair the "signature" of a vortex flow. The magnitude of the vorticity contours showed that the relative strength of the vortices generated by each rotor was almost the same (recall from previously that C_T/σ was held constant for all the test conditions).

While the 24 x 24 PIV interrogation window grid used in the present tests was not quite fine enough to resolve all of the small-scale turbulent eddies inside the rotor wake, it did identify areas of increased turbulence that were produced when using the 2-bladed rotor. This effect can be seen by the yellow contours depicting increased levels of vortical flow directly below the rotor and also in the wake at the older wake ages. As with many of the images, in this particular set of images of the 2-bladed rotor, it produces two adjacent helicoidal vorticex filaments that are in the process of pairing and merging. The equivalent vorticity plot (Fig. 3.8b) shows that there are two distinct centers of circulation that correspond to two adjacent vortices that have paired. As can be seen in the velocity contours (Fig. 3.8d), this behavior causes a local transient increase in both the upwash and downwash in the flow from the resulting larger vortical flow region containing the combined vorticity fields of both of the original vortices.

Further reintensification of the vortical flow results in the persistence of the net vorticity to older wake ages in this case when compared to the flow obtained with the 1-bladed rotor. The adjacent, further upstream vortex in both the 1- and 2-bladed rotor cases, have essentially the same vorticity magnitudes. However, in the 1-bladed case the diffusive action in the flow becomes dominant and counteracts the stretching and straining of the vortex filament, resulting in lower swirl velocities. For the 2-bladed rotor, the pairing and merging of the two vortical structures augments the stretching and straining

process, and creates the large wall-normal velocities that were seen in Fig. 3.8d. The implications of this latter behavior on the uplift of sediment particles is discussed later.

The significance of the observed vortex dynamics on the flow field at the ground can be better understood from the measured velocity profiles. Figure 3.9 shows results for the wall-parallel velocity contours and corresponding two-dimensional velocity profile for the 1-bladed rotor in ROI 2. The velocity profile has been extracted at $r/R = 2.0$ (measured downstream from the rotor shaft axis). This sequence of measurements were separated by 194° of blade rotation. Figure 3.9b shows the velocity profile near the ground is similar to a classical wall-jet (see Fig. 3.4) but is about to encounter the influence of a tip vortex. As the vortex passes over the cut location (see Fig. 3.9e), there is a transient excursion that creates a localized region of high wall-parallel flow velocity. This result is indicative of a high swirl velocity induced near the ground by the vortex flow, i.e., the velocity in both the wall-parallel and wall-normal directions undergoes sharp increases in its magnitude under the influence of the vortex.

The foregoing excursions in the flow are increased even further when two adjacent vortices pair and merge; see Fig. 3.10. Both the wall-parallel and wall-normal velocities still show the characteristic excursions from the mean flow, however, the excursions are now larger and produce a number of distinct velocity peaks that arise from the merging process of vortices and the creation of secondary vortical flows. The transient excursions from the mean flow velocity extend into the slipstream boundary of the rotor wake, and so could be expected to affect the motion any sediment lying below this region (described next). Another important observation here is that these perturbations are produced at significant heights above the ground, up to 60–70% of the rotor radius.

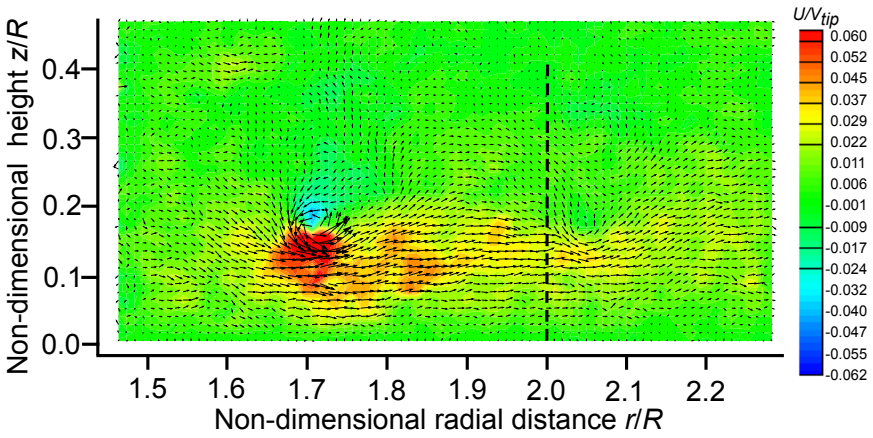

(a) PIV at time $\psi_b \approx 261^\circ$

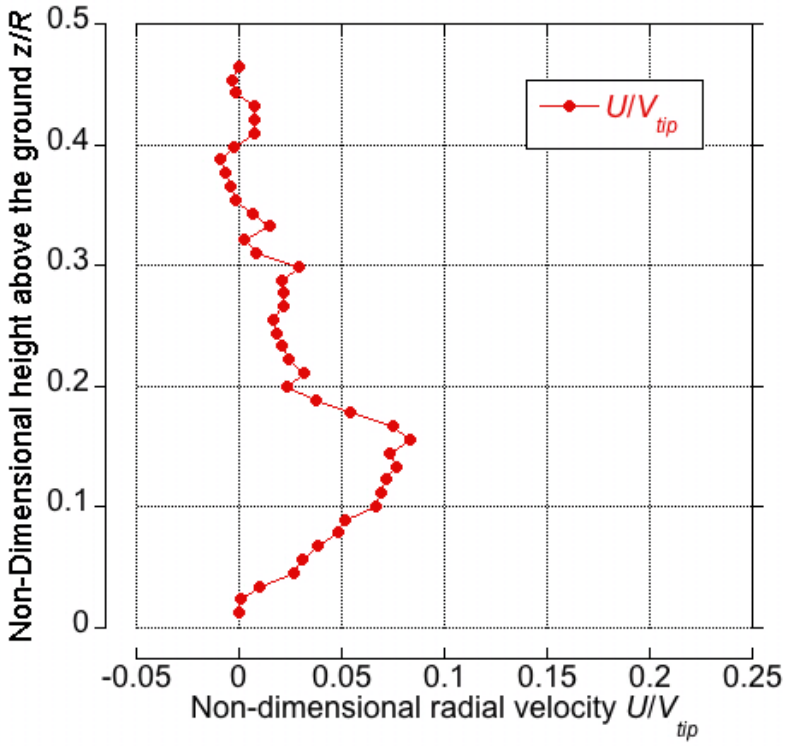

(b) Velocity profile at time $\psi_b \approx 261^\circ$

Figure 3.9: Sequence of images tracking the evolution of the near-wall flow field; contours show wall parallel velocity. Velocity profile is taken at $z/R = 2.0$ (indicated by black dashed line).

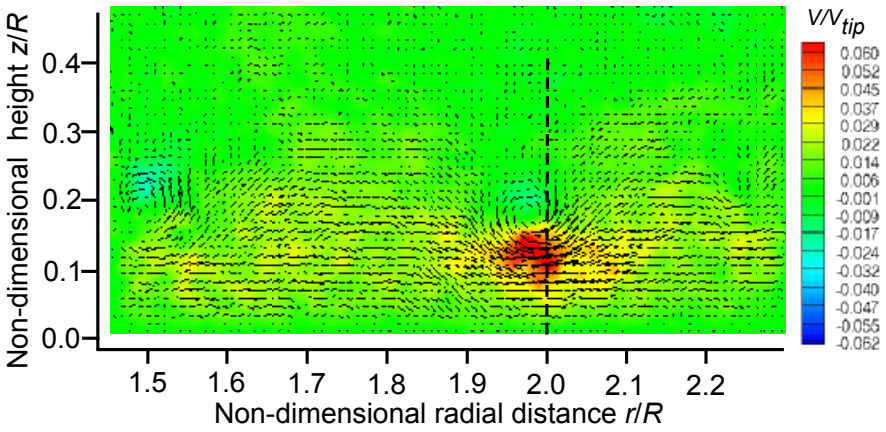

(c) PIV at time $\psi_b \approx 95.4°$

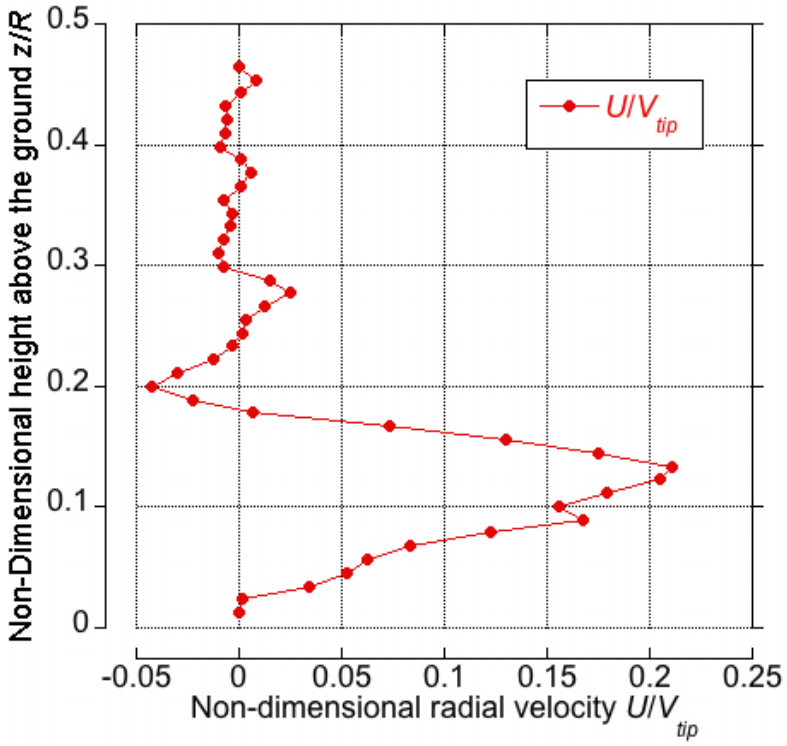

(d) Velocity profile at time $\psi_b \approx 95.4°$

Figure 3.9: (Cont'd)Sequence of images tracking the evolution of the near-wall flow field; contours show wall parallel velocity. Velocity profile is taken at $z/R = 2.0$ (indicated by black dashed line).

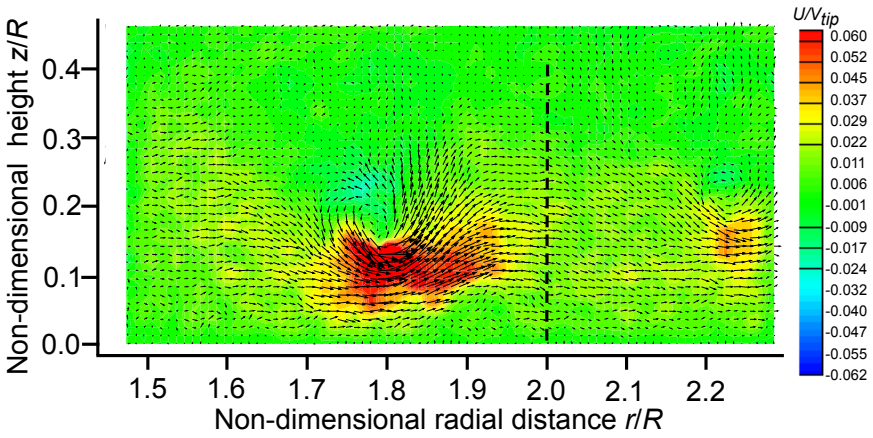

(e) PIV at time $\psi_b \approx 289.8°$

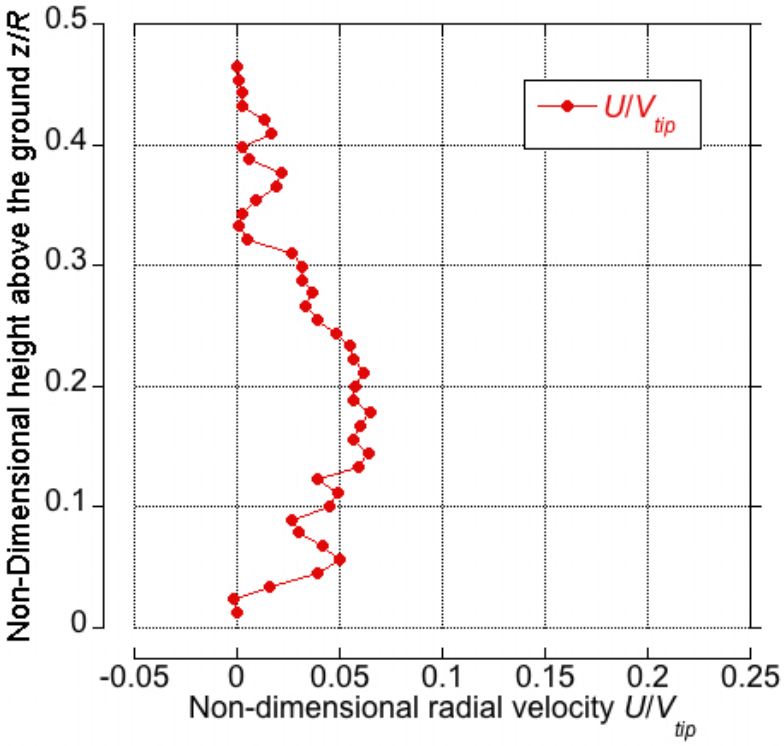

(f) Velocity profile at time $\psi_b \approx 289.8°$

Figure 3.9: (Concluded) Sequence of images tracking the evolution of the near-wall flow field; contours show wall parallel velocity. Velocity profile is taken at $z/R = 2.0$ (indicated by black dashed line).

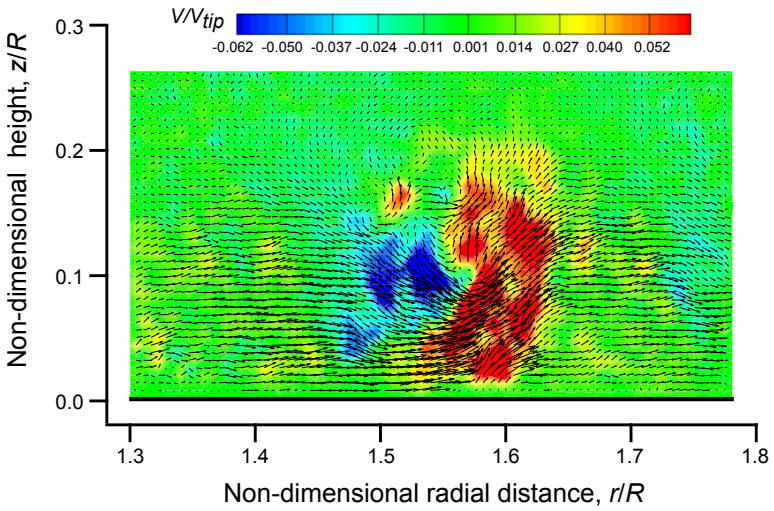

(a) PIV image of two merged vortices

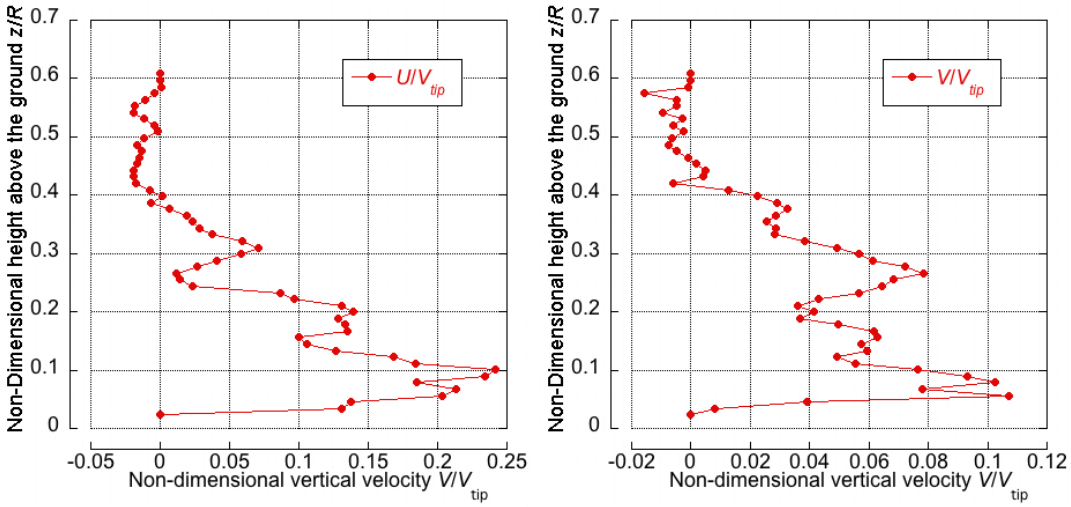

(b) Radial velocity profile

(c) Vertical velocity profile

Figure 3.10: Wall-normal and wall-parallel velocity profiles for two vortices that have merged for a 2-bladed rotor at $z/R = 1.0$.

3.2 Considerations of Scale

The rotor used in the current work obviously has a relatively small diameter when compared to full-scale helicopter rotors (it is roughly 0.0096 scale). This large difference

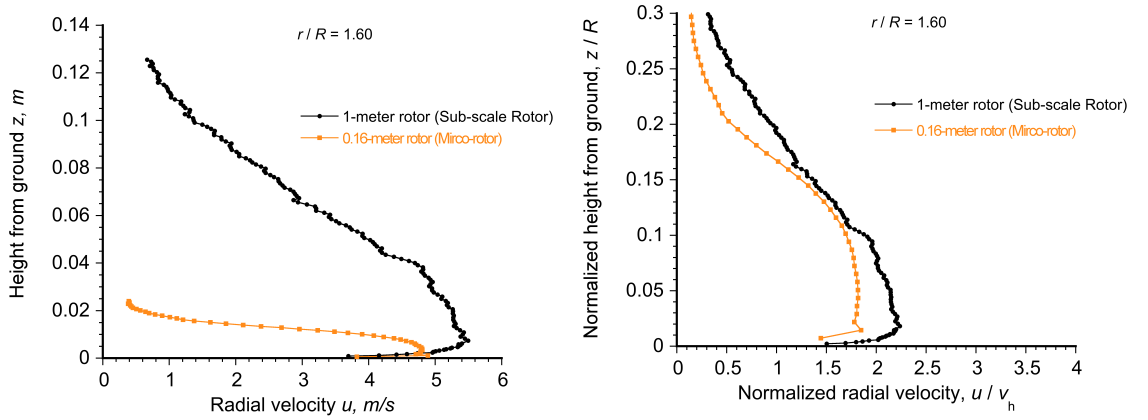

(a) Velocity profile comparison

(b) Non-dimensionalized velocity profile comparison

Figure 3.11: Velocity profile comparison for a 0.16 m diameter rotor and a 1.0 m diameter rotor at a radial location of $r/R = 1.6$

in geometric size brings into consideration possible aerodynamic scaling issues that are associated with laboratory-scale experiments with rotors in general, and in the two-phase flow environment in particular. Figure 3.11a shows a comparison of a wall-parallel velocity profile at the ground taken at $r/R = 1.6$ for the rotor used in current experiments with results from a larger rotor with a diameter of approximately 1 meter operating at a tip Reynolds number of approximately 250,000 [21]. Both velocity profiles were obtained from an ensemble average over a large data set of 1000 flow realizations for the smaller rotor and 100 flow realizations for the larger rotor.

Notice that the peak velocities for both rotors are relatively similar, with the values for the smaller rotor being slightly lower, but the disparity of geometric scales means that the boundary layer thicknesses are very different. However, if the velocity and rotor height above the ground are non-dimensionalized by the hover induced velocity from momentum theory, v_h, and rotor radius, R, respectively, as shown in Fig. 3.11b, it is significant to see

that the two velocity profiles now become very similar. This outcome shows that even though the rotor used in the present experiment is relatively small, the results obtained may be representative of what would be obtained at larger scales. The outcomes here, however, do not necessarily imply that the present results would be fully representative of those obtained at full-scale, i.e., with actual helicopters. While other aspects of the flow properties would also need to be compared (e.g., turbulence spectra), these initial results suggest that flow measurements that are representative of those at a larger scales can be adequately studied in the laboratory at much smaller scale, which becomes a particularly important consideration when the dual-phase flow environment must be measured.

3.3 Dual-Phase Results

Dual-phase FV was first conducted in ROI 1 below the rotor to gain a general understanding of the processes of sediment entrainment and mobilization under the action of the rotor wake. The overall goal was to understand, in good detail, the mechanisms of sediment uplift off the ground and how the sediment was suspended in the flow by the rotor wake, i.e., the eventual development of a dust cloud. For most of the dual-phase FV and PIV conducted in the present work, the sediment bed was composed of particles in the 45–63 μm diameter range, which was found to be the most mobile type of sediment.

3.3.1 Dual-Phase Flow Field

Figure 3.12 shows the two-phase flow in ROI 1 for the 2-bladed rotor operating at a height of $z/R = 1.0$ above the ground. This image shows waves of sediment that

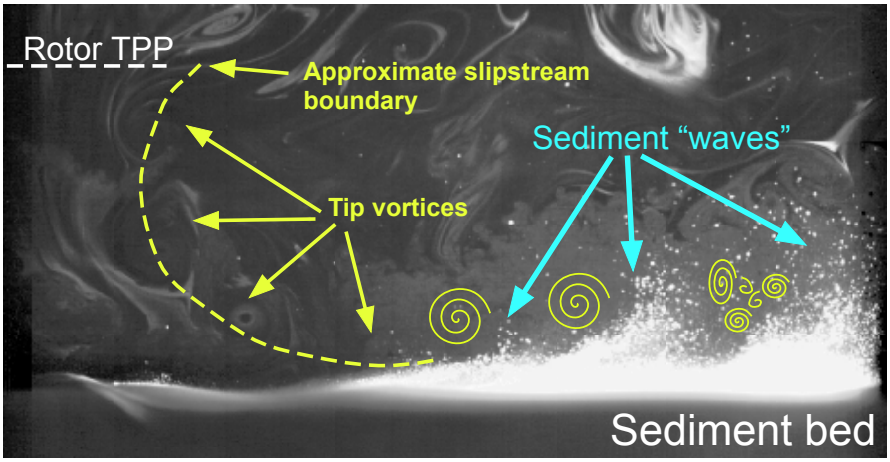

Figure 3.12: Dual-phase flow visualization of the 2-bladed rotor at $z/R = 1.0$ above a sediment bed depicting the characteristic waves of sediment that are induced by the vortex passage over the underlying bed. $\psi_b = 108°$.

are lifted by the rotor wake flow and are convected along the ground just ahead of each passing vortex. This observation confirms previous observations [8] that the vortices play a primary role in the uplift of sediment particles from a bed underlying the rotor. Towards the right-hand-side of the image, the vortex induced swirl velocities here have decreased and the sediment particles in this region of the flow are more heavily influenced by gravity and inertial forces. Further downstream, the flow has become more turbulent and the sediment was noted to follow more random paths under the action of this type of turbulent flow.

3.3.2 One Versus Two Blades and Effect of Rotor Height

As was done using the single-phase FV, the flows generated by the 1- and 2-bladed rotors were examined at various rotor heights above the ground plane when operated at the

same blade loading coefficient, but this time over the mobile sediment bed. Figure 3.13 shows a comparison of the results for both rotor systems at heights of z/R = 1.5, 1.0 and 0.5 above the ground. As the height of the 1-bladed rotor was lowered, it was noted that the amount of sediment that was uplifted did not significantly increase. This outcome is because the vortex filaments do not undergo as much pairing and merging as was observed with the 2-bladed rotor. Therefore, the tip vortices eventually spin down under the action of shearing and turbulence, as was seen in the single-phase results.

The results obtained with the 2-bladed rotor were found to be different in that the interdigitated helicoidal vortex filaments more readily interacted with each other, as previously explained. In this case, the resulting uplift and suspension of the sediment particles in the flow was greatly increased as the rotor height was lowered toward the ground. The single-phase results showed that as the 2-bladed rotor was lowered there was also an increase in aperiodicity in the flow. The dual-phase FV indicated that this increase in aperiodicity (because of the vortex-vortex interactions such as pairing and merging) correlates with significant sediment mobilization and uplift. It was shown in Fig. 3.9 that vortex-vortex interactions produced large excursions from the mean flow velocity, confirming that these transient excursions play a very important role in the mobilization and uplift of sediment. It was clear that the characteristic waves of uplifted sediment seen in the two-phase images were mostly a consequence of the local velocity excursions that were caused by the high swirl velocities induced by the vortices.

It is important to note the change in the topology of the sediment bed that eventually occurs in each test. From Fig. 3.13(f), there is a clear difference in the bed topology created by the 2-bladed rotor versus the 1-bladed rotor case after the approximately the

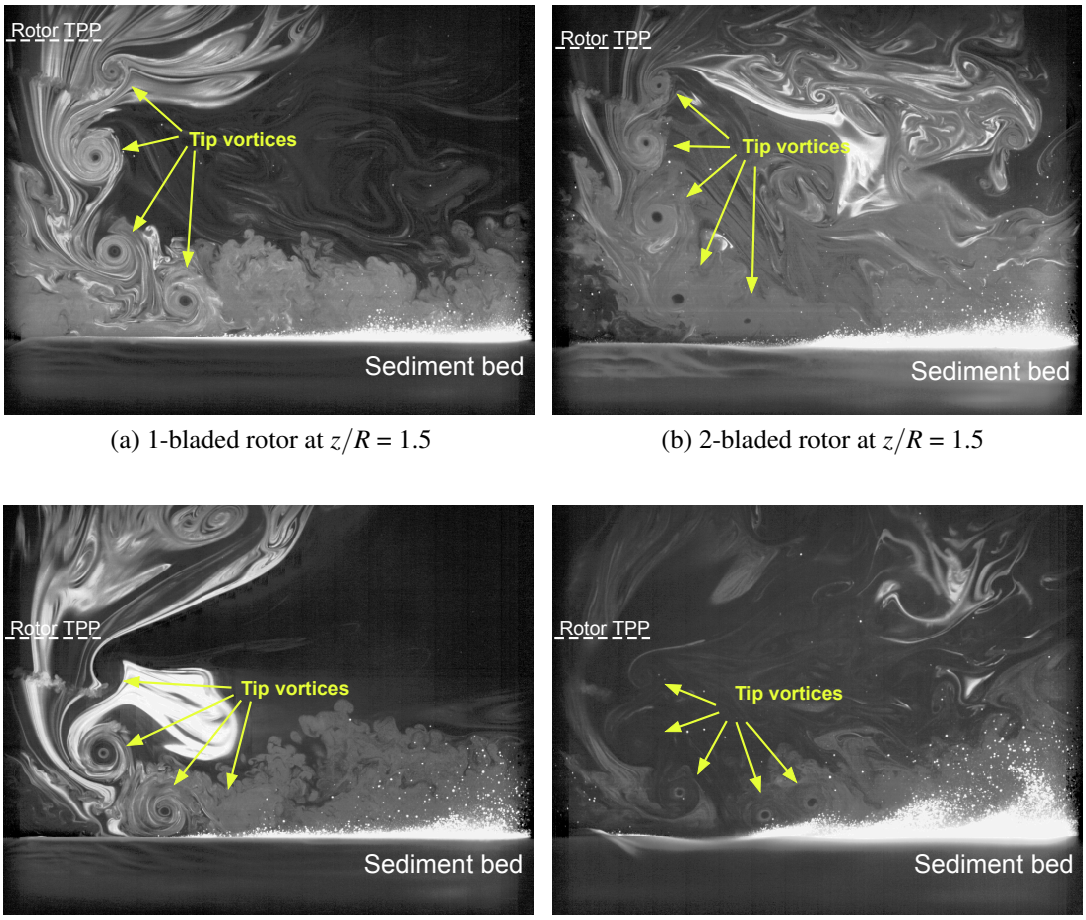

(a) 1-bladed rotor at $z/R = 1.5$

(b) 2-bladed rotor at $z/R = 1.5$

(c) 1-bladed rotor at $z/R = 1.0$

(d) 2-bladed rotor at $z/R = 1.0$

Figure 3.13: Comparison of the flows for 1- and 2-bladed rotor at various heights over a sediment bed comprised of 45–63 μm particles. $\psi_b = 54^\circ$.

same running time. This outcome is because the impingement of the vortices creates a deflation region near where the vortices impinge upon and interact with sediment bed. The sediment particles removed from this region are either uplifted into the flow or deposited further downstream in the form of a dune. The consequence of dune formation is that when it reaches a critical height relative to the rotor dimensions it begins to alter the wall flow such that, in some cases, it can precipitate the onset of vortex-vortex interactions. This effect ultimately leads to higher flow fluctuation velocities than would have other-

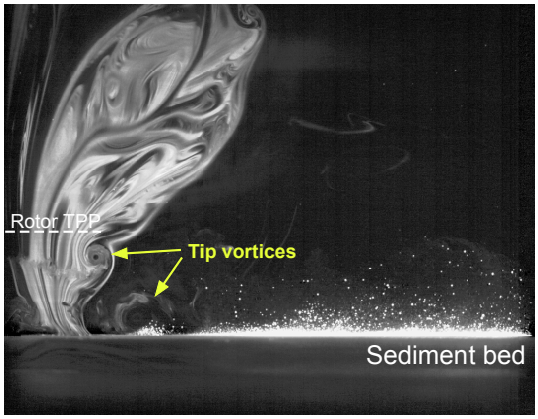

(e) 1-bladed rotor at $z/R = 0.5$

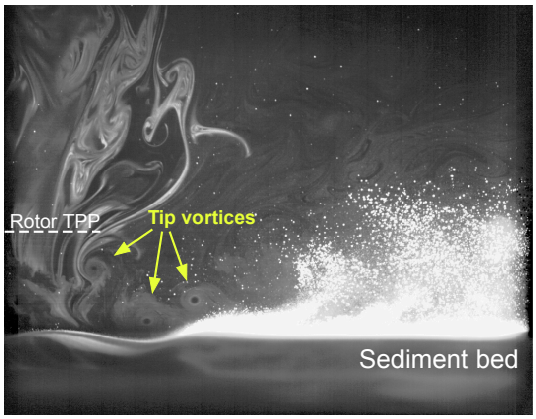

(f) 2-bladed rotor at $z/R = 0.5$

Figure 3.13: (Cont'd) Comparison of the flows for 1- and 2-bladed rotor at various heights over a sediment bed comprised of 45–63 μm particles. $\psi_b = 54°$.

wise occurred with a completely flat sediment bed. Measurements of the developing bed morphology under similar vortical flow conditions has been done by Dade et al. [35], but in the present case further measurements will be required to quantify this effect in detail.

3.3.3 Sediment Uplift and Mobilization Mechanisms

To gain a more complete understanding of the dust field that was created under the influence of the rotor wake, it was necessary to examine in close detail the areas of the bed where sediment was actually being entrained into the flow. From the dual-phase FV made in ROI 1, it can be concluded that the dual-phase flow environment at the ground is intricately complicated. To this end, ROI 2 was chosen to encapsulate the region that was responsible for mobilizing and entraining a majority of the sediment. The goal for these experiments was to identify and quantify the fundamental uplift mechanisms that occurred at the bed, and to understand how these mechanisms related to the overall

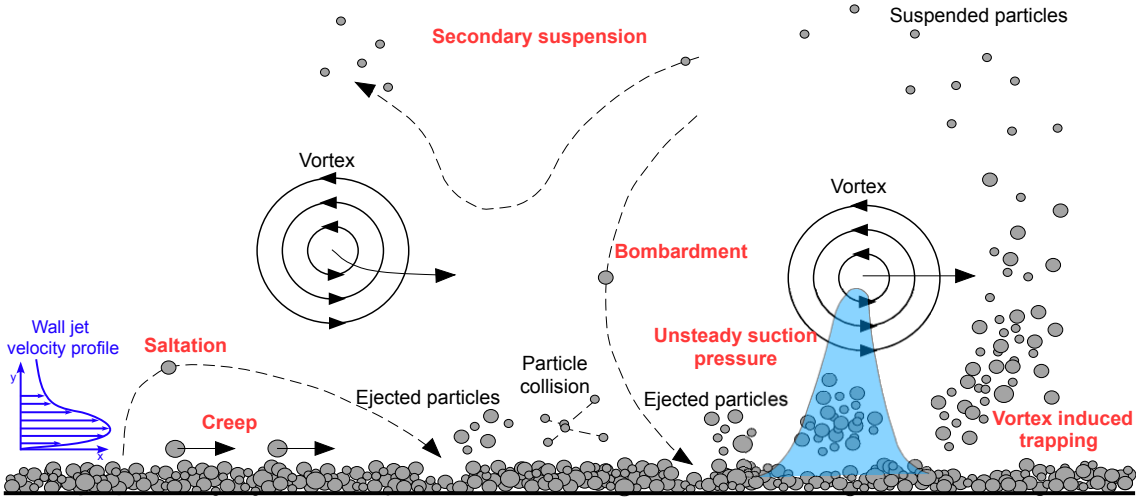

Figure 3.14: Schematic showing the different modes of sediment particle motion and the fundamental uplift mechanisms as observed in the near-wall region.

transport of sediment up into suspension around the rotor.

A schematic of the observed near-wall two-phase flow mechanisms is shown in Fig. 3.14. Identified in red are the sediment transport mechanisms that were observed to contribute most significantly to sediment mobilization, including particle uplift and suspension. These mechanisms are: creep, modified saltation, bombardment, unsteady pressure effects, vortex-induced trapping, and secondary suspension. These mechanisms can be further subdivided into two categories: classical sedimentology (i.e., aeolian) mechanisms and rotor-specific mechanisms, with both mechanisms being associated with primary and secondary ejection of sediment particles as well as entrainment.

3.3.3.1 Creep and Saltation

The first two mechanisms (creep and saltation) have been studied in great detail in the field aeolian sciences [31–33]. Below the rotor, these mechanisms appear in the

near-wall region, but in significantly modified forms. Creep is a process by which loose sediment particles on the ground (usually the larger particles) roll along the surface of the bed, subsequently disturbing other particles along their paths. These creeping sediment particles move under the shearing action produced by the turbulent flow at the wall, which produces forces that are sufficient to mobilize the particles but does not generally have sufficiently high wall-normal velocities to uplift or entrain the particles into the flow.

Saltation occurs when loose sediment particles on the ground obtain a vertical velocity through a surface collision or a wall-normal excursion in the flow velocity (e.g., from the action of turbulence). These particles initially jump from the sediment bed and then follow ballistic-like trajectories back toward the ground. The saltating particles extract energy from the surrounding flow such that they gain velocity and impact the sediment bed with considerably more momentum and energy, causing the ejection of many new particles. A schematic of the dynamics of this particular mechanism is shown in Fig. 3.15(a).

The process of saltation, however, occurs in a significantly modified form below the rotor because the airborne particles are also influenced by the impinging vortices and highly vortical flow produced by the rotor wake. These factors can either slow or accelerate the velocity of the saltating particles, changing their trajectories compared to what would be obtained in a more uniform flow. Therefore, there are actually many different saltation trajectories that the particles can undergo after being uplifted from the bed, not just simple ballistic trajectories.

Figure 3.15(b) shows PTV results for the 90–120 μm glass microspheres in the wake of the 1-bladed rotor in a magnified region of ROI 2. This figure shows 20 overlaid

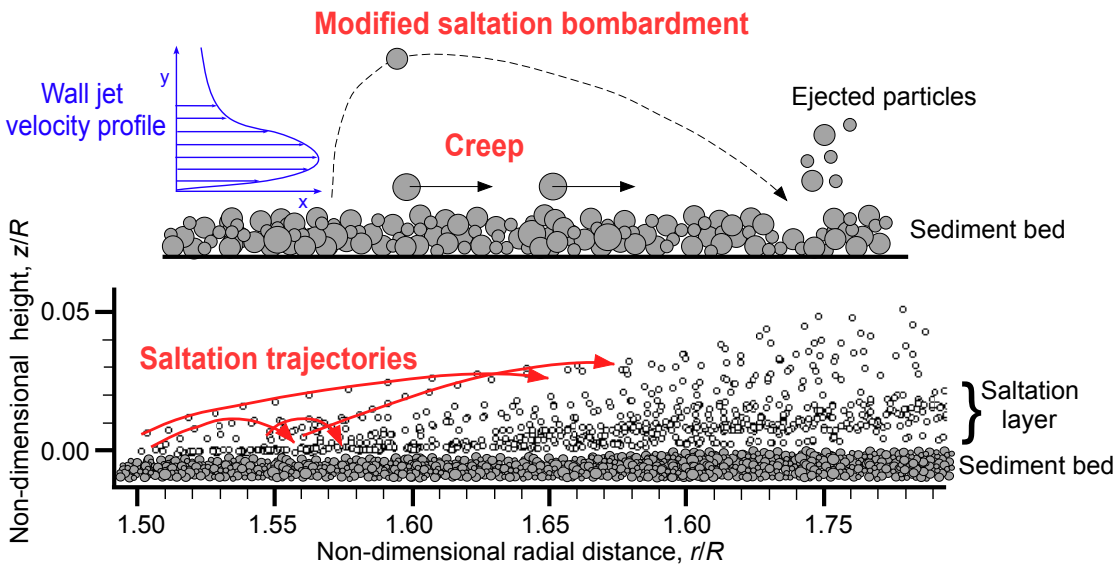

Figure 3.15: Top: Schematic showing modified saltation bombardment and creep. Bottom: PTV data of 20 overlaid images showing some saltation trajectories.

PTV images, with each white circle representing an individual particle that was identified by the particle tracking algorithm, which allows for the tracking of particles from image frame-to-image frame. The red arrows depict different saltation trajectories that occur after the sediment particles are uplifted. Even from only 20 images, it was clear that the sediment particles can follow short or long paths as they convect in the flow and impact the downstream regions of the bed. While not all such particles paths are parabolic, they mostly conform to this profile.

The observations in the present work also showed that modified saltation bombardment is a cascading process that manifests by a significant increase in the airborne particle density at increasingly downstream distances, as well as a gradual thickening of the saltation layer (discussed next). The newly ejected particles that are uplifted from the process of saltation bombardment immediately begin to creep or saltate if they are not directly en-

trained into the flow, causing even more particles to be ejected from the bed. This process eventually forms the so-called saltation layer.

3.3.3.2 Saltation Layer

Figure 3.16 shows a schematic of a saltation layer responding under the influence of two impinging vortices, along with a corresponding measured PIV/PTV image. The image contours represent the wall-normal velocity, while the white circles with red vectors indicate sediment particles with their corresponding velocities. The vortices were observed to create a local thickening of the saltation layer as the particles in this layer convected along the sediment bed. The particles are generally moving in the same direction as the flow but are heavily influenced by inertial forces, causing them to deviate from the mean flow in both velocity magnitude and direction.

Within the saltation layer it was noted that there is a relatively high particle density, which can lead to inter-particle collisions. Figure 3.17 shows one example of two particles in the 45–63 μm diameter range that collide under the influence of a vortex flow. The two particles are initially lifted off the ground into saltation, but because they have different velocities and are also of different sizes, they follow different trajectories. In this case, these trajectories intersect at the collision point—see Fig. 3.17(b)—where the software in this case has actually identified the two particles as one large particle because their intensity signatures overlap. At this point, the particles rebound off each other and undergo a momentum transfer, moving away from each other with altered trajectories.

The foregoing example is just one of simplest of the many possible collisions that

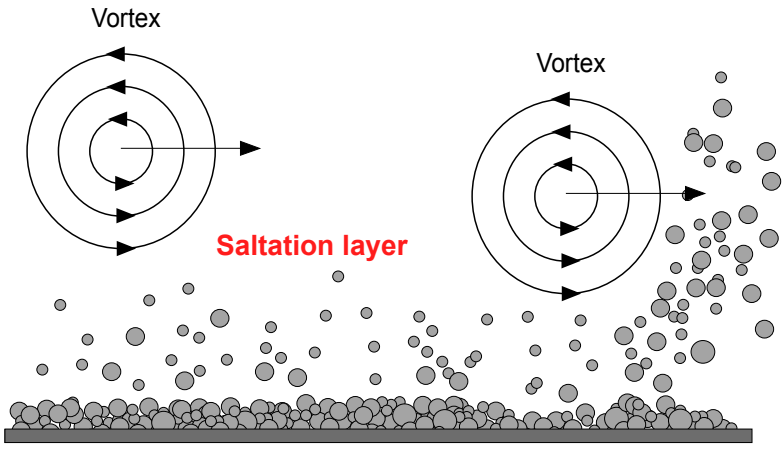

(a) Schematic of saltation layer

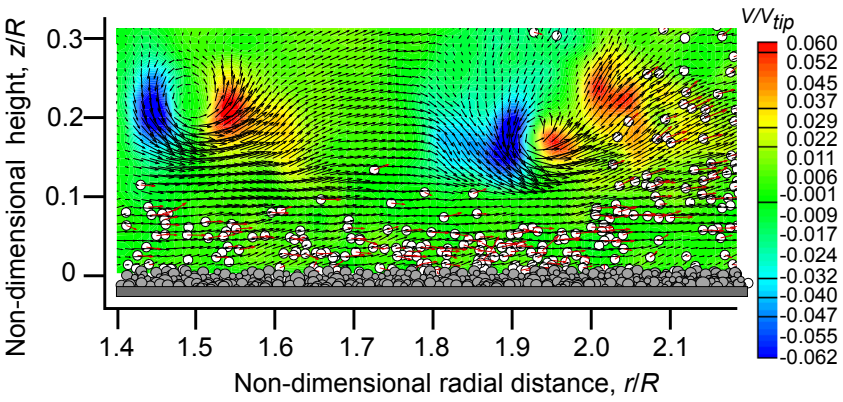

(b) Measurements of saltation layer

Figure 3.16: Schematic and PIV/PTV of a saltation layer under impinging vortex flows.

were observed in the saltation layer near the ground. Recall that the flow field here is very unsteady and highly three-dimensional, so particles collide both in and out of the measurement plane in all three spatial dimensions. Furthermore, groups of particles that are traveling close to each other (or they may convect as aggregates because of residual cohesive forces) were found to be burst apart by a more complex collision with a particle that intersects its saltation trajectory. These observations obviously raise some interesting issues in regard to the detailed modeling of the sediment dynamics in the near-wall region.

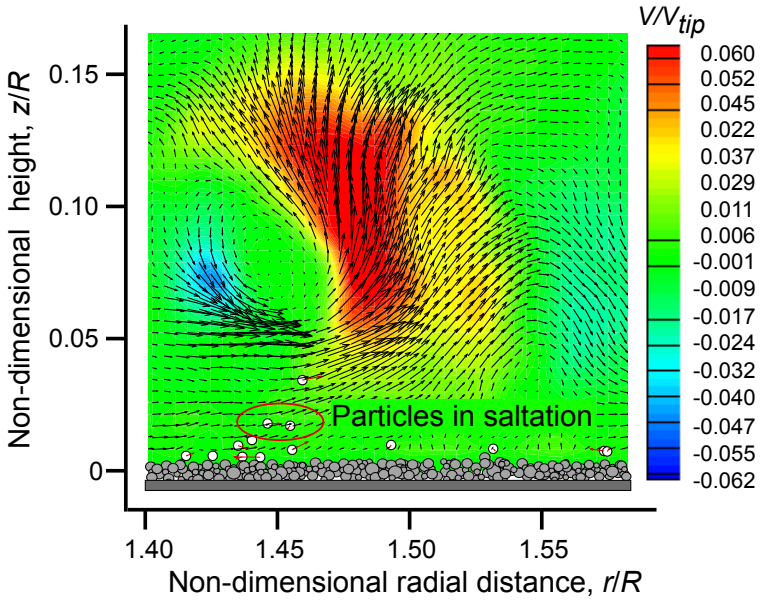

(a) Time step 1, $\psi_b \approx 116°$

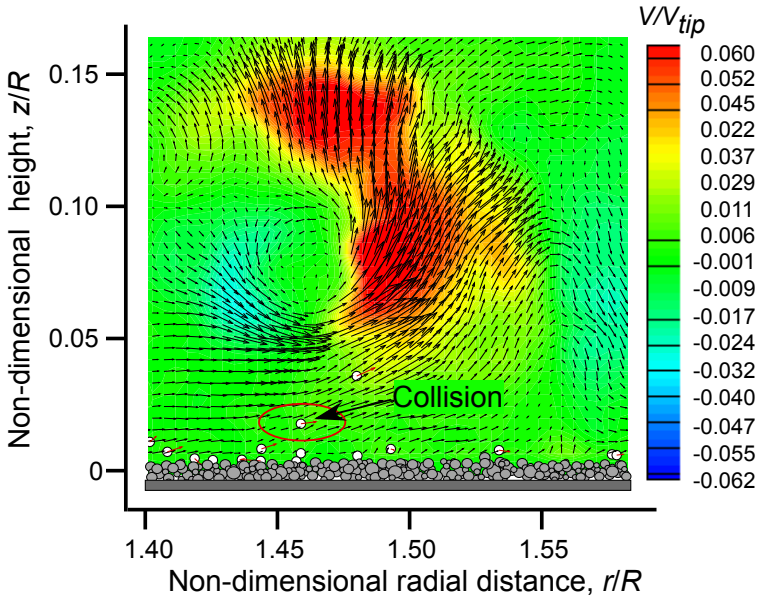

(b) Time step 2, $\psi_b \approx 134°$

Figure 3.17: PTV depicting the collision of two sediment particles with intersecting saltation trajectories: (a) particles saltating; (b) particles colliding

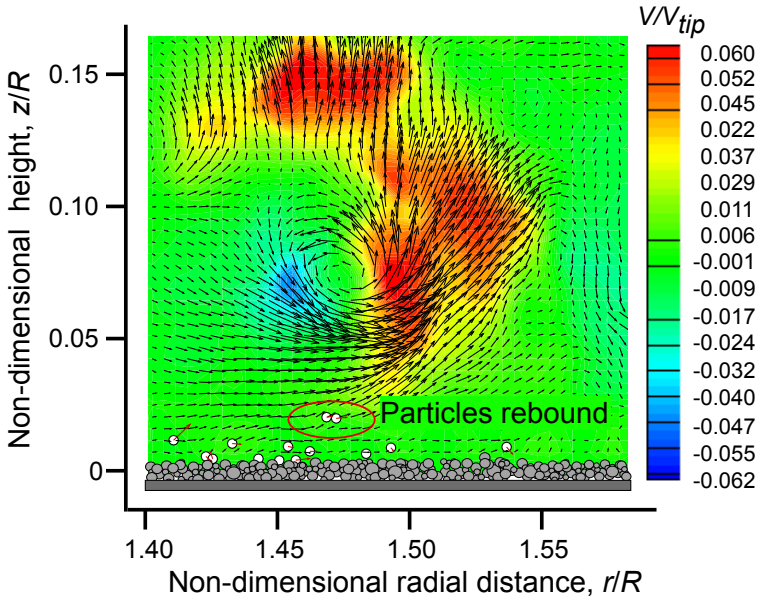

(c) Time step 3, $\psi_b \approx 152^\circ$

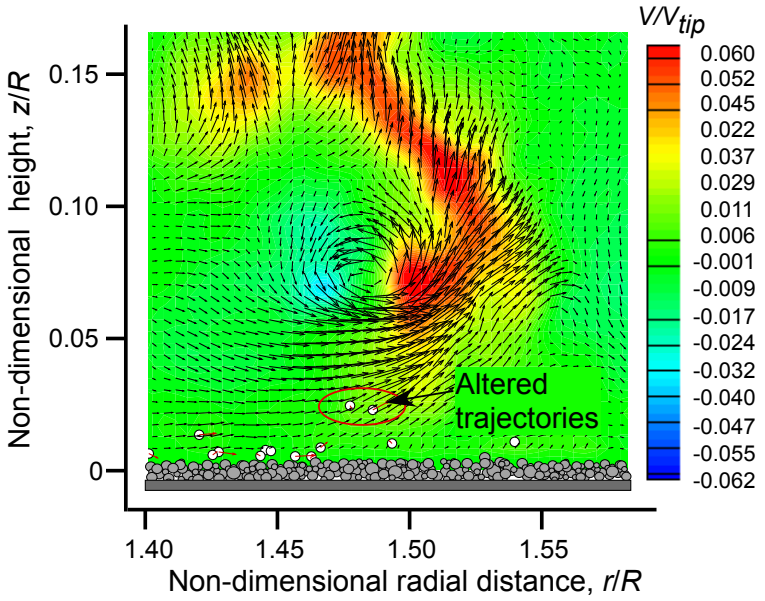

(d) Time step 4, $\psi_b \approx 170^\circ$

Figure 3.17: PTV depicting the collision of two sediment particles with intersecting saltation trajectories: (c) particles rebounding; (d) particles with altered trajectories.

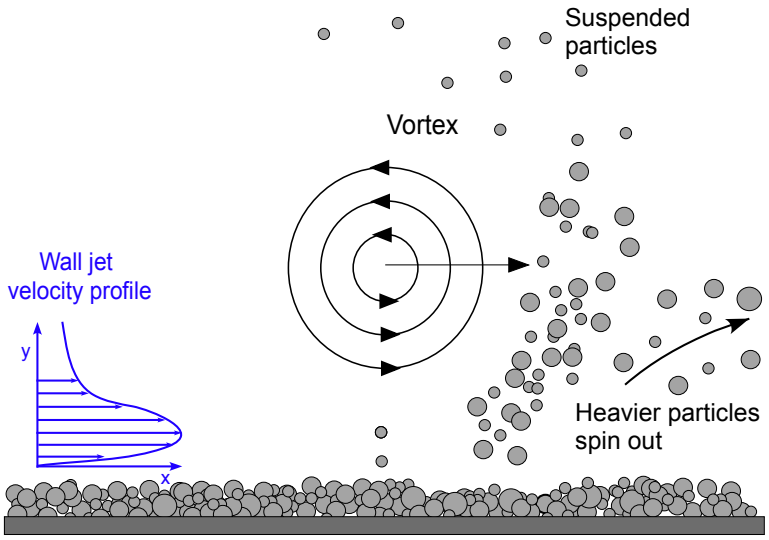

(a) Schematic of mechanism

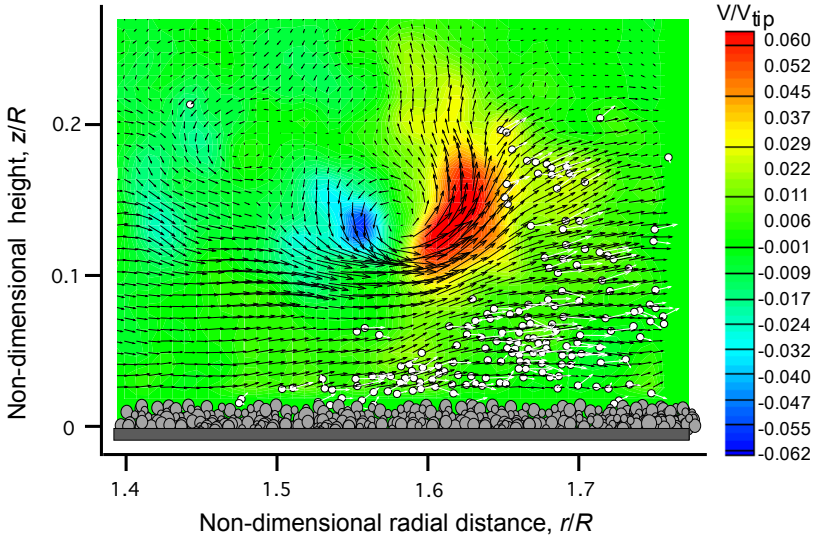

(b) PIV/PTV results of mechanism

Figure 3.18: Schematic and PIV/PTV measurements of showing particles in the saltation layer being entrained into the vortex-induced upwash.

3.3.3.3 Vortex-Induced Trapping

The FV made in ROI 1 revealed that characteristic bursts or waves of sediment (see previously in Fig. 3.12) were convected over the ground just downstream of the

passing blade tip vortices, which appeared to be responsible for uplifting a majority of the sediment into suspension. Besides the effects of pressure forces, for particles to move in the near-wall normal direction above the saltation layer they must entrained by an upwash region in the flow field, such as the upwash induced by an impinging vortex on the bed; see Fig. 3.18. As the upwash region of a vortex passes within proximity to the bed, particles suspended within the saltation layer in this region are immediately uplifted. If the vortex is strong enough and the sediment on the bed is mobile enough, then these particles can be directly entrained from the surface into the upwash region, i.e., through the mechanism of vortex induced sediment trapping.

Subsequently, the heavier particles that have been entrained by the vortex flow are spun out under the action of centrifugal forces unless they are captured by another flow structure (i.e., secondary trapping), in which case they follow ballistic trajectories back toward the bed. For the smaller particles, the momentum they extract from the flow is sufficient to convect them well above the flow at the bed and into overall suspension in the particle field. Particle suspension will occur when the balance of forces on the particle from the vertical flow and turbulent fluctuations in the surrounding flow is greater than the gravitational forces on the particle.

3.3.3.4 Secondary Suspension

Once particles have been suspended clear of the bed, one of three possibilities occurs. The first, as previously alluded to, is that the particles can remain in suspension if the local turbulent flow fluctuations are sufficiently large, i.e., the vertical perturbations

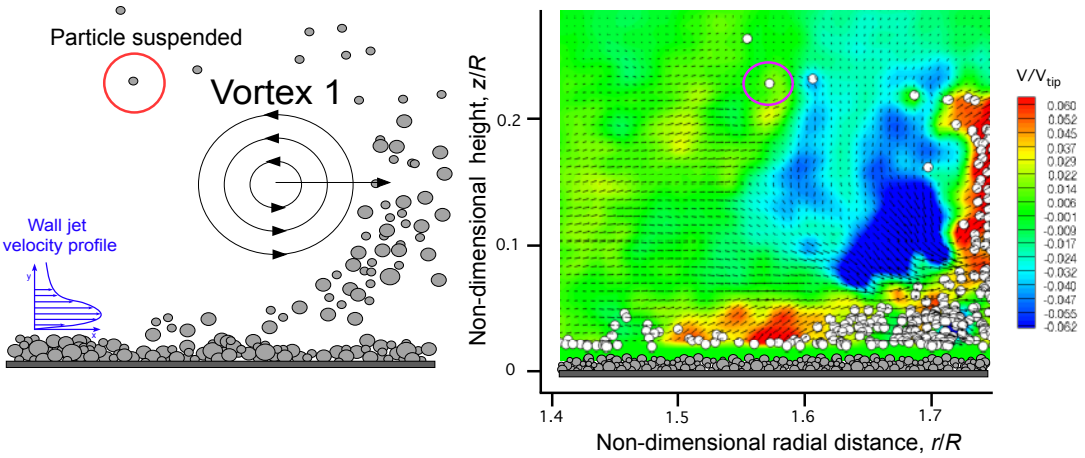

(a) Sediment settling

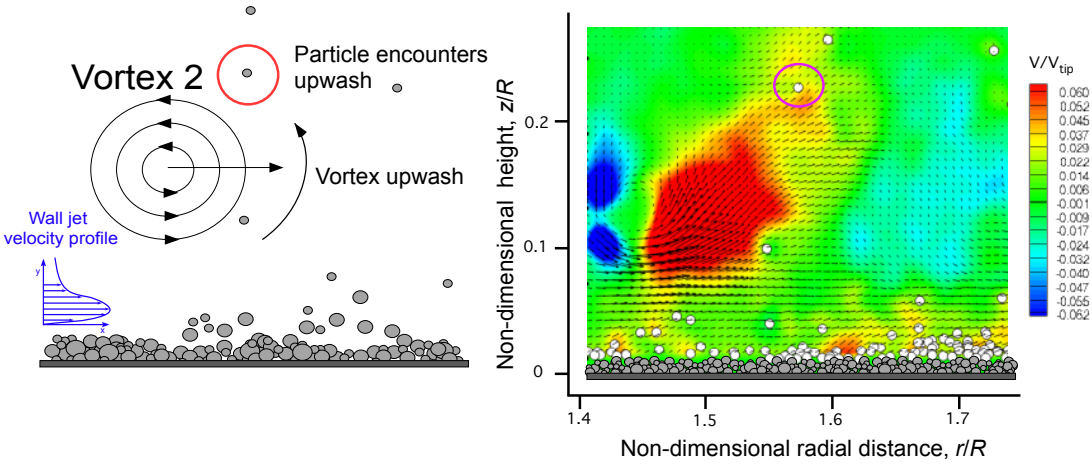

(b) Sediment reentrained

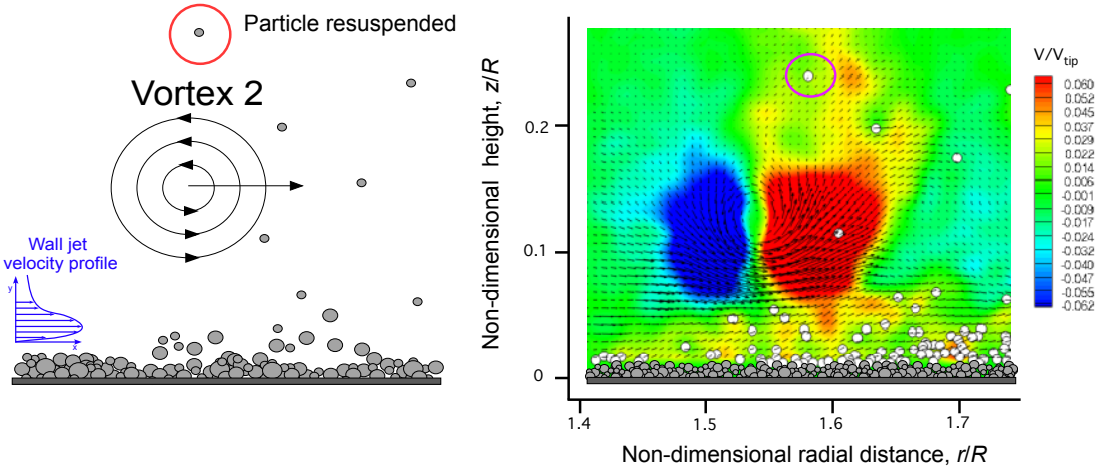

(c) Sediment resuspended

Figure 3.19: Schematic and PIV/PTV measurements of the secondary suspension process.

in the flow are greater than the settling velocities. However, if the conditions for suspension are not met, the particles will slowly settle back towards the bed under gravity. Figure 3.19 shows that such suspended particles can encounter the upwash region of a younger vortex that is convecting along the ground, and almost parallel to the bed. If this event happens, then the particle is uplifted back into suspension again. This process can continue indefinitely, meaning that the suspended sediment can by resuspended as long as upwash regions remain present in the flow field. As more and more of the particles are suspended, the probability of these particles encountering these upwash regions in the flow becomes much more likely. This process reveals itself in the suspended sediment field as swirling particle flows and a rapid overall accumulation of suspended particles, and in some cases bursts of accumulated sediment.

The process of secondary suspension suggests that the generation frequency of vortices plays a strong role in sediment suspension and, therefore, in the development of brownout cloud. Recall that for the flow visualization in ROI 1, more particles were seen to be in suspension for the 2-bladed rotor than for the 1-bladed rotor; see Fig. 3.13. This outcome arises because as particles settle back towards the surface they have a higher probability of encountering the upwash region of one of the vortices as a result of the higher vortex generation frequency for the 2-bladed rotor. These upwash regions are, at times, significantly larger than those produced by the 1-bladed rotor because the 2-bladed rotor flow field is more susceptible to vortex pairing and merging, and higher levels of aperiodicity in the flow. The transient excursions from the mean flow velocities were previously shown to be much larger for a pair of merged vortices, with the consequence that they have a greater influence on the mobilization and uplift of sediment.

3.3.3.5 Bombardment of Sediment

Downwash regions present in the flow can also be responsible for mobilizing particles by means of bombardment of the suspended particles back onto the bed. Such effects can be produced by the downwash of the rotor itself (i.e., a global region of downwash below the rotor) or by the downwash of the passing vortices (i.e., a local downwash).

In practice, the process of reingestion bombardment may occur in any downwash flow region. Shown in Fig. 3.20 is a local form of bombardment that ejects copious amounts of sediment into the developing saltation layer. The particle depicted in this figure orbits around the vortex and impacts the bed and, as with the other forms of bombardment, is responsible for ejecting many new particles from the bed up into the saltation layer.

Particles that are suspended high enough off the bed can be reingested by the rotor flow and then convected downward to produce bombardment on the bed, a process that has previously been called reingestion bombardment [8]. This process is somewhat similar to saltation bombardment, but the generally higher momentum of the particles in this case ejects many more new particles into suspension than would otherwise have occurred in more wall-parallel flow. In fact, field observations [4] of the brownout problem suggest that helicopters that experience reingestion of suspended dust through the rotor system tend to have the worst over types of brownout signatures.

During this global bombardment, the point that a given particle impacts the bed is not necessarily limited to the region in which sediment entrainment has been previously observed. Reingestion bombardment can also occur much closer to the region directly

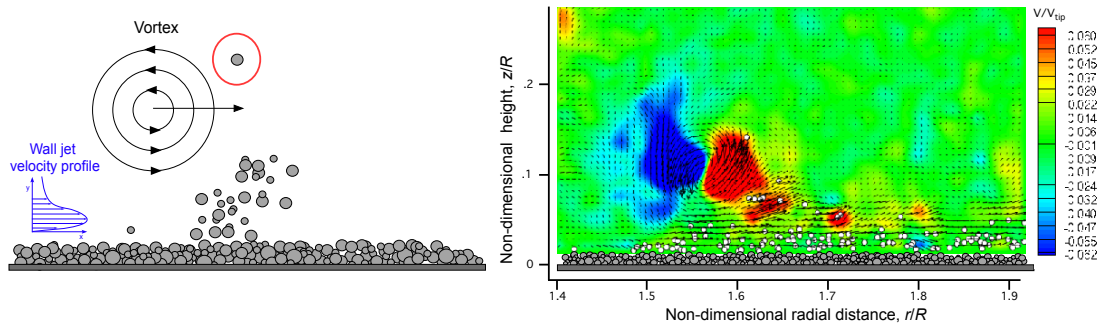

(a) Sediment entrained into vortex upwash

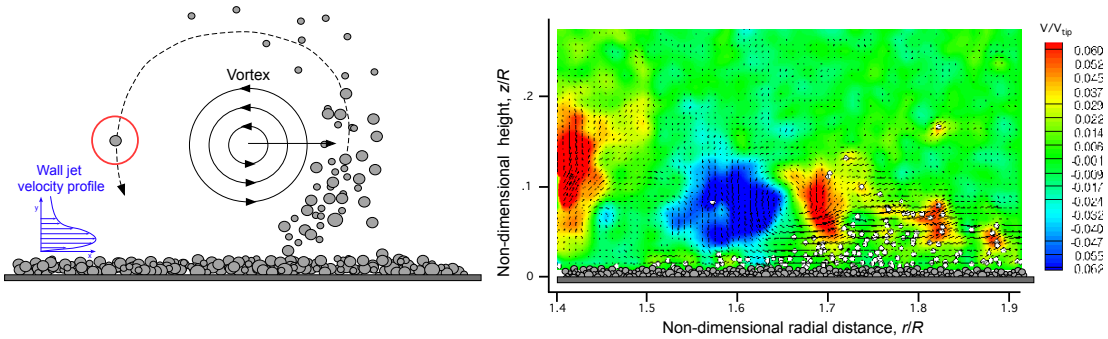

(b) Entrainment into downwash flow

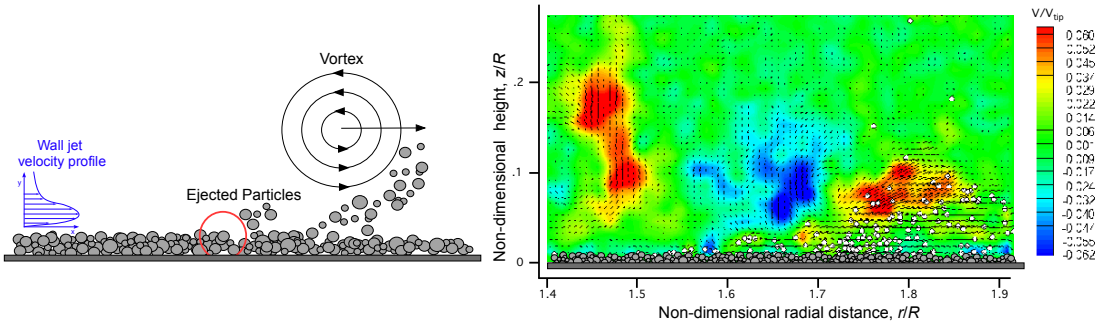

(c) Sediment bombarding bed

Figure 3.20: Sequential schematic and PIV/PTV measurements of a sediment particle undergoing the process of reingestion and ejecting new particles after bombardment onto the sediment bed.

below the rotor, ejecting particles in a region that would have otherwise gone uninfluenced by the effects of the mean flow or by the blade tip vortices.

3.3.3.6 Pressure Effects

A previously unexamined mechanism in the brownout problem is the effect induced by the pressure field created near a vortex flow [32, 47]. While it is not possible to directly measure local unsteady pressure from the PIV, there were certain characteristics of the sediment motion in near-wall region that suggested that pressure forces were playing some role in particle uplift and entrainment into the flow. Greeley et al. [47] have investigated the effects of tornadoes on sediment mobility and have concluded that pressure effects caused by vortices participate in the problem and will affect the threshold conditions for mobility compared to that obtained without the pressure effects.

For example, Fig. 3.21 shows a schematic and FV image that shows a concentration of particles that are directly beneath the centerline of a passing vortex. These particles have not been entrained into any upwash region, yet they are still moving almost vertically upward in the flow away from the wall. While this particular mechanism remains a hypothesis at this point, the observation suggests that the onset of particle motion in this case may be more influenced by the pressure field caused by the unsteady convection of the vortices near the ground rather than by shear forces. Future experiments could be undertaken to measure the induced pressure on the ground plane with the goal of more completely understanding these effects.

3.3.4 Summary of Identified Mechanisms

All of the foregoing mechanisms will play some lesser or greater role when it comes to producing the dust fields surrounding a rotor in ground effect operation above a mobile

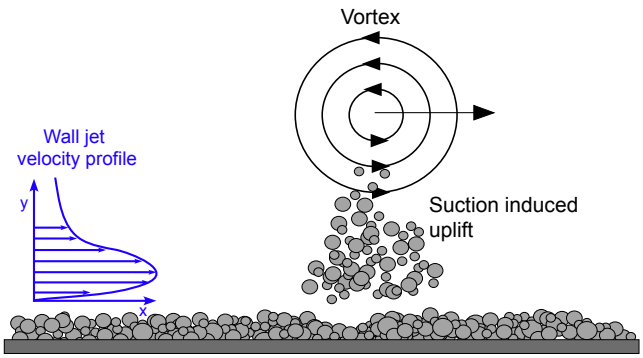

(a) Schematic

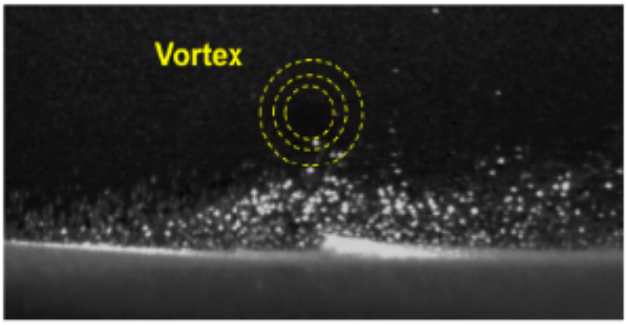

(b) Flow visualization

Figure 3.21: Results showing the influence on the sediment motion by the induced pressure field of a convecting vortex: (a) schematic of the behavior; (b) flow visualization image.

sediment bed. In the present research, the different modes of sediment transport have been better delineated. The near-wall measurements documented at least five fundamental uplift and sediment transport mechanisms below the rotor: 1. Creep, 2. Modified saltation and saltation bombardment, 3. vortex-induced trapping, 4. Reingestion bombardment (local and global), and 5. Secondary suspension with a possible sixth mechanism relating to the unsteady pressure forces created by a convecting vortex. These mechanisms

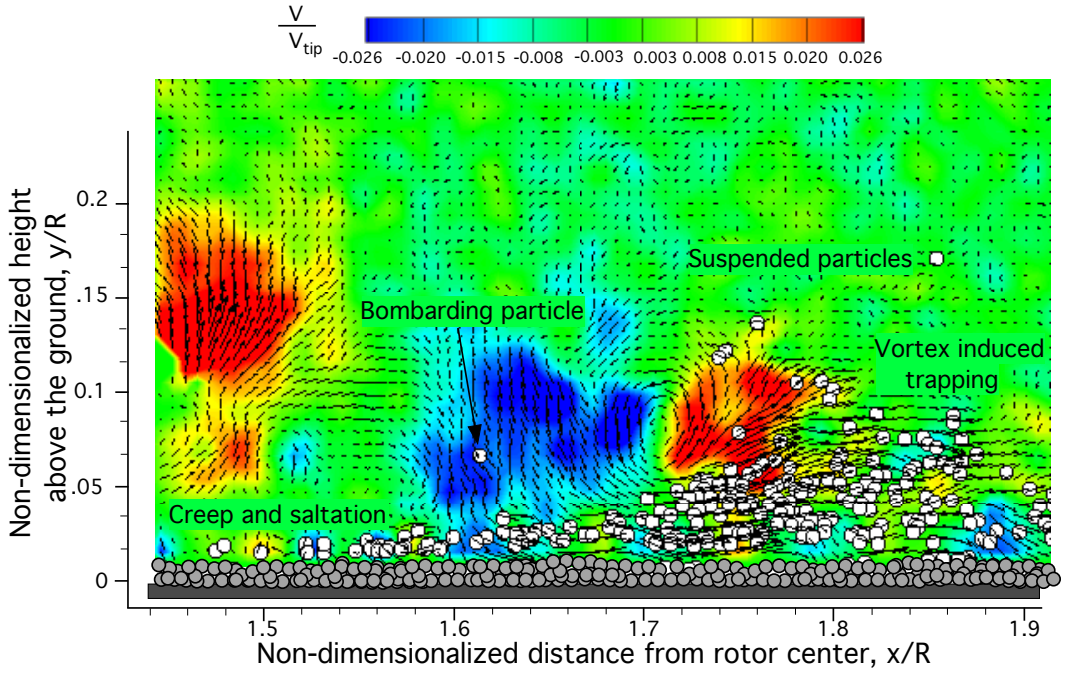

!t

Figure 3.22: A single PIV/PTV image containing several simultaneously occurring sediment uplift and mobilization mechanisms.

were described individually, however, in practice they will occur simultaneously, creating a very complex two-phase flow environment near the ground. For example, Fig. 3.22 shows a PIV/PTV image that depicts a number of the previously described mechanisms in simultaneous process. The uplift mechanisms all interact with one another to a lesser or greater degree, causing a cascading effect that ultimately results in the development of a relatively thick saltation layer and, consequently, the mobilization and uplift of large amounts of sediment into suspension.

3.3.5 Initial Investigation of the Effect of Sediment Size

Another aspect of the problem that was examined in this study, at least initially, was the effect of sediment size. Three different particle diameters in the range of 1–38 μm, 45–63 μm, and 90–120 μm were tested under the influence of the 1-bladed rotor. The rotor was operated under the same conditions for each size of sediment, as previously described, so that the observed effects could be directly compared.

An overall comparison of the results is shown in Fig. 3.23. The smallest size of particles were found to experience little to no movement, which is because of the relatively large cohesive forces that exist between them [31]. There are a number of particles that are suspended by the turbulence in the flow, but relatively few particles are actually entrained by the rotor wake flow. The particles that do become airborne closely follow the surrounding flow vectors because they have low mass and drag.

The medium sized particles (45–63 μm diameter) were the more mobile of those used in the present work, with many particles in this case being mobilized to form the initial saltation layer. This mobility is a consequence of the sediment particles being large enough to have relatively lower cohesive forces, but still being small and light enough to be uplifted and suspended into the flow. It was observed (see previously) that the vortices that convect over the sediment bed can easily entrain these particles into the upwash regions of the flow and also bombard them back onto the bed in the downwash regions. The passing of each vortex resuspends some of the particles, although though there are relatively few particles suspended in the overall flow in this case. As previously explained, this outcome arises because the suspended particles (at least in this case) have

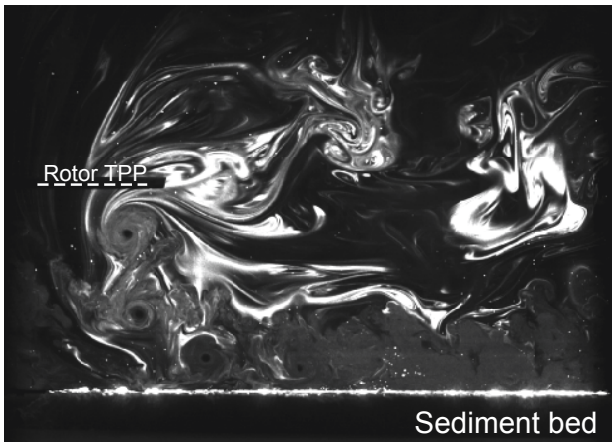

(a) 1–38 μm particles

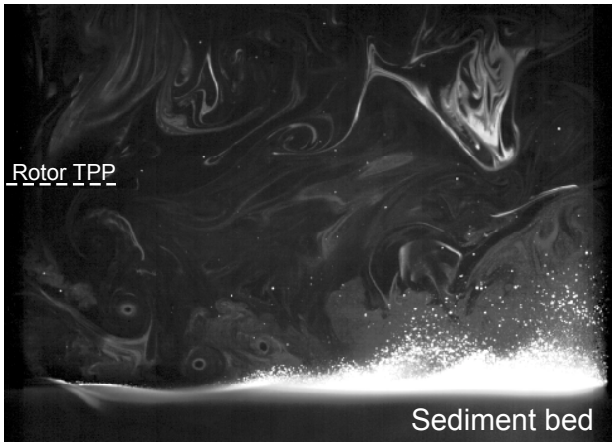

(b) 45–63 μm particles

(c) 90–120 μm particles

Figure 3.23: FV of the dual-phase flow below the rotor for three different sediment sizes.

average settling velocities that are greater than the surrounding upward flow velocities and turbulent flow fluctuations.

The largest particle diameter range (90–120 μm) was relatively mobile, but not as much as for the medium size range because in this case they are relatively heavier. These particles experienced creep and saltation, but it was observed that there were fewer particles being uplifted into suspension.

A further understanding of the the differences in the sediment particle fields for each particle size group was accomplished by examining the PIV/PTV results, as shown in Fig. 3.24. The flows obtained with smallest size range (1–38 μm) showed that almost no particles were suspended, but more interestingly there was no saltation layer. This outcome is because the action of the flow velocities and shear stresses on the ground below the rotor is too low to even initiate creep and/or saltation. The smallest particle sizes also stand out from the other two size ranges because they have the tendency to form clumps or aggregates under the action of the cohesive forces. The resulting mass of the aggregate further resists direct entrainment and uplift from the action of the boundary layer.

For the flows that were studied, the medium size range of particles (45–63 μm in diameter) generally produced a clearly formed saltation layer over the bed. In this case, the particles underneath the impinging vortex flow were convected upward by the surrounding upwash field. The smaller particles in the range were thrown into suspension, while the larger particles were spun out of the influence of the vortex by centrifugal forces and then had a tendency to impact the bed, as shown by the thicker saltation layer in the far right of the image. However, with the larger particles, several previously identified

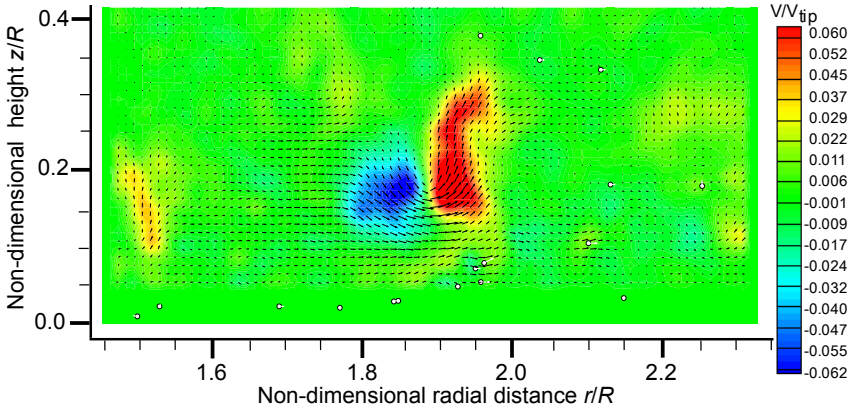

(a) 1–38 μm particles

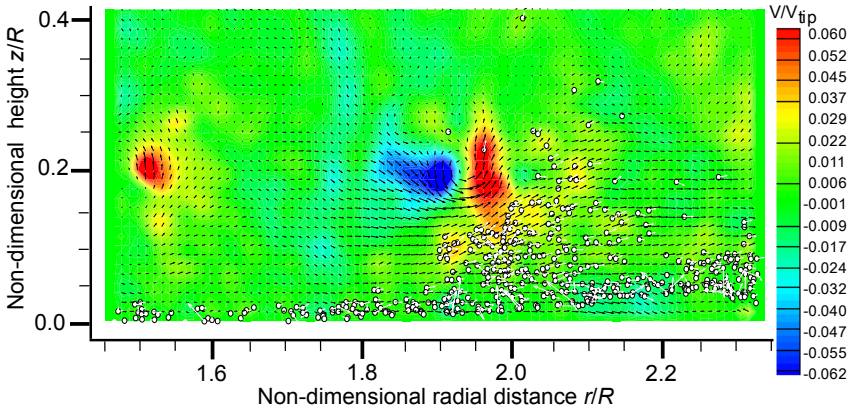

(b) 45–63 μm particles

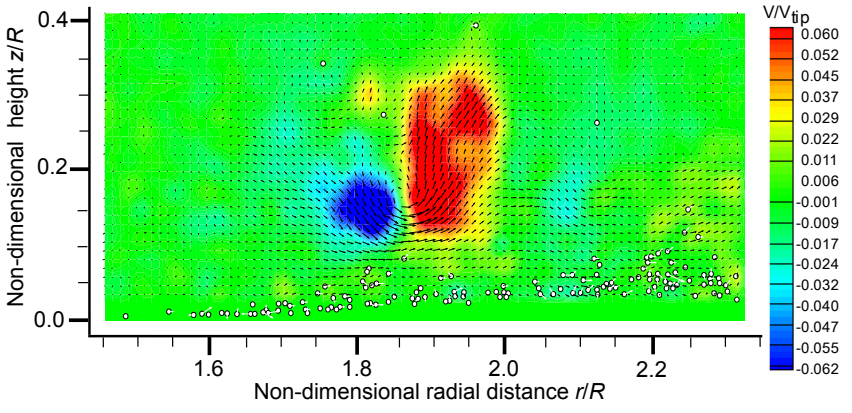

(c) 90–120 μm particles

Figure 3.24: Comparison of PIV/PTV results for flows with different sediment sizes.

mobilization and uplift mechanisms were absent. There was still a well-formed saltation layer, however, the vortex flow did not trap many particles, which has been previously shown to be the mechanism that contributes the most to particle uplift and suspension, when it occurs. Consequently, there were fewer particles suspended in the flow and all secondary suspension was absent. This observation shows that all of the aforementioned mechanisms must be active to form a saltation layer that is sufficiently laden with particles to ultimately generate significantly concentrated particle fields near the rotor.

3.4 Chapter Summary

This chapter has described the experimental results obtained using flow visualization and time-resolved particle image velocimetry of a rotor hovering above a ground plane or sediment bed. Single-phase and dual-phase flow observations were for made for a rotor (in both a 1- and 2-bladed configuration) that was operated at various heights off the ground. It was shown that decreasing the heights and/or using two blades resulted in a significant increase in vortex-vortex interactions such as pairing and merging and, therefore, an increase in the aperiodicity in the flow. With the passing of each blade tip vortex, there was found to be large transient excursions in both the wall-parallel and wall-normal flow velocities, which was a phenomenon primarily responsible for mobilizing and uplifting sediment. Five fundamental mobilization and uplift mechanisms were observed: modified creep and saltation, vortex-induced trapping, secondary suspension, and reingestion bombardment, with unsteady pressure effects being a hypothesized sixth mechanism. The onset of creep and saltation bombardment were found to be cascade-

producing mechanisms, creating a significantly concentrated saltation layer from which particles were more easily uplifted. Within this saltation layer, it was seen that densely packed particles also had the propensity to collide with each other. The effects of sediment size were also examined. It was noted that the smaller particles were more cohesive and less easily mobilized, while the larger size of particles were too heavy to be uplifted. The medium range size of particles used in the present work, unlike the other two size ranges, experienced all five uplift and mobilization mechanisms and were more likely to be uplifted by the impinging rotor wake.

Chapter 4

Conclusions

4.1 Summary

Time-dependent flow visualization and particle image velocimetry measurements were performed with a laboratory-scale rotor system that was operated at different heights above a mobile sediment bed. The rotor was tested in both in a single blade configuration and with two blades. Two-phase flow measurements were taken with sediment particles comprising glass microspheres in three diameter ranges: 1–38 μm, 45–63 μm, 90–120 μm. Measurements were taken over more complete regions of the flow field, as well as in two detailed near-wall regions. The near-wall measurements were used to understand the details of the complex two-phase fluid dynamic processes that occur on the sediment bed under the action of the vortical rotor flow. Particle tracking velocimetry was performed in these regions to study the interaction between the aerodynamic structures at the ground, and their participation in the ultimate generation and development of a dust cloud. The present research goals included: 1. Better understanding the effects of rotor geometric and operational factors on the wake behavior and blade tip vortex structures, including how these flow characteristics changed at the ground plane; 2. Understanding the details of how the wake vortices interacted with the mobile sediment bed, and how the resulting two-phase flow developed in this region.

4.2 Specific Conclusions

The following conclusions have been drawn from the research that was conducted:

1. The results have shown that the blade tip vortices contribute significantly to the mobilization and uplift of sediment from the ground below a rotor. In fact, five of the six sediment mobilization and uplift mechanisms identified in this research work were directly affected by the near-wall effects produced by such vortical flows.

2. Five fundamental sediment transport and uplift mechanisms below the rotor were identified: 1. creep, 2. modified saltation bombardment, 3. vortex-induced trapping, 4. reingestion bombardment (local and global), and 5. secondary suspension. In the dual-phase flow environment produced below the rotor, all of these mechanisms usually occurred simultaneously, their interactions often creating a sustaining or cascading effect that served to rapidly entrain more sediment particles into the flow.

3. The effects of saltation bombardment created a relatively concentrated saltation layer near the ground as the flow developed over the ground. Mobile particles in the saltation layer were shown to be easily trapped by the upwash region of a passing vortex and quickly convected upward. Such particles often experienced bombardment back into the bed if they were recirculated into the vortex flow or if they experienced secondary suspension when trapped in the flow by a younger vortex.

4. The passing of each vortex created transient excursions in the local flow velocities.

These excursions significantly increased the wall-parallel and wall-normal velocities and also had effects to substantial distances above the ground plane. These excursions tended to be large enough to both mobilize sediment, as well as trap sediment in the swirling flow of the vortex, either uplifting the particles into suspension or bombarding them back into the sediment bed.

5. The process of bombardment of suspended sediment particles back onto the underlying bed was shown to eject copious amounts of new particles, which rapidly concentrated the saltation layer and so increased the number of uplift-eligible particles near the ground. This process was observed to contribute significantly to the number of particles that were uplifted and seems particular to dual-phase flows with coherent downwash regions in the near-wall region such as those produced by a rotor flow.

6. Lowering the rotor height increased the aperiodicity of the rotor wake and increased the susceptibility of the helicoidal wake vortices to exhibit vortex-vortex interactions such as pairing and viscous merging of adjacent vortices. The consequences included increases in the quantity of uplifted sediment because of the large transient excursions in the combined flow of the merged vortices that was subsequently produced.

7. The 2-bladed rotor was shown to increase the propensity of vortex induced trapping and local transient excursions from the mean flow velocity over that seen with the 1-bladed rotor. The 2-bladed rotor also increased the overall levels of aperiodicity in the flow and the amount of sediment that was entrained in the upwash regions of the

vortices. The associated excursions in flow velocity also created an increase in the frequency and intensity of bombardment of the sediment back onto the underlying bed, which in turn produced a thicker and more concentrated saltation layer near the ground.

8. Observations of the near-wall sediment motion suggest that there is a sixth possible mechanism affecting sediment mobility and uplift that is produced by the low pressure field induced by the vortices. In this regard, it was noted that sediment particles on or near to the bed can, at times, move almost vertically upwards as a vortex convects directly above. While further studies will need to be conducted, it has been hypothesized that the unsteady pressures caused by a convecting vortex may be strong enough to directly entrain particles and/or alter their trajectories within the saltation layer, even in the absence of other mobilization and uplifting effects.

4.3 Suggestions for Future Work

The results from this work have given a new understanding of the possible mechanisms involved in the mobilization and uplift of sediment in the problem of helicopter brownout. However, there are still several other experiments that could be conducted to help provide a better understanding of the generation and evolution of a brownout dust cloud. These experiments could include, but are not limited to, an examination of the effects of blade tip shape, tip anhedral, radius, blade planform, and blade twist. Furthermore, all the experiments conducted in the present work were for a rotor operating in

hover. In reality, brownout is a problem that occurs when a rotorcraft is taking off or landing, i.e., with some combination of vertical and/or translational motion. To this end, the flow environment produced under these conditions will help to further understand the fluid dynamics associated with the formation of a brownout dust cloud.

The blade tip vortices were observed to contribute significantly to the quantity of uplifted sediment. This outcome suggests that significantly diffusing the blade-tip vortices and spreading the distribution of their induced velocity field may also reduce the quantity of uplifted sediment. To this end, the slotted-tip is an idea that has been studied in some detail [21, 48–50], and may be a good candidate to explore for brownout mitigation. Figure 4.1 shows an image of the slotted-tip design; the slots at the leading edge passively draw in air and eject it out of the side edge of the blade, at the location the tip vortex originally form. The four "jets" serve to inject turbulence and vorticity into the otherwise laminar core of the tip vortex, causing it to become turbulent and diffuse more quickly. By the time the vortices reach the ground, significantly lower swirl velocities remain as compared to an equivalent rectangular tipped rotor blade [21]. However, to properly investigate whether the slotted tip can potentially mitigate brownout, it needs to be thoroughly studied in a dual-phase environment.

The work conducted in the present research has also hypothesized that there was an unsteady suction pressure effect that contributed to the uplift and entrainment of sediment particles into the flow. To quantify this phenomenon, a detailed measurements of the pressure field below an impinging rotor wake will be required. For example, a row of pressure transducers below a hovering rotor would give a time history of the pressure loads that are produced on the sediment bed and may help to quantify the significance of

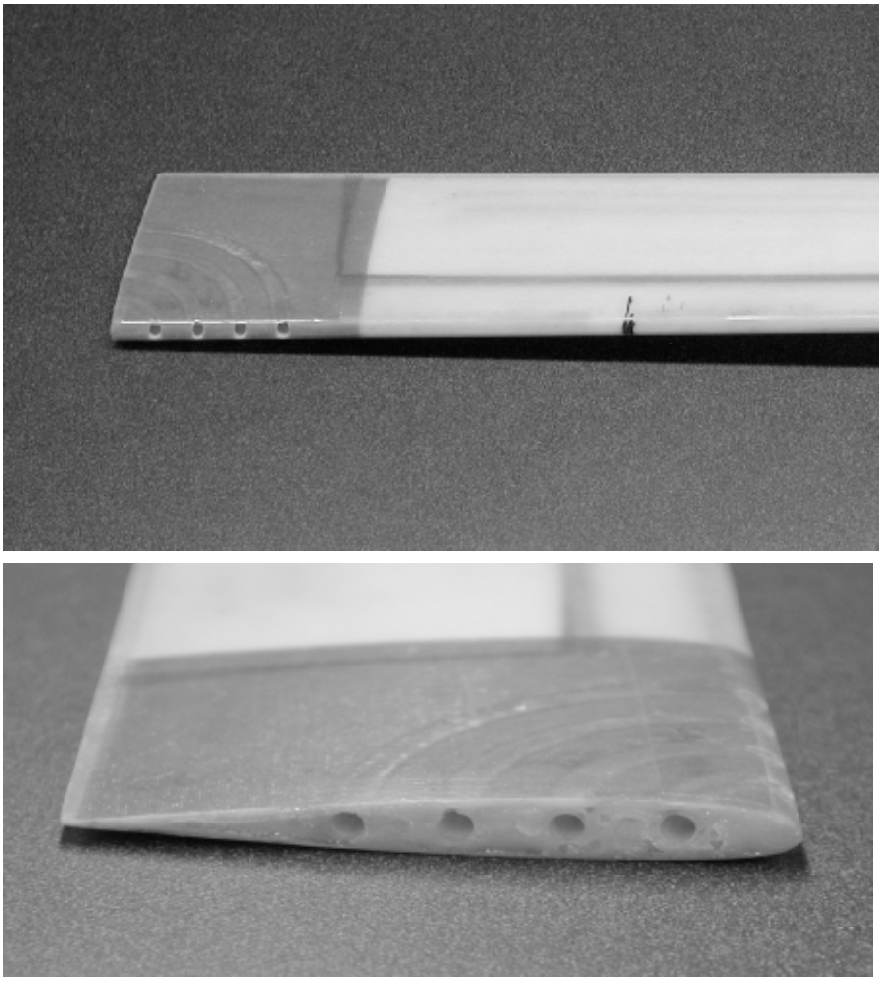

Figure 4.1: Slotted-tip design, with four slots passing from the leading edge to the side edge of the blade.

this possible mechanism.

The rotor flow is intricately complex and three-dimensional. In an effort to quantify this three-dimensionality, a number of different PIV experiments can be performed. To further understand the overall flow, the test volume can be dissected into a number of radial planes, with phase-resolved and time-resolved PIV being performed in both. This approach can work in single-phase and dual-phase environments and may provide fur-

ther insight into the three-dimensionality of the flow field. This approach can be further refined by taking one of these radial planes, namely the plane coincident with the rotor shaft axis, and performing phase-resolved PIV. This technique measures all three velocity components simultaneously.

The effect of three different sediment diameter ranges was studied in the present work, however, there are a number of combinations of these size ranges that can be examined. To properly quantify the dual-phase environment, the sediment bed should, in the first instance at least, be prepared with sediment sizes corresponding to infield sediment particle diameter distributions. The challenge with this approach is that the sediment dynamics and forces involved do not typically scale directly. There are, in fact, 15 different scaling parameters in the field of sedimentology alone. To this end, a scaling study should be performed and according to the results of said study, a sediment bed can be prepared corresponding to the infield particle size distribution, effectively performing a test that scales the problem of helicopter brownout down to the laboratory scale.

Another avenue of fruitful research that would potentially be useful in understanding the two-phase problem further is to attempt to individually study the effects of specific flow features on the mobilization and uplift of sediment. For example, the flow at the ground under a rotor is comprised of two characteristic components, namely a wall-jet type flow and dominant vorticity (i.e., the tip vortices). To further understand and quantify the fluid mechanisms responsible for sediment uplift, a comparison of a classic wall-jet and a rotor flow would be extremely useful. The information that can be gathered from a single-phase and dual-phase wall-jet study, such as sediment threshold friction velocities, flow couplings, sediment mobilization mechanisms, turbulence quantities, etc. would be

helpful in better understanding the fundamental physics of rotor wake interactions with a sediment bed.

The dual-phase observations in this study have been primarily qualitative and have identified the fundamental uplift and mobilization mechanisms involved in the problem of helicopter brownout. While these observations are extremely useful, they do not quantify the dual-phase flow. To this end, the particle field can be analyzed using a concentration map, effectively binning each image to obtain a density field for each ROI. Other approaches, such as measuring particle fluxes across radial planes should also be explored in an attempt to quantify this dual-phase flow. This study can also be performed in an ROI that is in the pilots field of view, i.e., orthogonal to those studied in the present work. The quantification of the sediment particle field in this region will help in the understanding of vertical transport and concentrations of sediment in the areas pilots require visibility.

Bibliography

[1] Mapes, P., Kent, R., Wood, R., "DoD Helicopter Mishaps FY85-05: Findings and Recommendations," U.S. Air Force, 2008.

[2] National Transportation Safety Board, NTSB Accident Briefs: LAX01LA283, LAX01LA304, LAX04LA285, SEA05CA173.

[3] Jansen, C., Wennemers, A., and Groen, E., "FlyTact: A Tactile Display Improves a Helicopter Pilots Landing Performance in Degraded Visual Environments," *Haptics: Perception, Devices and Scenarios*, Vol. 5024, 2008, pp. 867–875

[4] "Sandblaster 2 Support of See-Through Technologies for Particulate Brownout," Task 1 Technical Report, Sponsored by Defense Advanced Research Projects Agency (DOD) Strategic Technology Office, Issued by U.S. Army Aviation and Missile Command Under Contract No. W31P4Q-07-C-0215, MRI Project No. 110565, October 31, 2007.

[5] "Sandblaster 2 Support of See-Through Technologies for Particulate Brownout," Task 5 Final Technical Report, Sponsored by Defense Advanced Research Projects Agency (DOD) Strategic Technology Office, Issued by U.S. Army Aviation and Missile Command Under Contract No. W31P4Q-07-C-0215, MRI Project No. 110565, October 31, 2007.

[6] Wong, O. D., and Tanner, P. E., "Photogrammetric Measurements of an EH-60L Brownout Cloud," American Helicopter Society 66th Annual Forum Proceedings, Phoenix, AZ, 11–13 May 2010.

[7] Milluzzo, J., and Leishman, J. G., "Assessment of Rotorcraft Brownout Severity in Terms of Rotor Design Parameters," *Journal of the American Helicopter Society*, Vol. 55, (3), October 2010, DOI: 10.4050/JAHS.55.032000.

[8] Johnson, B., Leishman, J. G., and Sydney, A., "Investigation of Sediment Entrainment in Brownout Using High-Speed Particle Image Velocimetry," American Helicopter Society 65th Annual Forum Proceedings, Grapevine, TX, May 27–29, 2009.

[9] Haehnel, R. B., Moulton, M. A., Wenren, W., and Steinhoff, J., "A Model to Simulate Rotorcraft-Induced Brownout," American Helicopter Society 64th Annual Forum Proceedings, Montréal, Canada, April 29–May 1, 2008.

[10] Phillips, C., and Brown, R., "Eulerian Simulation of the Fluid Dynamics of Helicopter Brownout," American Helicopter Society 64th Annual Forum Proceedings, Montréal, Canada, April 29–May 1, 2008.

[11] D'Andrea, A., "Numerical Analysis of Unsteady Vortical Flows Generated by a Rotorcraft Operating on Ground: A First Assessment of Helicopter Brownout," American Helicopter Society 65th Annual Forum Proceedings, Grapevine, TX, May 27–29 2009.

[12] Syal, M., and Leishman, J. G., "An Efficient Mesoscale Sediment Tracking Methodology to Analyze Brownout Cloud Developments," 66th Annual Forum Proceedings of the American Helicopter Society, Phoenix, AZ, May 10–13, 2010.

[13] Syal, M., and Leishman, J. G., "Comparisons of Predicted Brownout Dust Clouds with Photogrammetry Measurements," 67th Annual Forum Proceedings of the American Helicopter Society, Virginia Beach, VA, May 3–5, 2011.

[14] Thomas, S., Anathan, S., and Baeder, J. D., "Eulerian-Lagrangian Analysis of Cloud Evolution Using CFD Coupled with a Sediment Tracking Algorithm," 67th Annual Forum Proceedings of the American Helicopter Society, Virginia Beach, VA, May 3–5, 2011.

[15] Kalra, T., Lakshminarayan, V., and Baeder, J., "CFD Validation of Micro Hovering Rotor in Ground Effect," AHS International Specialists Conference on Aeromechanics, San Francisco, CA, January 20–22, 2010.

[16] Morales, F., Naqvi, I., Squires, K. D., and Piomelli, U., "Euler-Lagrange Simulations of Particle Interactions with Coherent Vortices in Turbulent Boundary Layers," Presented at the 62nd Annual Meeting of the Division of Fluid Dynamics, Minneapolis, Minnesota, November 2009.

[17] Morales, F., Naqvi, I., Squires, K. D., and Piomelli, U., "Euler-Lagrange Simulations of Particle Interactions with Coherent Vortices in Turbulent Boundary Layers," *Bulletin of the American Physical Society*, Vol. 54, (19), 2009.

[18] Whitehouse, G. R., Wachspress, D. A., Quackenbush, T. R., Keller, J. D., "Exploring Aerodynamic Methods for Mitigating Brownout," American Helicopter Society 65th Annual Forum Proceedings, Grapevine, TX, May 27–29, 2009.

[19] Tritschler, J., Syal, M., Celi, R., and Leishman, J. G., "A Methodology for Rotor Design Optimization for Rotorcraft Brownout Mitigation," American Helicopter Society 66th Annual Forum Proceedings, Phoenix, AZ, May 10–13, 2010.

[20] Lee, T. E., Leishman, J. G., and Ramasamy, M., "Fluid Dynamics of Interacting Blade Tip Vortices With a Ground Plane," American Helicopter Society 64th Annual Forum Proceedings, Montréal, Canada, April 29–May 1, 2008.

[21] Milluzzo, J., Sydney, A., and Leishman, J. G., "In Ground Effect Aerodynamics of Rotors with Different Blade Tips," 66th Annual Forum Proceedings of the American Helicopter Society, Phoenix, AZ, May 2010.

[22] Knight, M., and Hefner, R. A., "Analysis of Ground Effect on the Lifting Airscrew," NACA TN 835, 1941.

[23] Zbrozek, J., "Ground Effect on the Lifting Rotor," British ARC R & M 2347, 1947.

[24] Cheeseman, I. C., and Bennett, W. E., "The Effect of the Ground on a Helicopter Rotor in Forward Flight," ARC R & M 3021, 1955.

[25] Fradenburgh, E. A., "The Helicopter and the Ground Effect Machine," *Journal of the American Helicopter Society*, Vol. 5, (4), 1960, pp. 26–28.

[26] Hayden, J. S., "The Effect of the Ground on Helicopter Hovering Power Required," American Helicopter Society 32th Annual National V/STOL Forum Proceedings, Washington D.C., May 10–12, 1976.

[27] Prouty, R. W., "Ground Effect and the Helicopter," AIAA Paper 85-4034, AIAA/AHS/ASEE Aircraft Design Systems and Operations Meeting, Colorado Springs, CO, October 14–16, 1985.

[28] Curtiss, H. C., Sun, M., Putman, W. F., and Hanker, E. J., "Rotor Aerodynamics in Ground Effect at Low Advance Ratios," *Journal of the American Helicopter Society*, Vol. 29, (1), 1984, pp. 48–55.

[29] Curtiss, H. C., Erdman, W., and Sun, M., "Ground Effect Aerodynamics," *Vertica*, Vol. 11, (1/2), 1987, pp. 29–42.

[30] Light, J. S., and Norman, T., "Tip Vortex Geometry of a Hovering Helicopter Rotor in Ground Effect," American Helicopter Society 45th Annual Forum Proceedings, Boston, MA, May 22–24, 1989.

[31] Bagnold, R. A., *The Physics of Blown Sand and Desert Dunes*, Dover Publications, Inc., Mineola, NY, 1941.

[32] Greeley, R., and Iversen, J. D., *Wind as a Geological Process on Earth, Mars, Venus, and Titan*, Cambridge University Press, New York, NY, 1985, Chapter 3.

[33] Greeley, R., Iversen, J. D., Marshall, J. R., and Pollack, J. B., "Aeolian Saltation Threshold: The Effect of Density Ratio," *Sedimentology*, Vol. 34, (4), 1987, pp. 699–706.

[34] Nathan, N. D., and Green R. B., "Measurements of a Rotor Flow in Ground Effect and Visualisation of the Brown-out Phenomenon," American Helicopter Society 64th Annual Forum Proceedings, Montréal, Canada, April 29-May 1, 2008.

[35] Dade, B., "A Comparative Study of the Vertical Structure of Near-Bed Sediment Transport," Presented at the Annual Meeting of the American Geophysical Union, San Francisco, CA, December 13–17, 2010.

[36] Dade, B., "Characterization of Near-Bed Sediment Transport in Air and Water," submitted to Sedimentology,

[37] Dade, B., "Near-Bed Aeolian Sediment Transport Under Non-Uniform Flows," Presented at the American Geophysical Union, December 2009.

[38] Mulinti, R., and Kiger, K., "Two-Phase PIV Measurements of Particle Suspension in a Forced Impinging Jet," 63rd Annual Meeting of the APS Division of Fluid Dynamics, Vol. 55, (16), November 21–23, 2010, Long Beach, CA.

[39] Geiser, J., and Kiger, K., "A Simplified Analog for a Rotorcraft-in-Ground- Effect Flow Using a Forced Impinging Jet," 63rd Annual Meeting of the APS Division of Fluid Dynamics, Vol. 55, (16), November 21–23, 2010, Long Beach, CA.

[40] Geiser, J., and Kiger, K. T., "Vortex Ring Breakdown Induced by Topographic Forcing," 13th European Turbulence Conference, Warsaw, Poland, 12–15 September. Journal of Physics: Conference Series, Advances in Turbulence (peer reviewed), 2011

[41] Ramasamy, M., Johnson, B., and Leishman, J. G., "Understanding the Aerodynamic Efficiency of a Hovering Micro-Rotor," *Journal of American Helicopter Society*, Vol. 53, (4), October, 2008, pp. 412–428.

[42] Leishman, J. G., "On Seed Particle Dynamics in Tip Vortex Flows," *Journal of Aircraft*, Vol. 33, (4), 1996, pp. 823–825.

[43] Raffel, R., Willert, C., Wereley, and S., Kompenhans, J., *Particle Image Velocimetry: A Practical Guide*, Second Edition, Springer, Berlin, Germany, 2007.

[44] Scarano, F., "Iterative Image Deformation Methods in PIV," *Measurement Science and Technology*, Vol. 13, 2002, pp. R1–R19.

[45] Ramasamy, M., and Leishman, J. G., "Benchmarking PIV with LDV for Rotor Wake Vortex Flows," *AIAA Journal*, Vol. 45, (11), November 2007, pp. 2622–2633.

[46] Ramasamy, M., and Leishman, J. G., "Interdependence of Diffusion and Straining of Helicopter Blade Tip Vortices," *Journal of Aircraft*, Vol. 41, (5), September 2004, pp. 1014–1024.

[47] Greeley, R., Balme, M. R., Iversen, J. D., Metzger, S., Mickelson, R., Phoreman, J., and White, B., "Martian Dust Devils: Laboratory Simulations of Particle Threshold," *Journal of Geophysical Research (Planets)*, Vol. 108, No. E5, 5041, May 2003, pp. 1–17, DOI: 10.1029/2002JE001987.

[48] Han, O. Y., and Leishman, J. G., "Performance Measurements of a Rotor Blade With a Slotted Tip," American Helicopter Society 60th Annual Forum Proceedings, Baltimore, MD, June 7–10 2004.

[49] Han, O. Y., and Leishman, J. G., "Experimental Investigation of Tip Vortex Alleviation Using a Slotted Tip Rotor Blade," *AIAA Journal*, Vol. 42, (4), 2004.

[50] Leishman, J. G., and Han, O. Y., "Rotor Blade System With Reduced Blade-Vortex Interaction Noise," U.S. Patent 6,948,906 B2, September 27, 2005.